



HAL
open science

Singular beam shaping from spin-orbit flat optics

Mushegh Rafayelyan

► **To cite this version:**

Mushegh Rafayelyan. Singular beam shaping from spin-orbit flat optics. Other. Université de Bordeaux, 2017. English. NNT : 2017BORD0583 . tel-01558113

HAL Id: tel-01558113

<https://theses.hal.science/tel-01558113>

Submitted on 7 Jul 2017

HAL is a multi-disciplinary open access archive for the deposit and dissemination of scientific research documents, whether they are published or not. The documents may come from teaching and research institutions in France or abroad, or from public or private research centers.

L'archive ouverte pluridisciplinaire **HAL**, est destinée au dépôt et à la diffusion de documents scientifiques de niveau recherche, publiés ou non, émanant des établissements d'enseignement et de recherche français ou étrangers, des laboratoires publics ou privés.

THÈSE PRÉSENTÉE
POUR OBTENIR LE GRADE DE
DOCTEUR DE
L'UNIVERSITÉ DE BORDEAUX

ÉCOLE DOCTORALE DES SCIENCES PHYSIQUES DE L'INGÉNIEUR
SPÉCIALITE : LASER, MATIÈRE ET NANOSCIENCES

par

Mushegh RAFAYELIAN

Sujet :

Singular beam shaping from spin-orbit flat optics

Soutenance le 3 mai 2017 devant la Commission d'examen :

M. GARNACHE Arnaud	Directeur de recherche, Université de Montpellier	Présidente
M. GROSJEAN Thierry	Chargé de recherche, Institut Femto-ST	Rapporteur
M. AGEZ Gonzague	Maître de conférences, Université de Toulouse	Examineur
M. BRASSELET Etienne	Directeur de recherche, Université de Bordeaux	Directeur

Acknowledgments

I express my deep gratitude to my scientific advisor Etienne Brasselet. I strongly appreciate the knowledge he has transferred to me during my PhD years. I would also like to thank my committee members Arnaud Garnache, Thierry Grosjean and Gonzague Agez for their attention and interest to this work, and for their valuable comments and suggestions, thanks to you.

I express my appreciation to all coauthors that have contributed in the carried research and related publications. I thank all my team members, Mohamed, Charles, Georgiy, Davit, Artur, Tatiana, Hernando, Nina, Mikaël, Benjamin and Sasha, for kindly sharing their equipment, time and knowledge with me. In addition, I express my gratitude to friendly and professional staff of Laboratoire Ondes et Matière d'Aquitaine and the former director, Jean-Pierre Delville for accepting me to this scientific community.

I would like to thank my family for supporting me spiritually throughout writing this thesis.

Last but not the least, I would like to thank to the programm Erasmus Mundus Action 2 (EMA2) for its financial support to my PhD studies.

Titre : Mise en forme singulière de faisceaux lumineux à l'aide de composants optiques spin-orbite plans

Résumé : Dans ce travail nous avons résolu deux problèmes principaux de la mise en forme topologique de faisceau paraxial pour les composants plans : la modalité et le polychromatisme. Nous les résolvons en introduisant de nouveaux concepts d'éléments optiques à interaction spin-orbite, à savoir la "q-plate modale" et la "q-plate Bragg-Berry". D'un côté, la q-plate modale convertit un faisceau gaussien incident en un faisceau de Laguerre-Gauss pour un indice radial et un indice d'azimut donnés, ce qui par conséquent dépasse les capacités des q-plates conventionnelles qui ne modifient que le degré de liberté azimutal, c.à.d. le moment orbital angulaire de la lumière. À des fins expérimentales, deux approches ont été développées : une basée sur des lames de verre nanostructurées artificiellement, l'autre sur des défauts topologiques de cristaux liquides auto-organisés naturellement. D'un autre côté, la q-plate Bragg-Berry consiste en une fine couche inhomogène de cristaux liquides chiraux (cholestériques) devant un miroir, ce qui fournit une mise en forme de faisceau spin-orbite pleinement efficace sur une large bande spectrale du faisceau incident, contrairement au q-plates conventionnelles qui ne sont fabriqués que pour une longueur d'onde donnée. Par ailleurs, nous obtenons une mise en forme de faisceau spin-orbite ultra-large bande en induisant une modulation de la structure supramoléculaire torsadée des cristaux liquides cholestériques selon la direction de propagation de la lumière. Nous montrons également que la présence du miroir derrière permet un puissant contrôle spatio-temporel des propriétés vectorielles de la polarisation du champ lumineux générées par la q-plate Bragg-Berry.

Mots clés : Mise en forme de faisceau singulier, vortex optique, mode de Laguerre-Gauss, q-plate, défauts de cristaux liquides, cristaux liquides chiraux, chiralité à rampe de pas, modulation spatio-temporelle, faisceau vectoriel

Title: Singular beam shaping from spin-orbit flat optics

Abstract: It is well-known that paraxial coherent electromagnetic fields can be completely characterized in terms of their radial and azimuthal spatial degrees of freedom in the transverse plane that add to the polarization degree of freedom and wavelength. In this work we address two main issues of paraxial beam shaping that are the modality and the polychromaticity in the context of flat-optics that we address by introducing novel concepts of spin-orbit optical elements. Namely, the 'modal q-plate' and the 'Bragg-Berry q-plate'. On the one hand, modal q-plate converts an incident fundamental Gaussian beam into a Laguerre-Gaussian beam of given radial and azimuthal indices, hence going beyond the capabilities of conventional q-plates that only control the azimuthal degree of freedom, i.e. the orbital angular momentum content of light. Towards experimental realization of modal q-plates, two approaches are developed: one based on artificially nanostructured glasses and another based on naturally self-organized liquid crystal topological defects. On the other hand, Bragg-Berry q-plate consist of mirror-backed inhomogeneous thin film of chiral liquid crystal (cholesteric) that provides fully efficient spin-orbit beam shaping over broad spectral range of the incident beam, in contrast to the conventional q-plates that are designed for single wavelength. Furthermore, ultra-broadband spin-orbit beam shaping is achieved by inducing an extra modulation of the supramolecular twisted structure of the cholesteric liquid crystal along the propagation direction. We also show that the presence of a back-mirror allows a powerful spatio-temporal control of the polarization vectorial properties of the light fields generated by Bragg-Berry q-plate.

Keywords: Singular beam shaping, optical vortex, Laguerre Gaussian mode, q-plate, liquid crystal defect, chiral liquid crystal, gradient-pitch chirality, spatio-temporal modulation, vector beam

Résumé en français

Dans ce travail nous avons résolu deux problèmes principaux de la mise en forme topologique de faisceaux : la modalité et le polychromatisme, traités respectivement dans le chapitre 1 et le chapitre 2.

Chapitre 1 – Mise en forme modale de faisceau, à partir d’éléments optiques biréfringents non-homogènes

Ce chapitre introduit le concept de mise en forme « modale » de faisceaux lumineux, c’est-à-dire la conversion d’un mode de propagation gaussien en des modes de Laguerre-gauss ou de Hermite-gauss. Notre étude théorique, dans la Sec. 1.1, propose les combinaisons de phases dynamiques et géométriques à appliquer au mode gaussien incident afin d’aboutir, directement en sortie de dispositif, au mode arbitraire choisi. Cette technique surpasse les techniques actuelles de mise en forme de faisceaux dans la mesure où le mode parfait recherché peut être généré directement à la sortie du masque de phase et ne nécessite pas la propagation du champ lumineux ou de systèmes de filtrage spatiaux pour « nettoyer » le faisceau du bruit optique induit par la conversion de phase.

Face au niveau de complexité des distributions de retard de phase requis pour l’ingénierie des q-plates modales, deux approches ont été explorées pour la réalisation des structures. La première approche, développée dans la Sec. 1.2, consiste à simplifier la structuration de phase de la q-plate en se plaçant dans l’approximation des petits déphasages. Il s’agit du concept de « q-plate quasi-modale », présentant un rendement de conversion réduit mais devenant accessible technologiquement : elles ont été réalisées avec succès par le biais de techniques de nanostructuration par faisceau laser femto-seconde. Les faisceaux devraient présenter un profil quasi-Laguerre-gaussien. La comparaison avec les q-plate classiques (non modales) réalisées par la même technologie laisse entrevoir des faisceaux plus proches des modes souhaités. La deuxième approche, développée dans la Sec. 1.3, consiste à créer les structurations complexes de biréfringence requises en tirant parti de l’auto-organisation naturelle des cristaux liquides. L’idée est ici de créer des singularités isolées auto-organisées dans le matériau ayant la capacité de moduler la biréfringence selon des fonctions décrivant la structuration des q-plates. Ce concept est étudié sur la base du modèle analytique de Rapini prédisant clairement une conversion modale avec une limite maximale d’efficacité de conversion. Enfin, nous présentons les premières démonstrations expérimentales qualitatives des q-plates modales à cristaux liquides auto-organisées prédites

dans le modèle théorique.

Chapitre 2 - Couplage spin-orbite de faisceau large-bande en réflexion sur un milieu anisotropique chiral

Le deuxième chapitre démontre que l'introduction du couplage spin-orbite dans le processus de réflexion lumineuse permet de moduler à la carte la phase de l'onde réfléchie tout en relâchant les contraintes de structuration de la matière propres aux dispositifs transmissifs (q-plates). Une telle mise en forme électromagnétique est démontrée sur la base de réflecteurs de Bragg à cristaux liquides présentant une structuration nanométrique chirale sous la forme d'hélices. En jouant sur l'orientation de ces hélices nanoscopiques dans le temps ou dans l'espace, nous faisons naître une phase géométrique (dite de Pancharatnam Berry) structurant le champ réfléchi et faisant apparaître de nouvelles fonctionnalités optiques.

Tout d'abord, dans Sec. 2.2, il est montré qu'un réflecteur de Bragg, créé à partir d'une distribution homogène de nano-hélices, mis en rotation développe une phase géométrique induisant un effet Doppler sur l'onde réfléchie (léger décalage en fréquence de l'onde). Ce phénomène est expliqué selon 3 approches théoriques différentes et complémentaires : le calcul direct de la phase à la réflexion, le transfert de moment angulaire de la lumière à la matière et ses conséquences sur le champ réfléchi et l'effet Coriolis liée au spin du champ incident dans un référentiel tournant lié au miroir de Bragg en rotation.

Ensuite, dans Sec. 2.3, nous introduisons le concept de miroir de Bragg-Berry sur la base d'une modulation spatiale azimutale de l'orientation des nano-hélices, permettant la création de gradients de phase géométriques azimutaux et une mise en forme topologique du champ réfléchi. Ce concept est démontré expérimentalement avec la génération de vortex à partir de faisceaux gaussiens (diffractant) et de faisceaux de Bessel (dits non-diffractant). Le concept de miroir de Bragg-Berry à ultra-large bande spectrale est ensuite présenté et démontré expérimentalement. Un tel dispositif est rendu possible par l'achromaticité de la phase géométrique et du processus de réflexion. Dans Sec. 2.4 par un procédé de diffusion entre 3 couches de cristaux liquides, la génération d'un miroir de Bragg-Berry à nano-hélices « graduelles » a permis la mise en forme topologique de faisceaux sur une gamme spectrale couvrant les longueurs d'ondes optiques visibles, et donc de générer des vortex de lumière blanche présentant une faible sensibilité à l'angle d'incidence. Grâce à cette réalisation technique, dans Sec. 2.5 nous introduisons et démontrons le concept de « Bragg-Berry q-plate » permettant de lever le verrou de la sélectivité des miroirs de Bragg-Berry vis-à-vis de l'hélicité du champ incident. Il s'agit ici de placer un miroir de Bragg conventionnel après le miroir de Bragg-Berry dans le processus de réflexion optique. Ce nouveau système combine les avantages des deux familles de dispositifs présentés dans les deux chapitres et ouvre la voie vers des faisceaux vortex fortement polychromatiques dont la charge topologique est contrôlée par le moment de spin de la lumière.

Enfin, dans Sec. 2.6, la modulation spatio-temporelle de faisceaux vectoriels est présentée et démontrée sur la base d'une légère translation du miroir de Bragg conventionnel par rapport au miroir de Bragg-Berry. Cette étude apporte la dimension de l'accordabilité dynamique des faisceaux vectoriels, qui connaissent actuellement un intérêt très fort. Par exemple, la possibilité offerte par cette technique de passer continûment d'un faisceau polarisé radialement à un faisceau polarisé azimutalement représente de fortes perspectives dans l'ingénierie de faisceaux focalisés et en optique sub-longueur d'onde. La présentation de tous ces concepts et de leurs bases théoriques respectives est limpide et les résultats expérimentaux sont sans équivoques. Ils sont le fruit de la mise en œuvre de techniques d'imagerie et de caractérisation optiques non triviales permettant de révéler les caractéristiques intrinsèques clés des faisceaux vortex générés.

Les résultats présentés dans cette thèse apportent un nouveau concept de mise en forme de faisceau modal et fournit un nouvel élément spin-orbite réflectif large bande, ce qui, d'un autre côté, peut ouvrir de nouveaux champs de recherche vers des éléments spin-orbite avancés.

Contents

General Introduction	3
Overview	3
Outlook of the thesis	7
1 Modal beam shaping from space-variant anisotropic flat optics	11
1.1 Laguerre Gaussian beam shaping: modal q-plate	11
1.1.1 Position of the concept	11
1.1.2 Conventional q-plate	12
1.1.3 Identification of modal q-plates	13
1.1.4 From modal q-plates to modal HG-plates	19
1.2 Towards experimental realization: quasi-modal q-plates	22
1.2.1 The limit of small retardance: quasi-modality	22
1.2.2 Quantitative modal analysis	23
1.2.3 Fabrication and optical characterization of quasi-modal q-plates	25
1.2.4 Experimental demonstration of quasi-modality	28
1.3 Liquid crystal umbilical defects and their modality	31
1.3.1 Description of umbilical defects	33
1.3.2 Umbilic as a natural modal q-plate candidate	36
1.3.3 Quantitative modal analysis	37
1.3.4 Swirling route to modality	39
1.3.5 Qualitative demonstration	42
2 Reflective broadband spin-orbit beam shaping from chiral anisotropic optical media	45
2.1 Cholesteric liquid crystals: optical characterization	45
2.2 Dynamic geometric phase experiment	49
2.2.1 General consideration	49
2.2.2 Experiment	51
2.2.3 Towards chiral Bragg metasurfaces	53
2.3 Bragg-Berry mirrors	55
2.3.1 Position of the concept	55
2.3.2 Experimental approach	55
2.3.3 Demonstration	57

2.3.4	Polychromatic features	60
2.4	Ultra-broadband Bragg-Berry mirrors	63
2.4.1	Position of the problem	63
2.4.2	Sample preparation	64
2.4.3	Spectral exploration of dynamic geometric phase	65
2.4.4	Gradient-pitch Bragg-Berry mirror demonstration	66
2.5	Bragg-Berry q-plates	70
2.5.1	Position of the problem	70
2.5.2	Mirror-backed uniform Bragg mirror	70
2.5.3	Mirror-backed Bragg-Berry mirror	72
2.6	Spatio-temporally modulated vector beams from Bragg-Berry q-plates	74
2.6.1	Tunable feature of mirror-backed CLCs	74
2.6.2	Calibration of the piezoelectric translation stage	77
2.6.3	Tunable mirror-backed homogeneous CLC: experiment	79
2.6.4	Tunable mirror backed inhomogeneous CLC: experiment	80
	Conclusion and perspectives	83
	Bibliography	98

General Introduction

Overview

The interest in beam shaping increased dramatically in the last years due to the development of various applications that can benefit from it. That led to the increase in research in beam shaping techniques and the corresponding advances in optical component fabrication technology.

A fundamental and attractive kind of beam that is a subject of beam shaping studies since many years is the optical vortex beam, namely light beam carrying optical phase singularity. The first modern day identification of an optical vortex was seemingly reported by Vaughan and Willetts in 1979 [1], who studied the helical wavefront of light beams and their interference along the beam propagation axis. Since then, many studies have been carried out towards helical shaping of optical wavefronts. One can mention spiral phase plates [2–4], which are changing the helical wavefront of the incident beam by their helical structure; computer generated holograms [5, 6], which are digitally generating holographic interference patterns with phase singularities; diffractive optical elements [7]; or geometric Pancharatnam-Berry phase optical elements [8] based on artificial subwavelength dielectric gratings. Liquid crystal fork gratings [9–11], liquid crystal natural topological defects [12, 13] or liquid crystal spatial light modulators (SLMs) [14, 15] are also well-known strategies exhibiting good tunability as well.

It has been shown that the optical vortex beams endowed with on-axis phase singularity, carry well-defined orbital angular momentum per photon [16]. In general, photons possess both spin and orbital angular momenta that are separately measurable [17]. The orbital angular momentum is related to the spatial degrees of freedom of light, while the spin angular momentum is related to the polarization of light. The sum of the spin and orbital angular momenta, the total angular momentum, is an invariant of free-space propagation. The interaction between light and matter may cause interdependent change of the spin and orbital angular momentum contributions of a light field, to which one refers as a spin-orbit interaction. As recently reviewed in [18], a general framework based on optical angular momenta and geometric phases allows one to unravel the various manifestations of the spin-orbit interaction of light. Since geometric phases are associated with rotations of coordinate system and lead to helicity-dependent phases for circularly polarized light [19, 20], they offer a robust roadmap towards

the elaboration of spin-controlled optical elements. In particular, space-variant optically anisotropic planar structures have attracted a lot of interest since more than one decade. In transmission mode, such structures give maximal spin-orbit effect when the half-wave retardation condition is fulfilled [21, 22]. More recently, nanofabrication technologies led to the realization of metasurfaces—planar optical elements with subwavelength thickness—that allow efficient shaping of the amplitude, phase and polarization state of light in an arbitrary manner, as reviewed in [23–31].

Spin and orbital angular momentum of light are the quantum characteristics of photons [32]. Quite naturally, in parallel to the investigations of spin-orbital shaping of light, many investigations have been performed towards the generation and detection of single photons carrying information of both spin and orbital degrees of freedom [33–40], which has been identified as a new resource towards a high-dimensional quantum space encoded in a single photon.

Of course, the interest in beam shaping is not restricted to the quantum manipulations of spin-orbital angular momentum state of single photon. Indeed, there were a lot of beam shaping investigations towards the realization of various families of fundamental beams, such as Laguerre Gaussian (LG), Hermite Gaussian (HG), Ince Gaussian (IG), Bessel, Bessel Gaussian (BG) families etc., that are all solutions of the paraxial wave equation. In particular, they form orthogonal basis on which any paraxial beam can be decomposed. In general, a beam is said to be paraxial if its wavefront normals make small angles with respect to the propagation direction. Hereafter we mainly focus our attention on the LG and HG beams. Taking the z axis as the propagation direction, LG and HG beams with angular frequency ω and wavevector k can be represented in the following forms

$$\begin{aligned} u_{p,\ell}^{\text{LG}}(r, \phi, z) &= \\ &= \frac{C_{p,\ell}^{\text{LG}}}{w(z)} \left(\frac{\sqrt{2}r}{w(z)} \right)^{|\ell|} e^{-\frac{r^2}{w(z)^2}} e^{i\ell\phi} e^{-i(\omega t - kz) + ik\frac{r^2}{2R(z)}} e^{-i(2p+|\ell|+1)\zeta(z)} L_p^{|\ell|} \left(\frac{2r^2}{w(z)^2} \right), \end{aligned} \quad (1)$$

$$\begin{aligned} u_{n,m}^{\text{HG}}(x, y, z) &= \\ &= \frac{C_{n,m}^{\text{HG}}}{w(z)} e^{-\frac{x^2+y^2}{w(z)^2}} e^{-i(\omega t - kz) + ik\frac{(x^2+y^2)}{2R(z)}} e^{-i(m+n+1)\zeta(z)} H_n \left(\frac{\sqrt{2}x}{w(z)} \right) H_m \left(\frac{\sqrt{2}y}{w(z)} \right), \end{aligned} \quad (2)$$

where (ℓ, p) and (n, m) are integer numbers that define the mode of LG and HG beams in the cylindrical, (r, ϕ, z) , and cartesian, (x, y, z) , coordinate systems, respectively. $L_p^{|\ell|}$ and H_n (or H_m) are the generalized Laguerre and Hermite polynomials [41], $w(z) = w\sqrt{1 + z^2/z_R^2}$ is the beam radius at z , $R(z) = (z^2 + z_R^2)/z$ is the radius of curvature, $\zeta(z) = \arctan(z/z_R)$ is the Gouy phase, $z_R = \pi w^2/\lambda$ is

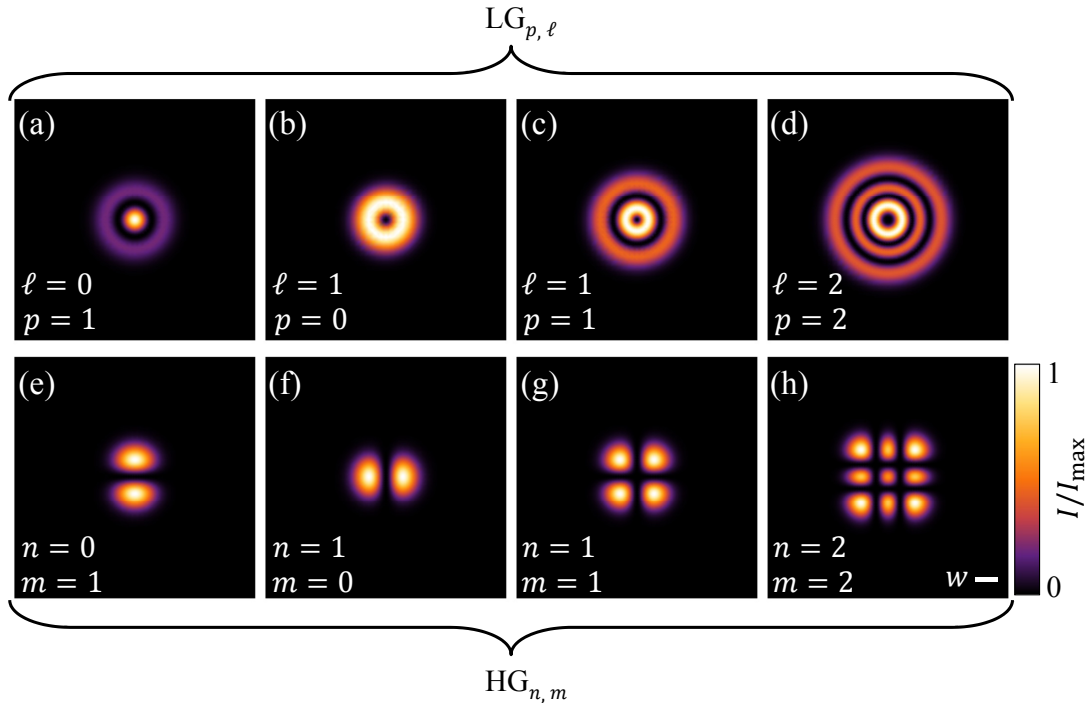


Figure 1: (a,b,c,d) Typical examples of Laguerre Gaussian beams with azimuthal, ℓ , and radial, p , modes. (e,f,g,h) Typical examples of Hermite Gaussian beams with modes n and m . Beams are at their waist plane ($z = 0$ plane). White line refers to w waist radius of beams. The intensities of beams are normalized to their maximums.

the Rayleigh length, w is the beam waist radius at $z = 0$, and finally, $C_{p,\ell}^{LG}$ and $C_{n,m}^{HG}$ are constants whose expressions can be derived from the total power of the beam.

Typical modes of LG and HG beams are illustrated in Fig. 1. The profiles of LG modes show axisymmetric rings, whose number are determined by the radial index p , while the azimuthal index ℓ determines the number of intertwined helical wavefronts. The indices n and m of HG beams determine the number of zeros of amplitude along the x and y directions, respectively. The intensity distribution of such a mode has n nodes in the horizontal direction and m nodes in the vertical direction. For both LG and HG beams, a Gaussian beam is obtained when $n = m = 0$ or $\ell = p = 0$.

Hereinafter we refer to a beam as being “modal” if it is a basis element of any family of solutions of the paraxial wave equation. Obviously, LG and HG beams are such examples. One of the basic property of these beams is that they are self-similar. Namely, their transverse intensity profile is preserved under propagation up to a rigid rescaling. Noting that they also form orthogonal basis enabling the

description of an arbitrary paraxial field, the generation and conversion of pure LG or HG beams is of a paramount practical importance.

One of the principal proposal of our work is associated with the modal beam shaping. So far Laguerre Gaussian and Hermite Gaussian modes have been mainly produced inside optical cavity [42–48]. The most common resonator for LG and HG modes is constructed from convex or concave spherical-mirrors separated by some distance where the mode is generated due to multiple reflections inside the cavity [49]. Intracavity LG or HG beams are supposed to be purely modal. To our knowledge, there are very few extracavity demonstrations of Hermite Gaussian modes generations. Namely, by spatial light modulator or by digital micromirror device (DMD) [50]. Meanwhile, for LG beams, several methods have been developed, such as high-order diffractive optical elements [51], computer generated high-order phase holograms [14], high-order spiral phase plates [4], high-order geometric phase optical elements [52], or amplitude-only spatial light modulators [53, 54]. Remarkably, complex-amplitude modulation can be mimicked by phase-only optical elements with the possibility to generate high-purity LG beams in free space [55, 56]. Noteworthy, strategies based on phase-only or amplitude-only modulation cannot provide a pure LG beam from a typical bell-shaped incident Gaussian beam. In phase-only beam shaping strategies, light acquires its LG-like form after substantial diffraction has taken place [57–59]. In amplitude-only shaping strategies, light acquires its LG form just after the mask but the latter changes upon propagation. In contrast, in an ideal situation, light should form its shape immediately after exiting the system and should propagate in free space self-similarly. In this context, the advent of powerful coherent integrated optical sources with controlled azimuthal and radial indices should emerge in a near future, with a huge range of practical uses such as optical communications, optical imaging, optical trapping, or optical manipulation.

The second main issue addressed in our work is the broadband shaping of optical vortex. Nowadays, broadband transmissive liquid crystal so-called q-plates of arbitrary order can be realized using chiral multilayered structures [60]. Solid-state strategies realizing effective q-plate endowed with broadband capabilities have also been reported [61, 62]. However, the latter approaches are limited to charge $q = 1$ and the poor spatial resolution of the effective optical axis patterning (several millimeters) limits their application potential. Another approach of broadband vortex generation based on Gaussian beam propagation along optical axis of uniaxial crystal is reported in [63]. Noteworthy, due to homogeneity of uniaxial crystal, such optical beam shaping is endowed with perfect resolution. Other kinds of approaches of polychromatic optical vortex generation is based on spatial light modulators [64, 65], Pancharatnam–Berry phase optical elements formed by a space-variant subwavelength grating [66], axially symmetric polarizer [67], ultrathin metasurfaces composed of a dipole antenna

array [68]. In general, rapidly growing supercontinuum laser sources [69–71] encourage the investigations towards achromatic optical elements, such as broadband retarders [72, 73], beam splitters [74], quarter wave-plates retarders [75] or wave-plate lenses [76].

Outlook of the thesis

In this work we have addressed two main issues introduced above in the context of topological beam shaping: the modality and the polychromaticity, respectively, in chapter 1 and chapter 2.

Chapter 1 - Modal beam shaping from space-variant anisotropic flat optics

This chapter introduces the concept of modal beam shaping from a flat space-variant anisotropic optical material. Namely, we show that the combined use of the dynamic and the geometric phases allows to shape arbitrary paraxial field depending on the spatial distribution of both birefringent phase retardation and optical axis orientation of the optical element. To support that idea, in Sec. 1.1 we design “modal q-plates” and “modal HG-plates” that are able to convert an incident Gaussian beam into arbitrary Laguerre Gaussian and Hermite Gaussian beams, respectively. Due to the advantage of pure modality, the modal q-plates and modal HG-plates exhibit perfect LG and HG modes just after the mask, in contrast to the other methods that we have briefly introduced previously. This is an important practical asset from the application point of view. Indeed, current technologies of q-plates allow to reduce their thickness down to a few wavelengths, which gives the possibility to operate mode conversion over a distance of the order of a wavelength.

Afterwards, we move towards the experimental realization of modal q-plates. Two kinds of approaches are discussed in Sec. 1.2 and Sec. 1.3. The first approach is the quasi-modal approach, that implies a deliberate simplification of the perfect modal q-plate proposed approach allowing less challenging fabrication requirements. This approach is demonstrated by realizing glassy quasi-modal q-plates of charges $q = (1/2, 1, 3/2)$ fabricated by femtosecond direct laser writing of self-assembled nanostructures in the bulk of silica glass. Accordingly, quasi-modal q-plates demonstrate better quality of vortex generation compared with conventional q-plates made by the same technology and company. The second approach consists in using naturally self-organized defects in liquid crystals. In contrast to artificial devices, this combines the self-engineered merit with enhanced spatial resolution. More precisely, we propose use of spontaneously formed topological defects appearing in nematic liquid crystals under external electric field. The chosen kind of defects, called umbilics, possess rich optical and structural proper-

ties that can be tuned electrically. Based on the reliable theoretical background of umbilics, we derived the optimal conditions towards modal beam shaping. Finally, we report on the first experimental qualitative demonstration of the predicted self-engineered modal liquid crystal q-plates.

Chapter 2 - Reflective broadband spin-orbit beam shaping from chiral anisotropic optical media

In this chapter we propose and demonstrate a novel kind of spin-orbit optical element with spectrally broadband properties based on the circular Bragg reflection phenomenon [77], specifically using chiral liquid crystals. We claim that such Bragg reflectors, if appropriately structured, can shape the phase of the reflected light in an arbitrary manner. To support this idea, in Sec. 2.2 we present a dynamic geometric phase experiment using a planar homogeneous cholesteric liquid crystal (CLC) film. By mechanically rotating the sample, we show that the reflected beam undergoes an angular Doppler frequency shift, which unveils the geometric phase (in other words Pancharatnam–Berry phase) associated with the spatial orientation of its molecular chiral helices. We note that, the existence of a geometric phase at reflection from homogeneous CLC planar slabs has been also reported in another recent independent report [78]. Consequently, a planar CLC allowing initially patterned inhomogeneous spatial orientations of its helices, is expected to shape the wavefront of Bragg reflected light in arbitrary manner. The experimental demonstration is reported in Sec. 2.3 using a planar inhomogeneous CLC film, where the inhomogeneity is achieved by using inhomogeneous alignment layers at the boundaries of the sample. Accordingly, the incident Gaussian beam on such inhomogeneous Bragg mirror reflects as a vortex beam. The polychromatic properties of such spin-orbit element (later we call it Bragg-Berry mirror or, in short, BB mirror) are analyzed by studying the reflection of an incident supercontinuum laser beam. Importantly, the reflected vortex beam exhibits broadband properties directly associated with the broadband nature of Bragg reflection from such chiral media. Here again similar investigations on vortex generation, lens effect and deflection based on such inhomogeneous planar CLC slabs have been independently reported in [79–81].

In the Sec. 2.4, we archive ultra-broadband reflective shaping of optical vortices using planar inhomogeneous “gradient-pitch” CLC, where the chiral properties are modulated along the beam propagation direction. Gradient-pitch BB mirrors have been fabricated using thermal diffusion between three distinct CLC layers with initially different uniform helix pitches. Remarkably, we experimentally demonstrate that ultra-broadband vortex generation from such BB mirrors are endowed with extreme robustness against large oblique incidences, whose exploration remains an open issue.

Noteworthy, due to the polarization sensitivity of Bragg reflection from CLC, the vortex generation of BB mirrors takes place only for one circular polarization

of incident beam, while the other circular polarization is almost totally transmitted from BB mirror. To solve this practical limitation and get rid of polarization selectivity of BB mirrors, in Sec. 2.5 we suggest to combine a BB mirror with a standard mirror and report experimentally on polarization independent optical vortex generation. In particular, using an incident linearly polarized Gaussian beam we obtain a vector vortex beam in reflection. Based on above mentioned statements, we have concluded that the mirror-backed BB mirror can be considered as a reflective q-plate, in short, a “Bragg-Berry q-plate”.

Finally, in the last section, Sec. 2.6, we discuss the possibility of spatio-temporal modulation of vector fields tailored by the mere control of optical path between the standard and the Bragg-Berry mirrors. The experimental demonstration is carried out by placing the back-mirror on a piezoelectric translation stage and displacing it in a periodic manner.

Modal beam shaping from space-variant anisotropic flat optics

1.1 Laguerre Gaussian beam shaping: modal q-plate

1.1.1 Position of the concept

In this section we propose space-variant uniaxial flat optical elements, designed to generate pure Laguerre Gaussian modes with arbitrary azimuthal and radial indices, ℓ and p , by considering the fundamental case of incident Gaussian beam (see Eq. 1). The key idea is to manipulate an incident light field with the combined use of the dynamic and geometric phases. Without lack of generality, this is made by considering a slab of anisotropic optical medium associated with both space-variant birefringent phase retardation, Δ , and space-variant optical axis orientation in the plane of the slab, ψ . The optical axis orientation along the longitudinal direction of slab is constant. Birefringent phase retardation is a characteristic of an optical anisotropic medium which indicates the difference between optical paths of propagating light polarized along the extraordinary and ordinary axes. Accordingly, this controls the polarization and dynamic phase experienced by the transmitted light. On the other hand, the optical axis orientation angle (i.e. the azimuth) defines the local eigen-frame of the material, and thus controls the geometric phase of the transmitted light. Consequently, an uniaxial planar layer with inhomogeneous retardation and azimuth profiles can shape the dynamic and geometric phases of transmitted light with inhomogeneous polarization in an arbitrary manner.

This kind of elements generalize the well known q-plates, that are associated with $\Delta = \text{constant}$, which is usually tuned to have a $\Delta = \pi$ for the used wavelength (we further refer to this as the half-wave plate condition).

1.1.2 Conventional q-plate

Conventional q-plates are anisotropic transparent uniaxial flat layers with space-variant orientation of optical axis in transverse plane defined by $\psi(\phi) = q\phi$ with q half-integer and with $\Delta = \text{constant}$ birefringent phase retardation, where ϕ is the azimuthal angle in transverse plane of q-plate. In general, the birefringent phase retardation is defined by following $\Delta = (n_e - n_o)kL$, where n_e and n_o are the extraordinary and ordinary components of the local refractive indices, which are parallel and perpendicular to the optical axis, respectively.

First, let us consider the case of circularly polarized normal incident monochromatic plane wave propagating along the z axis with angular frequency ω and wavevector k . The complex representation of plane wave is

$$\mathbf{E}_{\text{in}} = E_0 e^{-i(\omega t - kz)} \mathbf{e}_\sigma, \quad (1.1)$$

where \mathbf{e}_σ is the Jones vector and describes the polarization state of the field. Jones vector has the following form for the circular polarizations

$$\mathbf{e}_\sigma = \frac{1}{\sqrt{2}} \begin{pmatrix} 1 \\ i\sigma \end{pmatrix}, \quad (1.2)$$

where $\sigma = -1$ is for right-handed and $\sigma = 1$ is for left-handed polarizations.

Assuming that the light is incident on the spatial point of q-plate located at $z = 0$ plane with ϕ azimuth angle and neglecting its diffraction effects inside the medium, the output light field just after can be expressed in the laboratory frame by using Jones calculus

$$\mathbf{E}_{\text{out}} = E_0 e^{-i\omega t} \hat{\mathfrak{R}}_z(-\psi(\phi)) \begin{pmatrix} e^{ikLn_e} & 0 \\ 0 & e^{ikLn_o} \end{pmatrix} \hat{\mathfrak{R}}_z(\psi(\phi)) \mathbf{e}_\sigma, \quad (1.3)$$

where L is the thickness of the mask, $\hat{\mathfrak{R}}_z(\psi)$ is the rotation matrix around z axis by an angle $\psi = \psi(\phi)$ with respect to the x axis (see Fig. 1.1).

$$\hat{\mathfrak{R}}_z(\psi) = \begin{pmatrix} \cos \psi & \sin \psi \\ -\sin \psi & \cos \psi \end{pmatrix}. \quad (1.4)$$

After some simplification the output field gets the following form on the basis of the left/right circular polarizations

$$\mathbf{E}_{\text{out}} = E_0 e^{-i\omega t} e^{ikLn_o} e^{i\frac{\Delta}{2}} \left(\cos \frac{\Delta}{2} \mathbf{e}_\sigma + i \sin \frac{\Delta}{2} e^{2i\sigma\psi(\phi)} \mathbf{e}_{-\sigma} \right), \quad (1.5)$$

where $e^{2i\sigma\psi(\phi)}$ is the geometric phase factor generated in the cross-circular part of the beam due to the $\psi(\phi)$ geometric transformation of the optical axis. Note that the sign of geometric phase is dependent on the handedness of circular

polarization. Accounting that $\psi = q\phi$ and that for the given wavelength the retardation is tuned to $\Delta = \pi$, the output field gets the following simple form

$$\mathbf{E}_{\text{out}} = -E_0 e^{-i\omega t} e^{ikLn_o} e^{i2\sigma q\phi} \mathbf{e}_{-\sigma}, \quad (1.6)$$

Consequently an incident circularly polarized light field will be totally converted into a field with orthogonal circular polarization state in transmission, while acquiring an helical wavefront associated with an optical phase singularity with topological charge $l = 2\sigma q$. This technology is ideal in terms of efficiency in order to impart any quantity of orbital angular momentum (OAM) to the light. Since the OAM after a q-plate is characterized only by the azimuthal index ℓ , q-plates can perfectly shape the azimuthal mode of incident Gaussian beam. However, in order to obtain a LG output, one should also pay attention to the radial degree of freedom. For that reason we propose q-plates with spatially-varying properties towards the full control of both the azimuthal and radial features, at the expense of efficiency as we will discuss.

1.1.3 Identification of modal q-plates

Let us consider anisotropic transparent uniaxial flat layer with space-variant orientation of optical axis in transverse plane defined by $\psi(r, \phi)$ and with the space-variant birefringent phase retardation defined by $\Delta(r, \phi)$, where r and ϕ are the polar coordinates in transverse plane of modal q-plate (see Fig. 1.1). In general, the birefringent phase retardation is defined by following $\Delta(r, \phi) = (n_e(r, \phi) - n_o(r, \phi))kL$, where $n_e(r, \phi)$ and $n_o(r, \phi)$ are the extraordinary and ordinary components of refractive indices at that spatial point, which are parallel and perpendicular to optical axis, respectively. For simplicity, hereafter we take constant the ordinary component of refractive index, namely $n_o(r, \phi) = n_o = \text{constant}$.

First, let us again consider the case of circularly polarized normal incident monochromatic plane wave of Eq. 1.1. Assuming that the light is incident on (r, ϕ) spatial location of the medium which is located at $z = 0$ plane and neglecting its diffraction effects inside the medium, the output light field just after can be expressed in laboratory frame by using Jones calculus

$$\mathbf{E}_{\text{out}} = E_0 e^{-i\omega t} \hat{\mathfrak{R}}_z(-\psi(r, \phi)) \begin{pmatrix} e^{ikLn_e(r, \phi)} & 0 \\ 0 & e^{ikLn_o} \end{pmatrix} \hat{\mathfrak{R}}_z(\psi(r, \phi)) \mathbf{e}_\sigma, \quad (1.7)$$

where L is the thickness of the mask, $\hat{\mathfrak{R}}_z(\psi(r, \phi))$ is the rotation matrix around the z axis by an angle $\psi(r, \phi)$ with respect to the x axis (see Eq. 1.4). After simplification the output field gets the following form on the basis of left/right

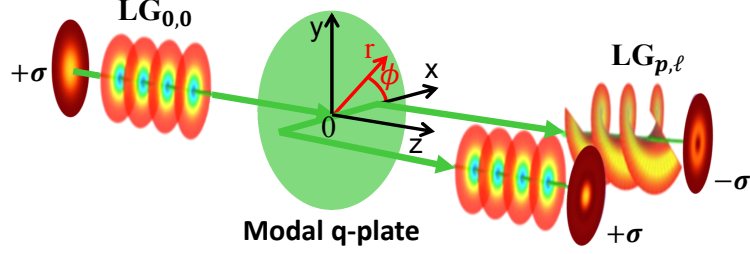


Figure 1.1: The sketch of Laguerre Gaussian mode ($LG_{p,\ell}$) conversion from incident Gaussian beam ($LG_{0,0}$) on the modal q-plate (green ellipse) with the $\Delta_{p,\ell}(r)$ and $\psi_{p,\ell}(r, \phi)$ birefringent phase retardation and azimuth profiles. The $LG_{p,\ell}$ beam has $-\sigma$ circular polarization and helical wavefront while the second part of the beam preserves the σ polarization and not helical structure of incident Gaussian beam.

circular polarizations

$$\begin{aligned} \mathbf{E}_{\text{in}} &= E_0 e^{-i(\omega t - kz)} \mathbf{e}_\sigma, \\ \mathbf{E}_{\text{out}} &= \\ &= E_0 e^{-i\omega t} e^{ikLn_o} e^{i\frac{\Delta(r,\phi)}{2}} \left(\cos \frac{\Delta(r,\phi)}{2} \mathbf{e}_\sigma + i \sin \frac{\Delta(r,\phi)}{2} e^{2i\sigma\psi(r,\phi)} \mathbf{e}_{-\sigma} \right). \end{aligned} \quad (1.8)$$

In general, if the incident field is no longer a plane wave but it varies slowly along propagation direction (paraxial transverse fields), the general output field can be expressed by the output field of Eq. 1.8 multiplied by the spatially varying incident field. Namely, in the case of incident circularly polarized Gaussian beam with its waist plane located at $z = 0$, the input and output fields are expressed as

$$\begin{aligned} \mathbf{E}_{\text{in}} &= E_0 e^{-\frac{r^2}{w_0^2}} e^{-i(\omega t - kz)} \mathbf{e}_\sigma, \\ \mathbf{E}_{\text{out}} &= \\ &= E_0 e^{-i\omega t} e^{ikLn_o} e^{-\frac{r^2}{w_0^2}} e^{i\frac{\Delta(r,\phi)}{2}} \left(\cos \frac{\Delta(r,\phi)}{2} \mathbf{e}_\sigma + i \sin \frac{\Delta(r,\phi)}{2} e^{2i\sigma\psi(r,\phi)} \mathbf{e}_{-\sigma} \right). \end{aligned} \quad (1.9)$$

In the case of a uniform birefringent phase retardation $\Delta(r, \phi) = \pi$ and azimuthally varying optical axis orientation $\psi = q\phi$ with q half-integer, Eq. 1.9 simplifies to the known case of a q-plate (see Eq. 1.6). However, accounting for the structuring upgrade $\pi \rightarrow \Delta_{p,\ell}(r)$ and $q\phi \rightarrow \psi_{p,\ell}(r, \phi)$, hereafter we demonstrate that pure LG modes of any radial and azimuthal indices can be generated.

The modal q-plate which converts the impinging Gaussian beam into the Laguerre Gaussian beam in opposite polarization must satisfy to the following condition

$$\mathbf{E}_{\text{out}} \cdot \mathbf{e}_{-\sigma}^* \propto u_{p,\ell}^{\text{LG}}(r, \phi, z = 0), \quad (1.10)$$

where the left side of the condition is

$$\mathbf{E}_{\text{out}} \cdot \mathbf{e}_{-\sigma}^* = E_0 i e^{-i\omega t} e^{ikLn_o} e^{-\frac{r^2}{w_0^2}} \sin \frac{\Delta(r)}{2} e^{i(2\sigma\psi(r,\phi) + \frac{\Delta(r)}{2})}, \quad (1.11)$$

while the Laguerre Gaussian field at $z = 0$ plane and at $t = 0$ moment of time is obtained from the general representation of Laguerre Gaussian beams (see 1)

$$u_{p,\ell}^{\text{LG}}(r, \phi, z = 0) \propto \left(\frac{\sqrt{2}r}{w} \right)^{|\ell|} e^{-\frac{r^2}{w^2}} e^{i\ell\phi} L_p^{|\ell|} \left(\frac{2r^2}{w^2} \right). \quad (1.12)$$

Inserting Eqs. 1.9 and 1.12 into Eq. 1.10, one gets the conditions of retardation and azimuth profiles for the modal q-plate

$$\Delta_{p,\ell}(r) = 2 \arcsin \left[\frac{|u_{p,\ell}^{\text{LG}}(r, w)| e^{\frac{r^2}{w_0^2}}}{\max_r \left[|u_{p,\ell}^{\text{LG}}(r, w)| e^{\frac{r^2}{w_0^2}} \right]} \right], \quad (1.13)$$

$$\psi_{p,\ell}(r, \phi) = \frac{\ell\phi}{2} \sigma - \frac{\Delta_{p,\ell}(r)}{4} \sigma - \left(1 - S \left[L_p^{|\ell|} \left(\frac{2r^2}{w^2} \right) \right] \right) \frac{\pi}{2}, \quad (1.14)$$

where the waist radiuses of the incident Gaussian, w_0 , and the converted Laguerre Gaussian, w , beams can be different. In general, the birefringent retardation can take both positive and negative values depending on the sign of $n_e(r, \phi) - n_o(r, \phi)$ difference. However, to our knowledge, such materials exhibiting both positive and negative values of birefringent phase retardation are relatively more challenging to realize technologically. Consequently, in order to have positive birefringent phase retardation, the sign change of LG field, which is coming in higher radial modes of LG beams, is accounted inside the azimuthal profile of modal q-plate by the factor $S(\cdot)$ step function. Step function returns 0 for negative argument and 1 for positive argument.

Finally, we can confirm that the Gaussian beam of w_0 waist radius passing through the anisotropic layer with the retardation and azimuth profiles of Eq. 1.13 and Eq. 1.14 equations, in opposite circular polarization will get the Laguerre Gaussian form of w waist radius and p, ℓ modes. This means that the modal q-plate has to be placed in the crossed-circular polarizers in general. First circular polarizer provides the circular incidence of Gaussian beam and the second circular polarizer filters the cross-circular part of the beam, which supposed to be the converted Laguerre Gaussian beam.

Importantly, only the circular polarization flipped part of the beam (from \mathbf{e}_σ to $\mathbf{e}_{-\sigma}$) inherits the Laguerre Gaussian form from the mask, which affects the efficiency of the Laguerre Gaussian mode shaper. In order to quantify it, we

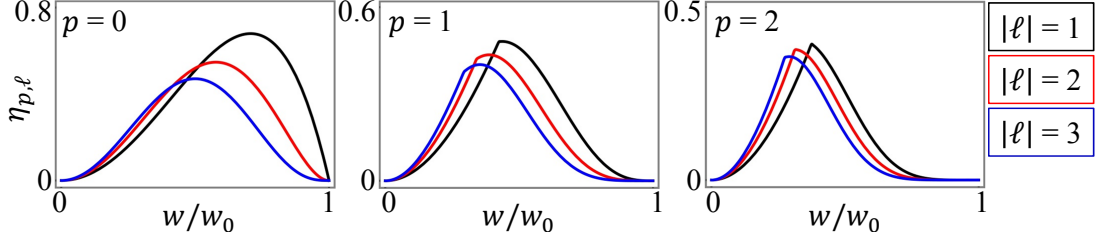


Figure 1.2: Modal q-plate efficiency dependencies on w/w_0 relation, where w_0 is the waist radius of incident Gaussian beam and w is the waist radius of converted $|\ell| = (1, 2, 3)$ and $p = (0, 1, 2)$ Laguerre Gaussian beams.

define the conversion efficiency as the ratio between the power of the generated LG mode and the total output power. Namely,

$$\eta_{p,\ell} = \frac{\int_0^\infty |\mathbf{E}_{\text{out}} \cdot \mathbf{e}_{-\sigma}|^2 r dr}{\int_0^\infty |\mathbf{E}_{\text{out}}|^2 r dr} = \frac{4}{w_0^2} \int_0^\infty e^{-\frac{2r^2}{w_0^2}} \sin^2(\Delta_{p,\ell}(r)/2) r dr, \quad (1.15)$$

where it is accounted that $\int_0^\infty |\mathbf{E}_{\text{out}}|^2 r dr = \int_0^\infty \exp(-\frac{2r^2}{w_0^2}) r dr = w_0^2/4$. Note that the efficiencies of modal q-plates with $\pm\ell$ azimuthal indices are the same, because $\Delta_{p,\ell} = \Delta_{p,-\ell}$

As a matter of fact, the efficiency of modal q-plate depends on the ratio $0 < w/w_0 < 1$. First let's discuss the particular case of $p = 0$, which is the most common situation encountered in LG beam generation. In that case, Eqs. 1.13, 1.14 and 1.15 can be simplified into the following explicit analytical expressions:

$$\Delta_{0,\ell}(r) = 2 \arcsin \left(\frac{e^{-\frac{r^2}{w^2} + \frac{|\ell|}{2} \left(\frac{r}{W}\right)^{|\ell|}}}{(|\ell|/2)^{|\ell|/2}} \right), \quad (1.16)$$

$$\psi_{0,\ell}(r, \phi) = \frac{\sigma}{2} \left(\ell\phi - \frac{\Delta_{0,\ell}(r)}{2} \right), \quad (1.17)$$

$$\eta_{0,\ell} = \left(\frac{w}{w_0} \right)^2 \left(1 - \left(\frac{w}{w_0} \right)^2 \right)^{|\ell|} \left(\frac{e}{|\ell|} \right)^{|\ell|} |\ell|!, \quad (1.18)$$

where $W = w_0 w / \sqrt{w_0^2 - w^2}$ is the characteristic waist radius of modal q-plate defined by the waist radiuses of incident and converted beams. Having the analytical expression of efficiency one can obtain the w/w_0 optimum relation which corresponds to the maximum efficiency, namely when

$$\frac{w}{w_0} = \sqrt{1/(1+|\ell|)}, \quad \eta_{0,\ell}^{\text{max}} = \frac{|\ell|! e^{|\ell|}}{(1+|\ell|)^{1+|\ell|}}. \quad (1.19)$$

	$ \ell = 1$	$ \ell = 2$	$ \ell = 3$	$ \ell = 4$	$ \ell = 5$	$ \ell = 6$
$p = 0$	0.68	0.55	0.47	0.42	0.38	0.35
$p = 1$	0.48	0.44	0.40	0.38	0.35	0.34
$p = 2$	0.39	0.38	0.36	0.34	0.33	0.31
$p = 3$	0.33	0.34	0.34	0.31	0.30	0.29
$p = 4$	0.29	0.30	0.30	0.29	0.29	0.28
$p = 5$	0.25	0.27	0.28	0.27	0.27	0.27

Table 1.1: The maximum $\eta_{p,\ell}^{\max}$ efficiency values of different modal q-plates.

	$ \ell = 1$	$ \ell = 2$	$ \ell = 3$	$ \ell = 4$	$ \ell = 5$	$ \ell = 6$
$p = 0$	0.71	0.58	0.50	0.45	0.41	0.38
$p = 1$	0.44	0.39	0.35	0.33	0.31	0.29
$p = 2$	0.38	0.32	0.29	0.27	0.26	0.25
$p = 3$	0.34	0.29	0.26	0.24	0.23	0.22
$p = 4$	0.32	0.27	0.25	0.23	0.21	0.20
$p = 5$	0.30	0.26	0.24	0.22	0.20	0.19

Table 1.2: The optimum w/w_0 relation values of different modal q-plates.

When $p \neq 0$, the retardation and azimuth profiles of modal q-plate as well as the conversion efficiency are evaluated numerically. The dependence of $\eta_{p,\ell}$ on w/w_0 for the $\text{LG}_{p,\ell}$ mode with $|\ell| = (1, 2, 3)$ and $p = (0, 1, 2)$ indices is shown in Fig 1.2. The tables of maximum efficiencies, $\eta_{p,\ell}^{\max}$, and corresponding optimum values of w/w_0 relations for different azimuthal and radial indices of modal q-plates are presented in tables. 1.1 and 1.2, respectively. Then we illustrate in Figs. 1.3 and 1.4 the corresponding retardation and azimuth profiles for such optimal modal q-plates for $p = (0, 1, 2)$ and $|\ell| = (1, 2, 3)$.

Summarising, we have presented in this section a new kind of optical element, enabling the transformation of an incident Gaussian beam into Laguerre Gaussian beam with arbitrary radial and azimuthal indices.

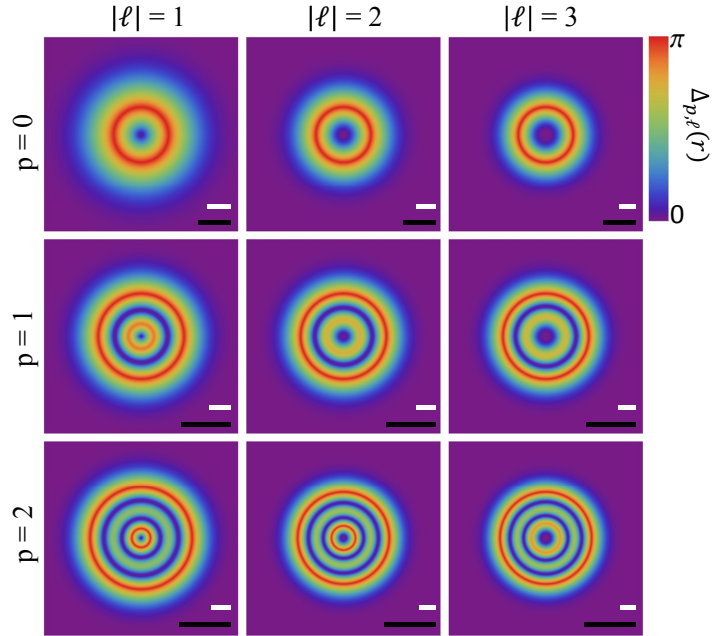


Figure 1.3: Retardation profiles of modal q-plates for maximum conversion efficiency for $p = (0, 1, 2)$ and $|\ell| = (1, 2, 3)$. The white and black lines refer to the waist radiuses of converted Laguerre Gaussian, w , and incident Gaussian, w_0 , beams.

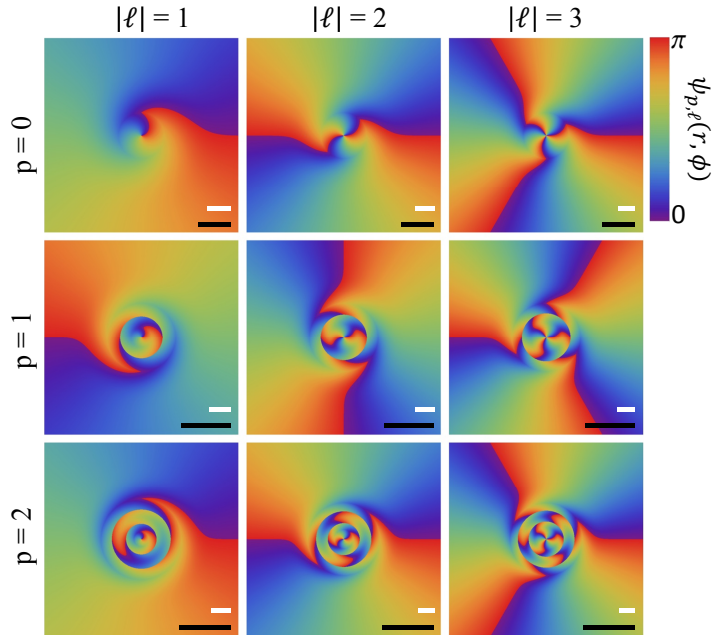


Figure 1.4: Azimuth profiles of modal q-plates for maximum conversion efficiency for $p = (0, 1, 2)$ and $|\ell| = (1, 2, 3)$. The white and black lines refer to the waist radiuses of converted Laguerre Gaussian, w , and incident Gaussian, w_0 , beams.

1.1.4 From modal q-plates to modal HG-plates

In this section we propose to generalize the concept of modal q-plate reported in Sec. 1.1.1 and Sec. 1.1.3, saying that the combined use of dynamic and geometric phases of light acquired from space-variant birefringent phase retardation and azimuth profiles of matter can transform an incident Gaussian beam into arbitrary paraxial field. To support that idea, we introduce modal HG-plates enabling the transformation of an incident Gaussian beam into a Hermite Gaussian beam with arbitrary indices, see Eq. 2. In contrast to Laguerre Gaussian beam, Hermite Gaussian beams are radially not symmetric. Consequently, here we need to use the birefringent phase retardation profiles that depend both on the radial and azimuthal coordinates, r and ϕ . On the other hand, although Hermite Gaussian beams do not possess helical wavefronts, the azimuth profile must also depend on r and ϕ in order to compensate the phase term $\exp[i\Delta(r, \phi)/2]$ in Eq. 1.9.

The modal HG-plate which converts the impinging Gaussian beam into the Hermite Gaussian beam in opposite polarization must satisfy to the following condition

$$\mathbf{E}_{\text{out}} \cdot \mathbf{e}_{-\sigma}^* \propto u_{n,m}^{\text{HG}}(x, y, z = 0), \quad (1.20)$$

where the left part of the equation can be obtained from Eq. 1.9 and the Hermite Gaussian beam at $z = 0$ plane and at $t = 0$ moment of time is obtained from the general representation of Hermite Gaussian beams (see Eq. 2)

$$u_{n,m}^{\text{HG}}(x, y, z = 0) = \frac{C_{n,m}}{w} e^{-\frac{x^2+y^2}{w^2}} H_n\left(\frac{\sqrt{2}x}{w}\right) H_m\left(\frac{\sqrt{2}y}{w}\right), \quad (1.21)$$

Inserting Eq. 1.21 into Eq. 1.20 one obtains the conditions of retardation and azimuth profiles for the modal HG-plate

$$\Delta_{n,m}(x, y) = 2 \arcsin \left[\frac{|u_{n,m}^{\text{HG}}| e^{\frac{x^2+y^2}{w_0^2}}}{\max_r \left[|u_{n,m}^{\text{HG}}| e^{\frac{x^2+y^2}{w_0^2}} \right]} \right], \quad (1.22)$$

$$\psi_{n,m}(x, y) = -\frac{\Delta_{n,m}(x, y)}{4} \sigma - \left(1 - S \left[H_n\left(\frac{\sqrt{2}x}{w}\right) H_m\left(\frac{\sqrt{2}y}{w}\right) \right] \right) \frac{\pi}{2}. \quad (1.23)$$

As in the case of modal q-plate, here also the argument of $\arcsin(\cdot)$ is taken to be always positive in order to have positive birefringent phase retardation, meanwhile the sign is accounted in the azimuth profile by the step function $S(\cdot)$.

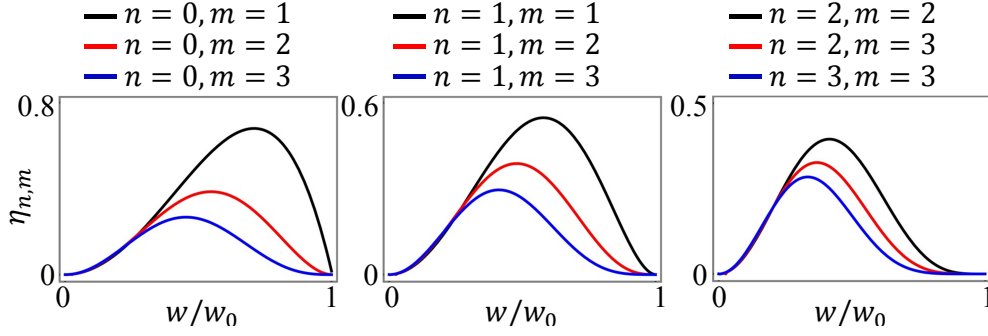


Figure 1.5: Modal HG-plate efficiency dependencies on w/w_0 relation value, where w_0 is the waist radius of incident Gaussian beam and w is the waist radius of converted Hermite Gaussian beams.

	$n = 0$	$n = 1$	$n = 2$	$n = 3$	$n = 4$	$n = 5$
$m = 0$		0.34	0.19	0.13	0.1	0.1
$m = 1$	0.34	0.27	0.19	0.15	0.12	0.1
$m = 2$	0.19	0.19	0.16	0.13	0.11	0.1
$m = 3$	0.13	0.15	0.13	0.11	0.1	0.09
$m = 4$	0.1	0.12	0.11	0.1	0.09	0.08
$m = 5$	0.08	0.01	0.01	0.09	0.08	0.08

Table 1.3: The maximum $\eta_{n,m}^{\max}$ efficiency of different modal HG-plates

	$n = 0$	$n = 1$	$n = 2$	$n = 3$	$n = 4$	$n = 5$
$m = 0$		0.71	0.55	0.45	0.39	0.35
$m = 1$	0.71	0.58	0.48	0.41	0.36	0.33
$m = 2$	0.55	0.48	0.42	0.37	0.33	0.31
$m = 3$	0.45	0.41	0.37	0.33	0.31	0.29
$m = 4$	0.39	0.36	0.33	0.31	0.29	0.27
$m = 5$	0.35	0.33	0.31	0.29	0.27	0.25

Table 1.4: The optimum w/w_0 relation values of different modal HG-plates

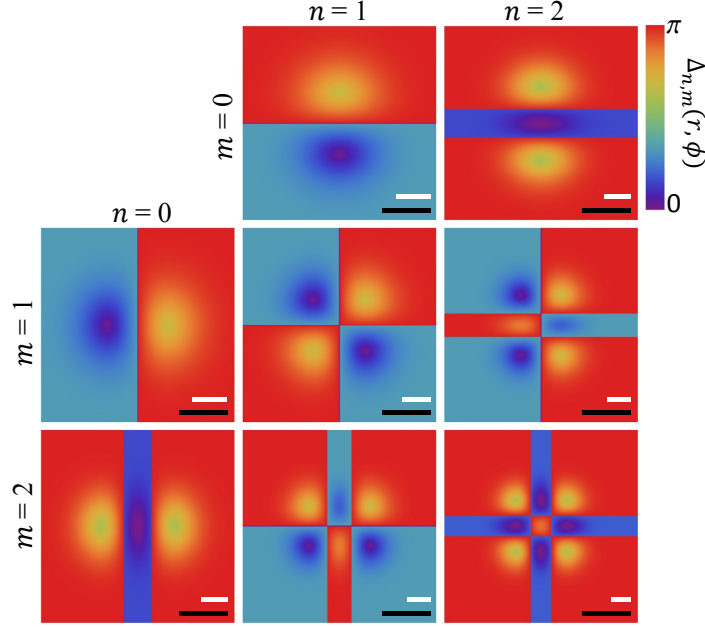


Figure 1.6: Retardation profiles of modal HG-plates for maximum conversion efficiency for $n = (0, 1, 2)$ and $m = (0, 1, 2)$. The white and black lines refer to the waist radii of converted Hermite Gaussian, w , and incident Gaussian, w_0 , beams.

The Gaussian beam is radially symmetric and most of the power is concentrated in central part. Meanwhile, the Hermite Gaussian beams are not radially symmetric and their power is concentrated out of central region. Consequently we expect that the modal HG-plates are less efficient than the modal q-plates, while the dependencies on w/w_0 remains. This is illustrated in Fig. 1.5, where the conversion efficiency, $\eta_{n,m}$, is plotted as a function of w/w_0 for $n = (0, 1, 2, 3)$ and $m = (0, 1, 2, 3)$. The Hermite Gaussian beams with (n, m) and (m, n) modes are the same beams just rotated by $\pi/2$ in the (x, y) transverse plane, that is why the efficiency curves of modes (n, m) or (m, n) will have the same form. For that reason, we present in Fig. 1.5 only one of them. The tables of maximum efficiencies, $\eta_{n,m}^{\max}$, and corresponding optimum values of w/w_0 relations for $n = (0, 1, 2, 3, 4, 5)$ and $m = (0, 1, 2, 3, 4, 5)$ modes are presented in tables 1.4 and 1.3, respectively. Then we illustrate in Fig. 1.6 and 1.7 the corresponding retardation and azimuth profiles for such optimal modal HG-plates for $n = (0, 1, 2)$ and $m = (0, 1, 2)$

Summarising, we have presented in this section another modal beam shaper, which can shape the incident Gaussian beam into Hermite Gaussian beam of arbitrary modes. Consequently, we claim that such concept of combining geometric and dynamic phases from single optical element, can provide a beam shaper of any other paraxial beam as well.

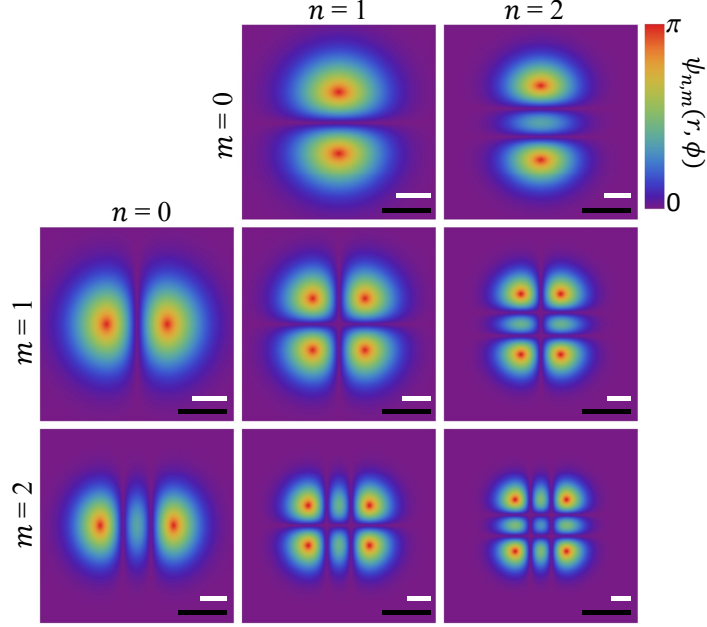


Figure 1.7: Azimuth profiles of modal HG-plates for maximum conversion efficiency for $n = (0, 1, 2)$ and $m = (0, 1, 2)$. The white and black lines refer to the waist radiuses of converted Hermite Gaussian, w , and incident Gaussian, w_0 , beams.

1.2 Towards experimental realization: quasi-modal q-plates

1.2.1 The limit of small retardance: quasi-modality

In the previous section we have introduced theoretically the modal q-plates from inhomogeneous anisotropic media. The optical characteristics, such as birefringent phase retardation and azimuth profiles of modal q-plates, exhibit spatially varying, not smooth and technologically challenging structuring of matter (see Fig. 1.3 and Fig. 1.4). Therefore, towards an experimental realization we would like to address the following question: could an approximate modal q-plate be conceived with smooth birefringent phase retardation and azimuth profiles? Namely, $\Delta = \Delta(r)$ and $\psi = \psi(r)$. To answer this question, we propose to consider the limit of small birefringent phase retardation, that refers to the condition

$$\Delta(r) \ll \pi. \quad (1.24)$$

Indeed this allows us to consider series expansion of Eq. 1.9, namely

$$\begin{aligned} \mathbf{E}_{\text{out}} = & \frac{E_0}{2} e^{-i\omega t} e^{ikLn_o} e^{-\frac{r^2}{w_0^2}} \left[\left(1 + \sum_{j=0}^{\infty} \frac{(i\Delta(r))^j}{j!} \right) \mathbf{e}_{\sigma+} \right. \\ & \left. + \left(-1 + \sum_{j=0}^{\infty} \frac{(i\Delta(r))^j}{j!} \right) e^{2i\sigma\psi(r,\phi)} \mathbf{e}_{-\sigma} \right], \end{aligned} \quad (1.25)$$

where the following two identities have been used

$$\begin{aligned} e^{i\Delta(r)/2} \cos(\Delta(r)/2) &= \frac{1}{2} (1 + e^{i\Delta(r)}) = \frac{1}{2} \left(1 + \sum_{j=0}^{\infty} \frac{(i\Delta(r))^j}{j!} \right) \\ e^{i\Delta(r)/2} \sin(\Delta(r)/2) &= \frac{1}{2i} (-1 + e^{i\Delta(r)}) = \frac{1}{2i} \left(-1 + \sum_{j=0}^{\infty} \frac{(i\Delta(r))^j}{j!} \right). \end{aligned} \quad (1.26)$$

Of course, the larger number of terms kept in Eq. 1.26, the more precise it describes the output field. In this section we keep only the first two terms of series, namely

$$\mathbf{E}_{\text{out}} = E_0 e^{-i\omega t} e^{ikLn_o} e^{-\frac{r^2}{w_0^2}} \left[\left(1 + i\frac{\Delta(r)}{2} \right) \mathbf{e}_{\sigma+} + i\frac{\Delta(r)}{2} e^{2i\sigma\psi(r,\phi)} \mathbf{e}_{-\sigma} \right]. \quad (1.27)$$

Then, considering the modality condition given by Eq. 1.10 for the output field given by Eq. 1.27 and requiring that the incident and converted beams have the same waist radiuses ($w = w_0$), the retardation and azimuth profiles of quasi-modal q-plate will get the following simple forms

$$\Delta_{p,\ell}(r) = \Delta_0 \left(\frac{r}{w_0} \right)^{|\ell|} L_p^{|\ell|} \left(\frac{2r^2}{w_0^2} \right), \quad (1.28)$$

$$\psi_{p,\ell}(\phi) = \frac{\ell\phi}{2} \sigma, \quad (1.29)$$

where Δ_0 is a constant given by Eq. 1.24.

A quasi-modal q-plate is associated with a smooth birefringent phase retardation and azimuth profiles, i.e. $\Delta(r)$ is a polynomial function of radial distance and $\psi(\phi)$ is a linear function of azimuth angle. The practical consequence is that the realization of quasi modal q-plates is much less demanding from fabrication point of view. Still, such good points in favor of quasi-modal q-plate should be consolidated by the analysis of converted beam modality and conversion efficiency which we address in what follows.

1.2.2 Quantitative modal analysis

According to the definition of Eq. 1.15 for given p and ℓ modes the conversion efficiency is proportional to $\eta_{p,\ell} \propto \Delta_0^2$. Consequently, the larger value of Δ_0 , the

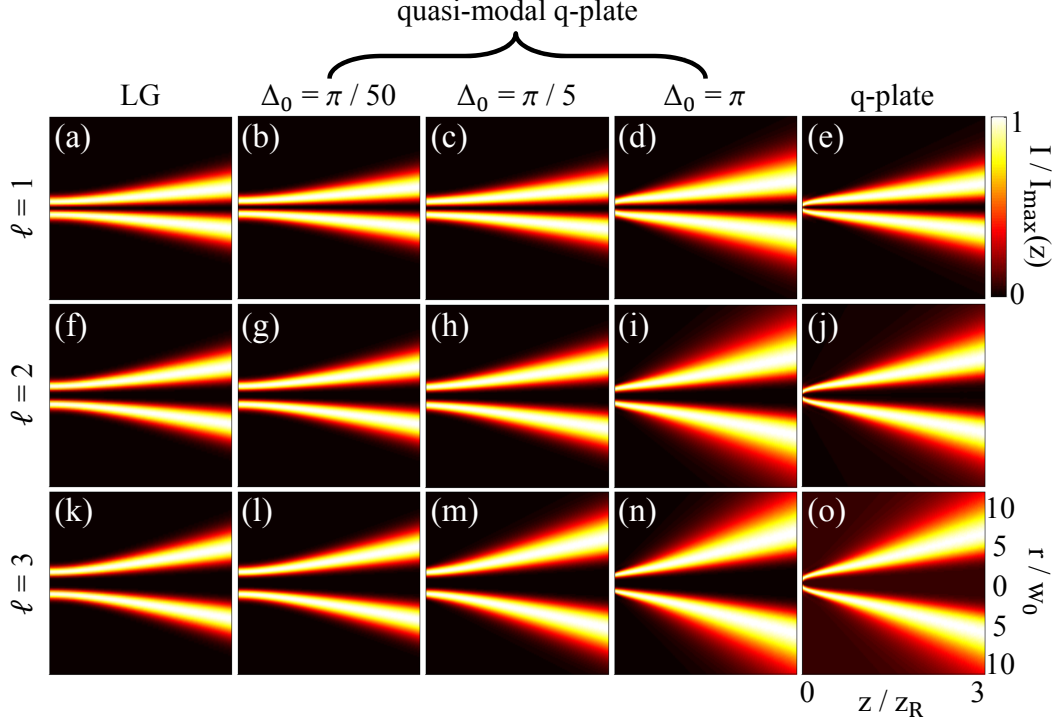


Figure 1.8: Comparative study of the diffraction of an incident Gaussian beam on different quasi modal q-plates (second, third, and fourth columns) and on the conventional q-plate (fifth column) with a diffraction of perfect LG beam (first column), for $p = 0$ and $\ell = (1, 2, 3)$. See the text for details.

higher the efficiency. However, large values of Δ_0 bring more imperfections in converted mode, since the condition Eq. 1.24 is less satisfied. A trade off thus naturally emerges: indeed, the value of Δ_0 should be small enough to satisfy the Eq. 1.24 and large enough to have a decant conversion efficiency, especially in view of the experimental demonstration.

To see the influence of Δ_0 on the quality of the modal conversion, we perform a numerical study of the diffraction of an incident Gaussian beam passing through the quasi modal q-plates with $\ell = (1, 2, 3)$ and $p = 0$ indices. There are various options to evaluate the diffracted field. One of them is the Kirchhoff-Fresnel diffraction equation, that is directly derived from the wave equation, from which we can derive approximated versions depending on the observation plane. For instance, the Fraunhofer diffraction approximation of the Kirchhoff equation applies to the far field, while the Fresnel diffraction approximation applies to the Rayleigh range field (for more information see the book [82]). Here we use another approach of beam propagation based on fast Fourier transforms. It consists of successive two-dimensional fast Fourier and inverse fast Fourier transforms (\mathcal{F} and \mathcal{F}^{-1}) in order to mimic incremental propagation step along the propagation

direction (here given by the z axis). According to that method, the original field $u_0(x, y) = u(x, y, z = 0)$ propagating over a distance z , $u_z = u(x, y, z)$ is expressed as

$$u_z = \mathcal{F}^{-1} \left(\mathcal{F}(u_0) \cdot e^{ik_z z} \right), \quad (1.30)$$

which is valid as long as the z -component of the wave vector, k_z , is not changed during propagation, for instance in homogeneous linear isotropic media, which applies to our case since we are considering a free space propagation.

The results of simulations are summarised in Fig. 1.8, where we compose different cases for $p = 0$: pure LG beam (first column), quasi-modal q-plates between crossed-circular polarizers for $\Delta_0 = \pi/50$ (second column), $\Delta_0 = \pi/5$ (third column), $\Delta_0 = \pi$ (fourth column) and conventional q-plate satisfying the half-wave plate condition (fifth column). First, second and third rows correspond to azimuthal indices $\ell = (1, 2, 3)$. The propagation axis, z , is normalized according to the Rayleigh length defined by $z_R = \pi w_0^2 / \lambda$. Finally, the radial profiles of the intensity distribution at each propagation distance, z , is normalized according to its maximum value, which ease the comparison between the different cases by mere visual inspection.

1.2.3 Fabrication and optical characterization of quasi-modal q-plates

Three glassy quasi modal q-plates with $\ell = (1, 2, 3)$ and $p = 0$ have been fabricated based on the retardation and azimuth profiles given by Eq. 1.28 and 1.29, see Fig. 1.9(a). In practice, we chose $\Delta_0 = \pi/5$ (Fig. 1.8 (c, h, m)) as a trade off between the validity of small retardation limit and conversion efficiency, which evaluated from Eq. 1.15 is approximately $\eta \simeq 0.05$ for each plate.

The plates have been fabricated by Altechna R & D company using femtosecond direct laser writing of self-assembled nanostructures in the bulk of silica glass [83]. In fact, depending on the parameters of focused writing laser, self-organized stripe-like structures appear with width of ~ 20 nm forming a grating with periods of 140–130 nm. Such subwavelength structuring induces birefringent phase retardation. Interestingly, depending of the power and irradiation rate of writing laser one can control the period and depth of the grating. That lead to the possibility of fabrication of space-variant birefringent plates, whose retardance and optical axis azimuth can a priori be controled at will. However, we stress that the realization of quasi-modal q-plates was already a technological challenge.

The images of fabricated quasi-modal q-plates observed between crossed-linear polarizers are shown in Figs. 1.9(b,c,d), that allow easy identification of the

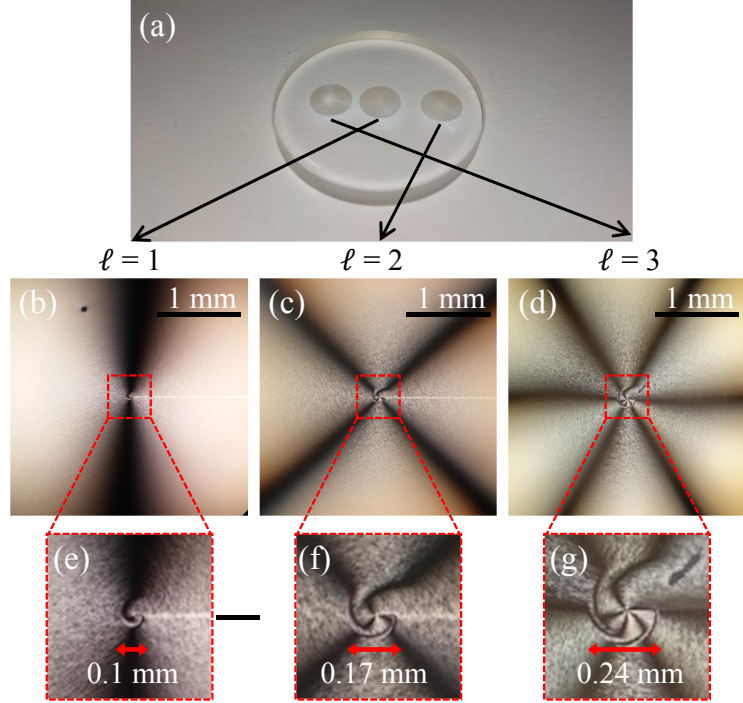


Figure 1.9: (a) Fabricated quasi-modal q -plates with $\ell = (1, 2, 3)$ azimuthal indices by Altechna R & D company. (b,c,d) Their images observed between crossed-linear polarizers. (e,f,g) Enlargement of central parts of panels (b,c,d).

charge q , since the number of dark brushes equal to $2q$. Indeed one can show by simple Jones calculation that such intensity pattern is proportional to $\sin^2(2\psi)$

Further optical characterization is made using Abrio imaging system, which is able to measure the birefringent phase retardation and optical axis azimuth maps of the sample (the maximum measurable retardation value is π and the minimum is a few tens of picometers at 546 nm wavelength). Fig. 1.10 shows the birefringent phase retardation and optical axis azimuth profiles of the fabricated quasi-modal q -plates. Indeed the retardation profiles are normalized according to 633 nm wavelength, since in our further experimental studies we use a laser of 633 nm wavelength. Retardation profiles confirm a good level of axisymmetry, as expected from our design, while the azimuth profiles reveal the topological material structuring with charge q .

A quantitative analysis then can be done for the retardation profile analysis via azimuth averaging, namely $\Delta_{\text{exp}}^{\text{av}}(r) = (1/2\pi) \int_0^{2\pi} \Delta_{\text{exp}}(r, \phi) d\phi$, see blue curves in Fig. 1.11. Measurements are compared with the theoretical expressions given by Eq. 1.28 for $\Delta_{0,\ell}(r)$ for $\ell = (1, 2, 3)$. The fabricated quasi-modal q -plates do not have zero central retardation due to the technological limitations to induce

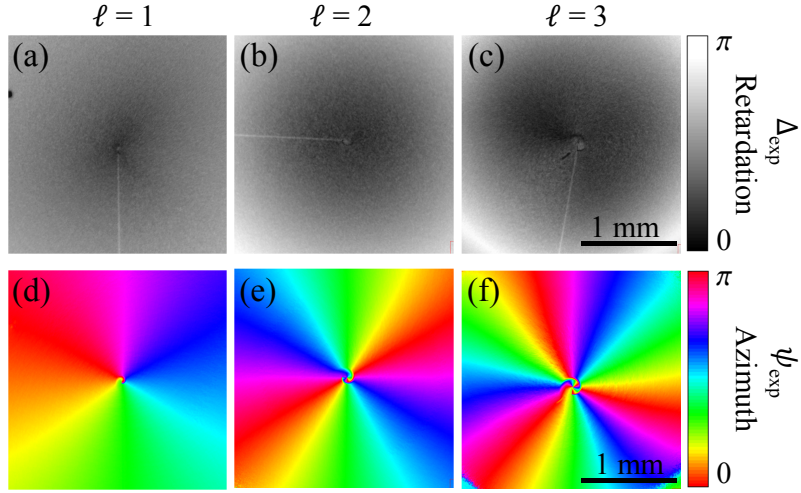


Figure 1.10: (a,b,c) The birefringent phase retardation profiles at 633 nm wavelength of fabricated quasi-modal q-plates measured by Abrio imaging system. (d,e,f) The optical axis azimuth profiles of fabricated quasi-modal q-plates measured by Abrio imaging system.

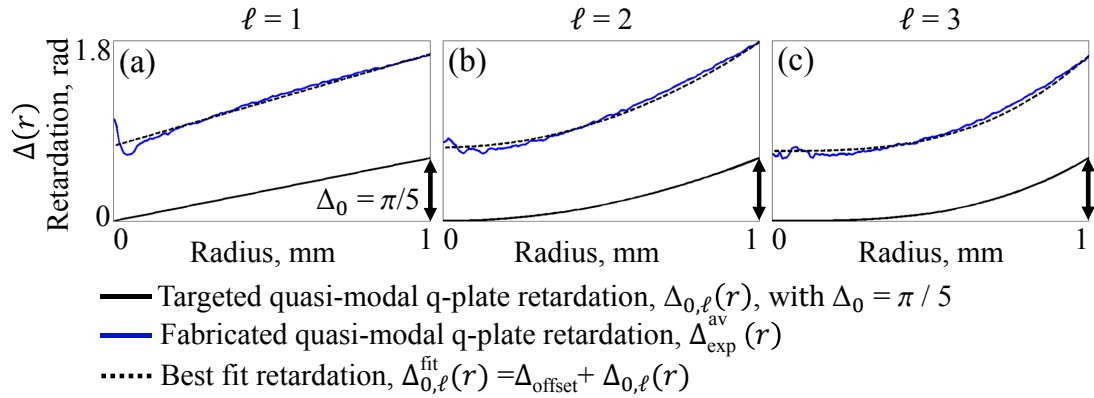


Figure 1.11: (a,b,c) The blue lines correspond to the azimuthal averaged retardation profiles of $\ell = (1, 2, 3)$ quasi-modal q-plates (originals are presented in Figs. 1.10(a,b,c)) measured by Abrio imaging system. The black solid curves correspond to the theoretical profiles from Eq. 1.28 for $\ell = (1, 2, 3)$. The black dashed lines correspond to $\Delta_{0,\ell}^{\text{fit}}(r)$ best polynomial fits to experimental data.

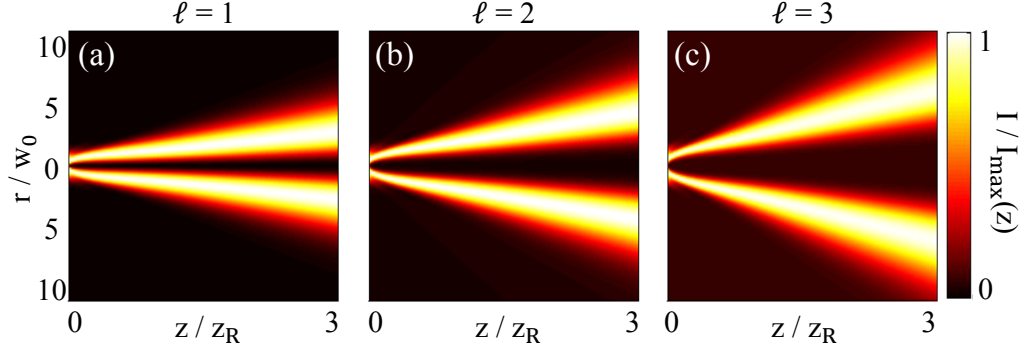


Figure 1.12: The diffraction of an incident Gaussian beam on quasi modal q-plates with $\Delta_{0,\ell}^{\text{fit}}(r)$ profiles for $\ell = (1, 2, 3)$.

zero retardation in general, as well as due to their large central defect sizes. Indeed, Figs. 1.9(e,f,g) are the enlarged central regions of fabricated quasi-modal q-plates for $\ell = (1, 2, 3)$ and show that their central defects have approximately 0.1 mm, 0.17 mm and 0.24 mm sizes, respectively. However, we see that $\Delta_{\text{exp}}^{\text{av}}(r)$ retardation curves are shifted up keeping their qualitative polynomial behaviour. To support our statement, we have showed also the fitting curves $\Delta_{\text{fit}}(r) = \Delta_{\text{offset}} + \Delta_{0,\ell}(r)$ (black dashed lines) corresponding to the same polynomial functions of $\Delta_{0,\ell}(r)$, but shifted up by constant offset Δ_{offset} .

Of course the deviation of retardation profiles will influence on the expected quality of converted beams. To estimate that we present in Fig. 1.12 the diffraction plots of incident Gaussian beams on the quasi-modal q-plates placed between crossed-circular polarizers and having $\Delta_{\text{fit}}(r)$ retardation profiles of Fig. 1.11 (see black dashed curves). It is seen that the new diffraction plots exhibit less similarity to the diffraction of LG beams than the ones based on initially planned retardation profiles (see Fig. 1.8(c,h,m)). However, they are still better than the Gaussian beam diffraction after ideal q-plates (see Fig. 1.8(e,j,o)). The main reason of better quality is that, though the retardation profiles of fabricated quasi-modal q-plates are deviated from $\Delta_{\text{exp}}^{\text{av}}(r)$, they still have the same power low.

1.2.4 Experimental demonstration of quasi-modality

Once the structures of fabricated quasi-modal q-plates have been characterized, the next experimental step consists in studying the Gaussian beam propagation through the mentioned quasi-modal q-plates. The quasi-modal q-plate is placed between crossed circular polarizers in order to select only the converted quasi-modal vortex beam. The experimental setup is presented in Fig. 1.13(a). The wavelength, waist radius and Rayleigh length of the incident Gaussian beam are $\lambda = 633$ nm, $w_0 = 1$ mm and $z_R = 4$ m, respectively. Consequently we can easily

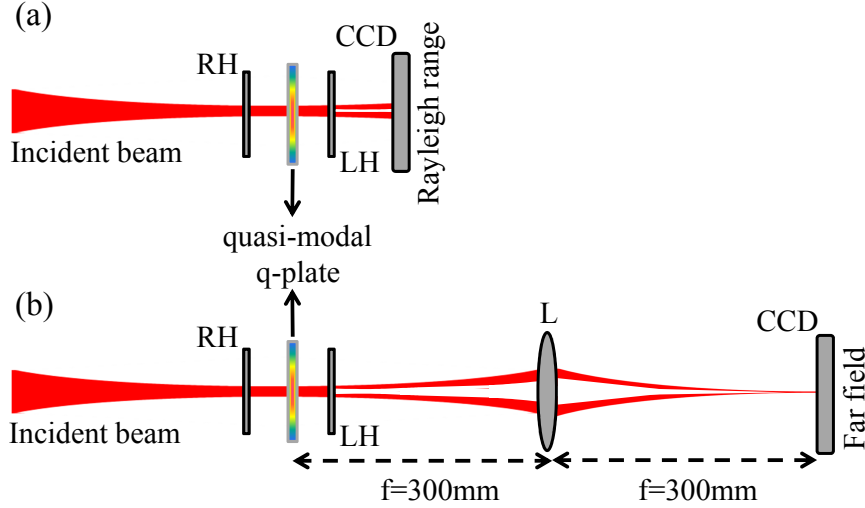


Figure 1.13: (a) Experimental setup to study the transmitted beam in the Rayleigh range from quasi-modal q-plates and conventional q-plates with azimuthal $\ell = (1, 2, 3)$ indices placed between crossed-circular polarizers. (b) Experimental setup to study the transmitted far fields from quasi-modal q-plates and conventional q-plates of $\ell = (1, 2, 3)$ azimuthal indices placed between crossed-circular polarizers. RH: right-handed circular polarizer, LH: left-handed circular polarizer, L: spherical lens with focal length $f = 300$ mm, CCD: imaging camera.

study the transmitted field at distance of the order of the Rayleigh range by placing a camera in the course of the output beam, see Fig. 1.13(a). Finally, for the sake of comparison, we repeat all the measurements for the conventional q-plates of same charges made by the same femtosecond direct laser writing technology and also from Altechna R & D.

Fig. 1.14 shows the converted beams intensity profiles on logarithmic scale after quasi-modal q-plates or conventional q-plates at different propagation distances, namely, $z = z_R/2, z_R, 2z_R$. One can see that the detected doughnuts of quasi modal q-plates are less distorted in comparison with the detected doughnuts of conventional q-plates with the same azimuthal indices. We note, that the theoretical diffraction plots of Fig. 1.12 of fabricated quasi-modal q-plates compared with the expected diffraction plots of Fig. 1.8(c,h,m) of original design suggest that there is room for improvement regarding the uncontrolled central area and technological limitation towards the zero retardation inducement.

The second experimental setup shown in Fig. 1.13(b) is then used in order to compare the far fields of incident Gaussian beams passing through the quasi-modal q-plates (see Figs. 1.15 (d,e,f)) and just after the conventional q-plates of the same charges (see Figs. 1.15(j,k,l)). We have used a lens of $f = 300$ mm focal length in $f-f$ optical configuration with respect to the q-plate and CCD camera in order to conjugate the far field of output light at imaging plane of camera, see

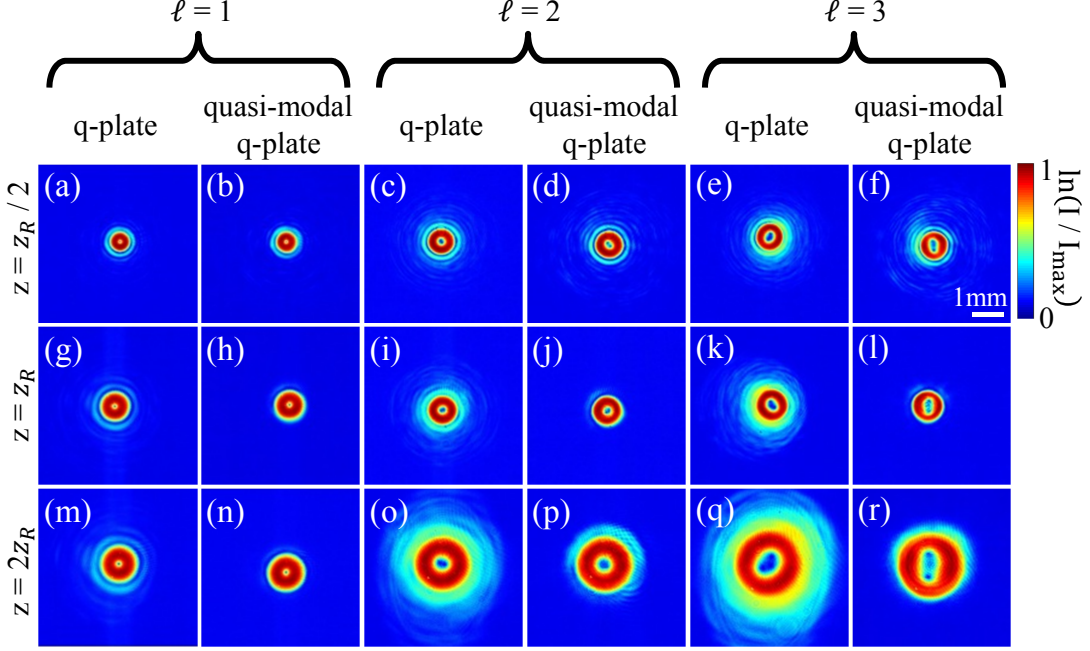


Figure 1.14: The converted beams intensity profiles on logarithmic scale after quasi-modal q-plates (a, c, e) or ideal q-plates (b, d, f) at different propagation distances.

Fig. 1.13(b). The theoretical calculations corresponding to the observed far field images of quasi-modal q-plates are done performing two-dimensional fast Fourier transform of output field component of crossed circular polarization of Eq. 1.27 with respect to the incident beam polarization, namely $E_{\text{farfield}} = \mathcal{F}(E_{\text{out}} \mathbf{e}_{-\sigma}^*)$, where the retardation profiles are taken as the best polynomial fits for quasi-modal q-plate $\Delta_{0,\ell}^{\text{fit}}(r)$ (see Fig. 1.11). Finally, the normalized intensities of calculated fields, namely I/I_{max} , where $I = |E_{\text{farfield}}|^2$, for the cases of $\ell = (1, 2, 3)$ are presented in Figs. 1.15(a,b,c), respectively. Similarly, the case of a conventional q-plate is shown in Figs. 1.15(g,h,i).

The differences between the far fields of quasi-modal q-plates and conventional q-plates in both experimental and theoretical cases are less obvious than for finite distance observations (see Fig. 1.14). Indeed, the imperfections of doughnuts, which were well visible at Rayleigh range, having a higher spatial frequencies are scattered and distributed far from main doughnuts in the far field.

In conclusion, the realization of glassy quasi-modal q-plates are a first promising step towards the realization of perfect modal q-plates. They exhibit better modality of converted beams in comparison of conventional q-plates currently used in the market. Nevertheless, the technological difficulties associated with the material structuring and its fabrication of modal q-plates led us to consider another route towards modality, by exploiting a self-engineered strategy based

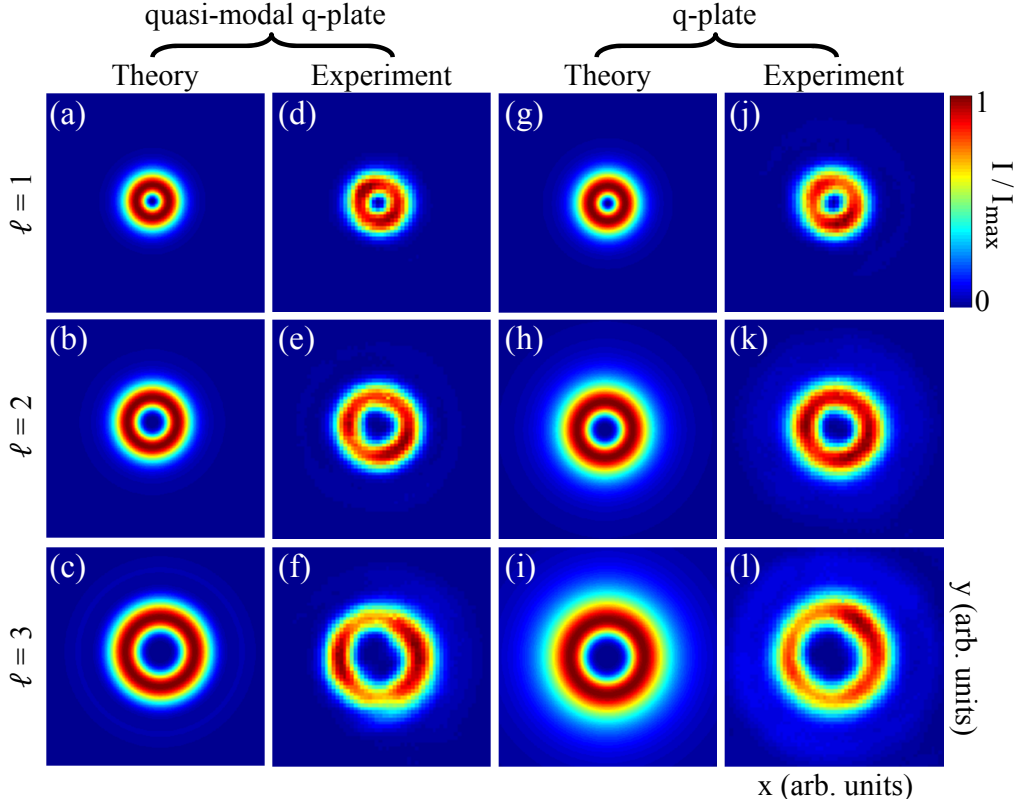


Figure 1.15: (a,b,c) The intensity profiles of output fields fast Fourier transforms of quasi-modal q-plates with $\ell = (1, 2, 3)$ placed between crossed circular polarizers. (d,e,f) Far fields of incident Gaussian beams on the fabricated quasi modal q-plates detected in the setup of Fig. 1.13(b). (g,h,i) Same as panels (a,b,c) but for the conventional q-plates with $\ell = (1, 2, 3)$. (j,k,l) Far fields of incident Gaussian beams on the conventional q-plates detected using the setup shown in Fig. 1.13(b).

on the use of liquid crystal topological defects, which is the purpose of the next section.

1.3 Liquid crystal umbilical defects and their modality

Over the past two decades, liquid crystals (LCs) have established their place in singular optics as an anisotropic and inhomogeneous optical materials [84, 85]. The long-range optical orientational order of the local averaged molecular axis (called director \mathbf{n} , a unit vector satisfying $\mathbf{n} = -\mathbf{n}$) and possible high birefringence allow the design of optical elements enabling on-demand shaping of the phase, amplitude or polarization of an incident light field. One of the most in-

teresting feature arises from the “soft” properties of liquid crystals is their ability to self-organize into topological defects with or without the presence of external fields (thermal, electrical, magnetic, electromagnetic, etc) [86]. Liquid crystal topological defects possess inherent structuring of their optical axis allowing to shape the incident Gaussian beam into vortex beam via spin-orbit interaction of light, indeed they have been unveiled to behave as artificially structured LC q-plates [12, 13, 87, 88]. Substantial research efforts were devoted to the development of methods to control the generation, evolution, topology, and optical properties of LC topological defects towards an agile control of structured light fields.

In practice, quasi-static electric fields are the most common external fields used so far to realize or tune self-organized LC defects, which is achieved by using LC layer sandwiched between two glass substrates provided with transparent electrodes [12, 89]. An alternative option consists to use LC light valves driven by either AC or DC electric fields. In that case, the applied electric field is spatially shaped according to the intensity spatial distribution of illuminating light [90, 91]. Under specific conditions, the light itself can also do the job and induce topological defects due to the nonlinear orientation of LC director. In that case, the light creates its own q-plate that eventually lead to self-induced optical vortex generation [92–94]. Recently, topological defects induced by magnetic fields (created by small NdFeB magnets) or light-driven heating effects have been investigated too [95, 96].

In this section we will discuss a three-dimensional director field called umbilical topological defect [97] that appears in nematic films with perpendicular alignment boundary conditions and negative dielectric anisotropy [98, 99]. Umbilics are nonsingular topological defects enabling the generation of singular light fields (such as vortex beams, Bessel-Gauss beams, LG beams etc.) from nonsingular incident beams. The electric field is generated by applying low-frequency voltage to the glass substrates provided with transparent electrodes. In that case, it is known that the operating wavelength and the operation mode of the vortex generator can be tuned in real time by mere control of the applied voltage [89]. Furthermore, it has been also shown that a single umbilical defect is able to modulate the spatial characteristics and the number of concentric rings of the generated singular vortex beam [12]. Such rich electrically tunable properties of umbilical defects in nematic LCs encourage us to investigate their modality, and hopefully identify the conditions leading to pure modal beam shaping capabilities.

To date, singular optics studies on umbilical defects were mainly restricted to the modification of the azimuthal index ℓ of a light beam by an amount of ± 2 , due to the strength values that are restricted to $s = \pm 1$. However, the formation of other anisotropic structures with higher charges in LCs are also possible [13, 100], which could trigger further studies on the modality of vortex beams shaped by

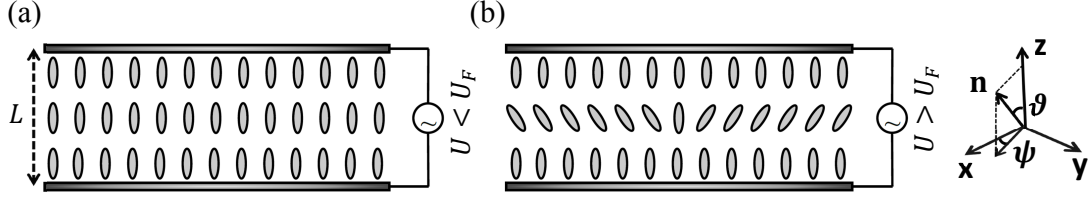


Figure 1.16: (a) Sketch of the liquid crystal film sandwiched by two glass substrates ensuring a perpendicular alignment of LC molecules at boundaries, under the voltage below Fréedericksz transition threshold value, $U < U_F$. (b) Sketch of same liquid crystal sample under the voltage above Fréedericksz transition threshold value, $U > U_F$. The laboratory Cartesian coordinate frame (x, y, z) is chosen in order to have LC director oriented along the z axis at rest, and LC film boundaries parallel to the (x, y) plane. The umbilic director orientation according Rapini method is described in spherical coordinate system (n_e, ϑ, ψ) , where ϑ is the director tilt angle along z and ψ is the umbilic director azimuth.

LC defects. Therefore, exploring the modal features of umbilics can be seen as a first step towards the elaboration of advanced self-engineered topological shaping strategies.

1.3.1 Description of umbilical defects

First, let us introduce the theoretical model of umbilic 3D director structure according to the early work by A. Rapini [97]. The sketch of liquid crystal sample when applied electric field is below the Fréedericksz transition threshold value, $U < U_F$, is depicted in Fig. 1.16(a). Cartesian coordinate system (x, y, z) is selected with z axis along the unit vector of director orientation, $\mathbf{n} = (0, 0, 1)$. When the electric field is above the Fréedericksz transition threshold value, $U > U_F$, and it is applied along the z axis direction, umbilics are generated and their director orientation can be represented in (x, y, z) laboratory frame by

$$\mathbf{n} = (\sin \vartheta \cos \psi, \sin \vartheta \sin \psi, \cos \vartheta), \quad (1.31)$$

where ψ is the director azimuthal angle in the (x, y) transverse plane and ϑ is the director tilt with respect to the z axis, see Fig. 1.16(b). Following [97], if the ϑ tilt angle is small, the umbilic can be described by

$$\psi = s\phi + \phi_0, \quad (1.32)$$

$$\vartheta(r, z) = \vartheta_{\max} a(r) \sin(\pi z/L), \quad (1.33)$$

where (r, ϕ) is the polar coordinate system in (x, y) plane, ϕ_0 is a constant,

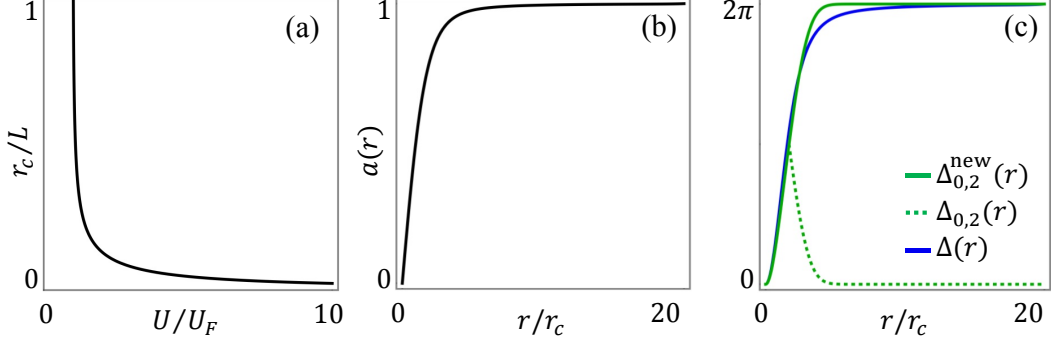


Figure 1.17: (a) The dependence of reduced core radius, r_c/L , of Rapini umbilic on applied reduced voltage U/U_F . (b) The numerical solution of reduced amplitude of Rapini umbilic. (c) The radial profile of Rapini umbilic retardation ($\Delta(r)$, blue line) combined with the radial profile of charge two modal q-plate ($\Delta_{0,2}(r)$, green dashed line), which gives best fit with umbilic retardation curve after flipping around the axis $\Delta_{0,2}(r) = \pi$.

$s = \pm 1$ is the defect strength (hereafter we will restrict the study to the case of $s = 1$), L is the film thickness, $0 \leq a \leq 1$ is the reduced tilt amplitude and

$$\vartheta_{\max} = \lim_{r \rightarrow \infty} (\max_z [\vartheta(r, z)]) , \quad (1.34)$$

is the asymptotic value of ϑ along z direction at large r . In general, it is a function of dielectric anisotropy, splay and bend Frank elastic constants and applied electric field. Finally, the profile of reduced tilt amplitude can be obtained from the following differential equation

$$\frac{d^2 a}{d\rho^2} + \frac{1}{\rho} \frac{da}{d\rho} + \left(1 - \frac{1}{\rho^2}\right) a - a^3 = 0 , \quad (1.35)$$

where $a(0) = 0$ and $a(\infty) = 1$ are the boundary conditions, $\rho = r/r_c$ is the reduced radial coordinate where $r_c = (L/\pi)(K_{\text{eff}}/K_3)^{1/2}((U/U_F)^{1/2} - 1)^{-1/2}$ is the core radius that depends on the cell thickness, applied electric field, splay elastic constant K_3 and effective elastic constant K_{eff} associated to a given umbilic (see Fig. 1.17(a), where $K_{\text{eff}} = K_2 = 9.52$ pN and $K_3 = 18.3$ pN correspond to the $s = 1$ umbilic induced in MLC2079 nematic LC mixture from Licristal used in our experiments). The numerical solution of Eq. 1.35 is depicted in Fig. 1.17(b).

Having the set of equations from Eq. 1.31 to Eq. 1.35 describing the 3D structure of an electrically induced umbilic, one can calculate the corresponding profile of the birefringent phase retardation $\Delta(r)$. In contrast to the previous sections, the umbilic structure corresponds to an optical axis with z -varying tilt angle with respect to the light propagation direction. Therefore, the evaluation of $\Delta(r)$ implies an integral evaluation of the form

$$\Delta(r) = \frac{2\pi}{\lambda} \int_0^L (n_{\text{eff}}(r, z) - n_o) dz , \quad (1.36)$$

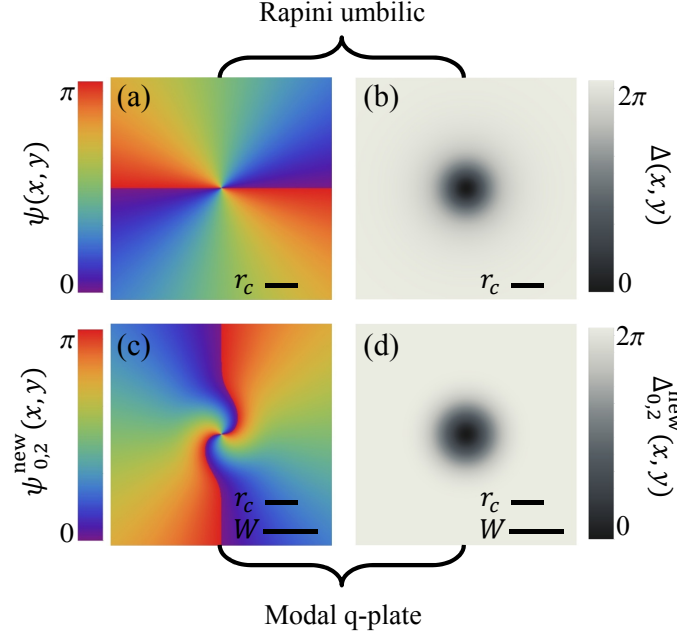


Figure 1.18: (a,b) 2D director azimuth, $\psi(x, y)$, and birefringent phase retardation, $\Delta(x, y)$, profiles of Rapini umbilic for $s = 1$ and $\phi_0 = 0$. (c,d) 2D director azimuth, $\psi_{0,2}^{\text{new}}(x, y)$, and birefringent phase retardation, $\Delta_{0,2}^{\text{new}}(x, y)$, profiles of new charge two modal q-plate.

where n_{eff} is the effective local extraordinary component of refractive index

$$n_{\text{eff}}(r, z) = \frac{n_e n_o}{(n_e^2 \cos^2 \vartheta(r, z) + n_o^2 \sin^2 \vartheta(r, z))^{1/2}}, \quad (1.37)$$

which equals the extraordinary refractive index, n_e , when the tilt angle is $\pi/2$ and the ordinary refractive index, n_o , when the tilt angle is zero. The former case corresponds to the maximum retardation, while in the latter case medium along the z direction behaves as an isotropic material associated with zero birefringent phase retardation.

Since the Rapini model implies modest director reorientation amplitude, $\vartheta_{\text{max}}^2 \ll 1$, any quantity evaluated from the director field should consistently account for this assumption. In particular, Eq. 1.37 thus expands as

$$n_{\text{eff}}(r, z) = n_o + \frac{(n_e^2 - n_o^2) n_o}{2n_e^2} \vartheta^2 + O[\vartheta]^4, \quad (1.38)$$

Consequently, inserting Eq. 1.38 into Eq. 1.36, one gets

$$\Delta(r) = \Delta_{\infty} a(r)^2, \quad \text{where } \Delta_{\infty} = \frac{\pi L \vartheta_{\text{max}}^2 n_o (n_e^2 - n_o^2)}{2\lambda n_e^2}, \quad (1.39)$$

determines the amplitude of retardation at large distance from the defect ($r \gg r_c$). The radial dependence of the retardation function is thus described by the square of universal function $a(r)$.

Expressions Eq. 1.32 and Eq. 1.39 are explicit profiles of azimuth and retardation of umbilic defect according to the Rapini model whose spatial distribution profiles in the transverse plane (x, y) are shown in Fig. 1.18(a) and Fig. 1.18(b) for $\phi_0 = 0$ and $\Delta_\infty = 2\pi$ (such a choice being clarified later). The latter brings an additional condition on the applied voltage, cell thickness and LC anisotropy characteristics, namely

$$\frac{L\vartheta_{\max}^2 n_o (n_e^2 - n_o^2)}{4\lambda n_e^2} = 1. \quad (1.40)$$

1.3.2 Umbilic as a natural modal q-plate candidate

Before to move to the quantitative analysis of umbilic modality, let us qualitatively compare it with the modal q-plate of the same charge and with $p = 0$, when $\Delta_\infty = 2\pi$. The retardation profile of Eq. 1.39 near to the umbilic core vanishes parabolically, indeed $a(r) \propto r$ for $r < r_c$ and $\Delta(r) \propto a(r)^2$, which is the case for the modal q-plate, as one can check by passing to the limit $r \rightarrow 0$ in Eq.1.16. On the other hand, far from the umbilic core, the retardation of umbilic converges rapidly to its maximal value of 2π , which is not a case for modal q-plate. This can be assessed in Fig. 1.17(d) comparing the green dashed curve with the blue curve, which refers to the modal q-plate profile $\Delta_{0,2}(r)$ given by Eq. 1.16 and the umbilic profile $\Delta(r)$ given by Eq. 1.39, respectively. However, such a difference can be almost removed if the decreasing part of modal q-plate retardation curve is mirror imaged with respect to the horizontal line defined by $\Delta_{0,2}(r) = \pi$, see Fig. 1.17(d) green solid line, which is expressed as

$$\Delta_{0,2}^{\text{new}}(r) = \begin{cases} \Delta_{0,2}(r), & \text{if } r < r_{\text{peak}}, \\ 2\pi - \Delta_{0,2}(r), & \text{if } r \geq r_{\text{peak}}, \end{cases} \quad (1.41)$$

where r_{peak} satisfies to the following condition $\Delta_{0,2}(r_{\text{peak}}) = \max_r [\Delta_{0,2}(r)] = \pi$. Let us note that in general the retardation curve of modal q-plate can have different forms depending on its characteristic waist radius W , but here we have chosen the one which gives largest correlation with umbilic retardation curve. The new retardation profile, compared with original one, will not change the complex amplitude shaping of transmitted light with opposite circular polarization than the incident one and similarly can be considered as a retardation profile of a modal q-plate. Indeed, $\Delta_{0,2}(r)$ in Eq. 1.11 is used inside the functions $\sin(\cdot)$ and $\exp(\cdot)$: the first one does not change the value after new reformulation, while the second one is canceled, if the azimuth profile of Eq. 1.17 be updated according to the

new retardation

$$\psi_{0,2}^{\text{new}}(r, \phi) = \frac{\sigma}{2} \left(\ell\phi - \frac{\Delta_{0,2}^{\text{new}}(r)}{2} \right), \quad (1.42)$$

The new director azimuth profile of modal q-plate is depicted in Fig. 1.18(c), which is different than the original one of Fig. 1.4 ($\ell = 2$, $p = 0$). The director azimuth profile of charge one umbilic corresponding to the Eq. 1.32 does not have the swirling behaviour of modal q-plate, see Fig. 1.18(a).

1.3.3 Quantitative modal analysis

For the quantitative analysis of umbilic modality we calculate the transmitted light field, $\mathbf{E}_{\text{out}}^{-\sigma}(r, \phi) = \mathbf{E}_{\text{out}}(r, \phi) \cdot \mathbf{e}_{-\sigma}$, just after the defect having an crossed-circular polarization state with incidence circular polarization state. Then we decompose it according to the Laguerre Gaussian modes, namely

$$\mathbf{E}_{\text{out}}^{-\sigma}(r, \phi) = \sum_{p,\ell} c_{p,\ell} u_{p,\ell}^{\text{LG}}(r, \phi), \quad (1.43)$$

where

$$c_{p,\ell} = \frac{\int \mathbf{E}_{\text{out}}^{-\sigma}(r, \phi) (u_{p,\ell}^{\text{LG}}(r, \phi))^* r d\phi dr}{\sqrt{\int |\mathbf{E}_{\text{out}}^{-\sigma}(r, \phi)|^2 r d\phi dr} \sqrt{\int |u_{p,\ell}^{\text{LG}}(r, \phi)|^2 r d\phi dr}} \quad (1.44)$$

is the complex projection coefficient of the output field on the LG field with (p, ℓ) modes. Accordingly, $|c_{0,2}|^2$ is the power fraction of the output field corresponding to the LG mode with $p = 0$ and $\ell = 2$. In general, the $|c_{0,2}|^2$ can get any values from 0 to 1. Larger it is, stronger is the modality of umbilic. Hereinafter we call it modality coefficient. Neglecting the light diffraction inside the umbilic defect, we apply the Eq. 1.11 for finding the output field just after the umbilic.

The analysis is summarized in Fig. 1.19. Fig. 1.19(a) shows the modality coefficient as a function of the incident Gaussian beam reduced waist radius, w_0/r_c . Fig. 1.19(b) corresponds to the dependence of the reduced waist of the best LG fit of the converted beam, w_{LG}/r_c , on the reduced waist of the incident Gaussian beam, w_0/r_c . Finally, Fig. 1.19(c) shows the efficiency of conversion. When the waist radius of incident beam vanishes, the conversion efficiency vanishes too, while the modality coefficient approaches to 1. In contrast, when the incident beam waist radius is much larger than the size of umbilic core, the modality coefficient approaches to some constant value smaller than 1. Hence, the umbilic defect can work as a modal beam shaper if the incident beam has much smaller waist radius than the size of umbilic core

$$w_0 \ll r_c. \quad (1.45)$$

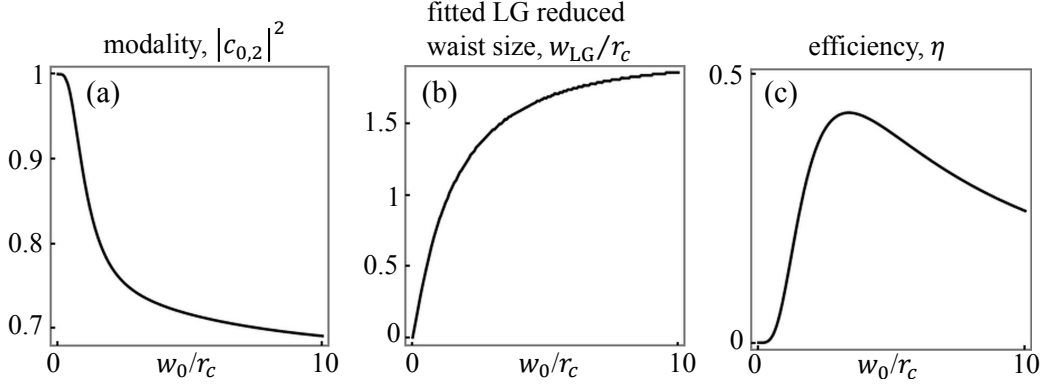


Figure 1.19: (a) Modality coefficient of output field for different waist radiuses of incident Gaussian beam. In general, modality coefficient shows the power fraction of output field corresponding to the LG beam of $\ell = 2$ and $p = 0$ modes and varies between 0 and 1. (b) Dependence of reduced waist radius of converted beam best LG fit, w_{LG}/r_c , on the reduced waist radius of incident Gaussian beam, w_0/r_c . When the waist radius of incident beam vanishes, the waist radius of best LG fit approaches to the incident waist radius, $w_{LG} \simeq w_0$ and the modality coefficient approaches to 1. (c) Conversion efficiency dependence on incident reduced waist radius. When the waist radius of incident beam vanishes, the conversion efficiency vanishes too, while the modality coefficient approaches to 1.

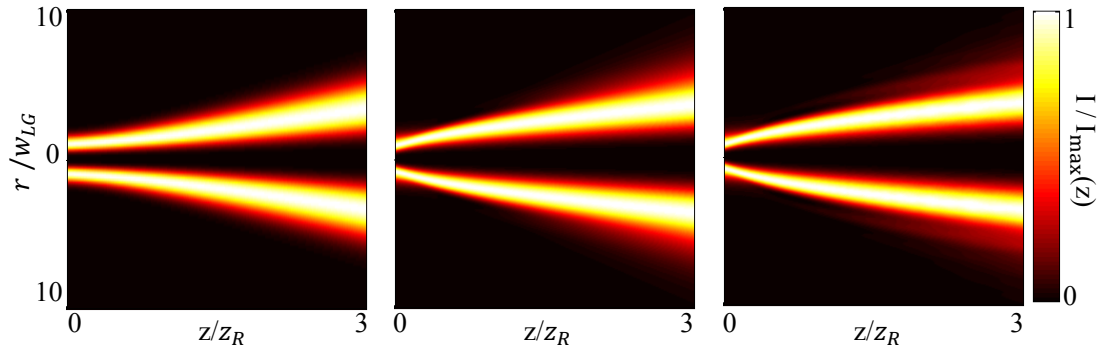


Figure 1.20: (a,b,c) Output beam diffractions from Rapini umbilic in free space for three typical cases of incident beam waist radiuses: $w_0 = 0.5r_c$ (a), $w_0 = 5r_c$ (b) and $w_0 = 10r_c$ (c), respectively. The radial axes of diffraction plots are normalized by their corresponding w_{LG} waist radiuses of best LG fits, taken from Fig. 1.19(b), $w_{LG} = 0.47r_c$, $w_{LG} = 1.54r_c$ and $w_{LG} = 1.64r_c$. The propagation z axes of plots are normalized by Rayleigh lengths of best fitted LG beam.

This makes sense with the Sec. 1.2 dealing with quasi-modal q-plate, since the incident Gaussian beam with small waist radius propagates through internal part of umbilic core, that has a small retardation (satisfies to the condition Eq. 1.24) with parabolic dependence on radius (satisfies to the condition Eq. 1.28 for $\ell = 2$ and $p = 0$). Interestingly, incident beam with small waist radius brings a modal conversion for any Δ_∞ value of umbilic, since the birefringent phase retardation near to the core satisfies to the Eqs. 1.24 and. 1.28 regardless of the value Δ_∞ . Let us also note, that far from the core of $\Delta_\infty = 2\pi$ umbilic, the retardation rapidly converges to 2π , so the transmitted light in opposite circular polarization than that for incident beam vanishes rapidly. Consequently, Gaussian incident beam of large waist radius, $w_0 \gg r_c$, changes only the conversion efficiency but not the beam shaping and its modality.

Summarizing, as the incident waist increases, the Rapini umbilic smoothly changes from a modal to a not modal. Such a transition is illustrated calculating the output beam diffraction in free space for three typical cases of incident beam waist radiuses and normalize them according to the w_{LG} waist radiuses of best LG fit, see Fig. 1.19. Figs. 1.20(a, b, c) correspond to the cases of $w_0 = 0.5r_c$, $w_0 = 5r_c$ and $w_0 = 10r_c$ normalized according to the $w_{LG} = 0.47r_c$, $w_{LG} = 1.54r_c$ and $w_{LG} = 1.64r_c$, respectively. In addition, the propagation are normalized by Rayleigh lengths of best fitted LG beam, $z_R = \pi w_{LG}^2/\lambda$. One can see that, Fig. 1.20(a) resembles to the diffraction of a LG beam (see Fig.1.8(f)), while a non modal behaviour can be grasped from Figs. 1.20(a,b) by mere comprehensive visual inspection.

1.3.4 Swirling route to modality

One more step towards the modality of umbilical defects can be done accounting for the imperfect realization of ideal umbilic as described by the Rapini model. Indeed, in practice, umbilics are neither ideally isolated nor evolving within ideally translation invariant cell. The result is that the relationship $\psi = \pm\phi + \phi_0$ is an idealization. In other words, real umbilics are swirled, though pursuing their topological charge ± 1 . For the sake of illustration, Fig. 1.21 shows a typical image of umbilic cell observed between crossed-linear polarizers and under the voltage $U = 2 V_{\text{rms}}$ modulated sinusoidally with 1kHz frequency. The sample is observed by microscope using incoherent white light source spectrally filtered at 633 nm wavelength.

Remarkably, the swirling properties of real umbilics remind us the swirling optical axis azimuth profiles of modal q-plates (see Fig. 1.4). From Sec. 1.1 we learnt that a retardation profile of the form, $\Delta(r)$, transfers to the incident field a space-variant anisotropic dynamic phase term $\exp(i\Delta_{p,\ell}(r)/2)$ in addition to the space-variant geometric phase term $\exp(2i\sigma\psi(r, \phi))$ arising from the azimuthal

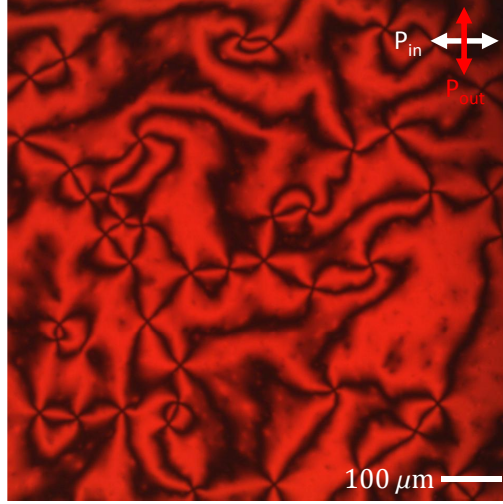


Figure 1.21: Typical image of umbilical sample between crossed linear polarizers illuminated by red incoherent light. Arrows correspond to the incident and output linear polarization states of light, P_{in} and P_{out} .

profile $\psi(r, \phi)$ of optical axis. An appropriately chosen radial dependence of the azimuth profile can thus lead to an overall space variant phase profile matching with the phase profile of given LG field with p and ℓ indices. Consequently, following the results of Sec. 1.1, the sought azimuth profile of a modal umbilic is

$$\psi^{\text{swirl}}(r, \phi) = \frac{\sigma}{2} \left(2\phi - \frac{\Delta(r)}{2} \right). \quad (1.46)$$

To our knowledge the Rapini approximation of umbilic retardation profile works good and it is experimentally reproducible [12, 101]. Hence, we keep the retardation profile of umbilic suggested from Rapini model, while its azimuth profile according to the Eq. 1.46 will get the new look depicted in Fig. 1.22(a). To find the desired umbilic experimentally, it is more convenient to know how it looks like in crossed circular and crossed linear polarizers. We choose the incident field a plane wave in order to have a similar case to the microscope observation, which uses generally a incoherent white light source. The calculation of the output field corresponding to the umbilic placed between crossed-circular polarizers is straightforward using Eq. 1.8, while the calculation of the output field corresponding to the umbilic placed between crossed-linear polarizers requires the initial representation of incident plane wave linear polarization on the basis of left/right circular polarizations, for example $\mathbf{e}_x = (\mathbf{e}_\sigma + \mathbf{e}_{-\sigma})/\sqrt{2}$, where the \mathbf{e}_x corresponds to the linear polarization of electromagnetic field along x direction. Afterwards, one can calculate the output field processing independently left and right circular polarization parts by Eq. 1.8 and combining them after. Finally, the crossed linear polarized part of output beam can be calculated by multiplying

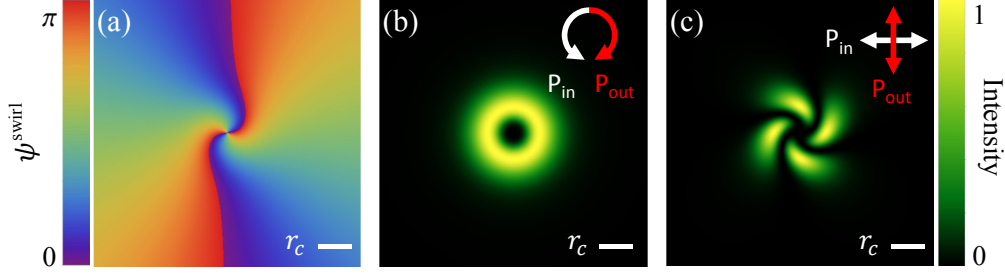


Figure 1.22: (a) Azimuth profile of a swirled umbilic, $\psi^{\text{swirl}}(r, \phi)$, obtained from Eq. 1.46 using Rapini retardation profile shown in Fig. 1.18(b) that provide with a modal q -plate with $p = 0$ and $\ell = 2$. (b,c) Simulated intensity pattern of a modal umbilic observed between crossed circular and crossed linear polarizers. White and red arrows indicate the incident and output selected polarization states, respectively.

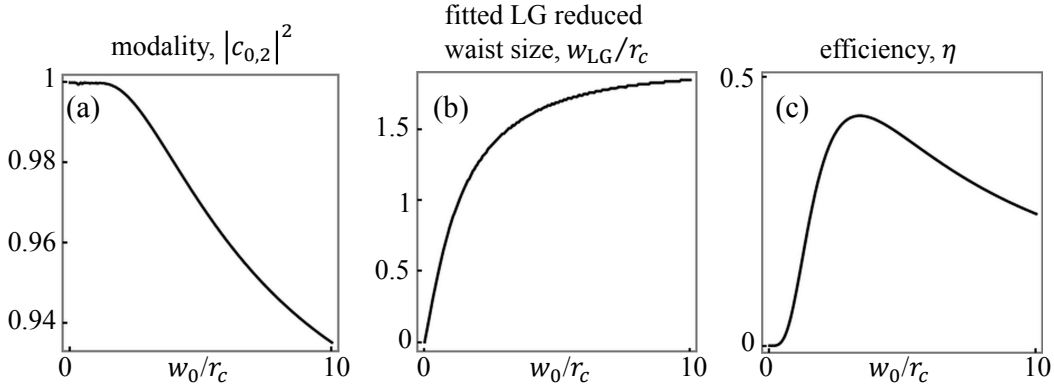


Figure 1.23: (a,b,c) The analogical dependencies of Figs. 1.19(a,b,c) corresponding to the new swirled umbilic.

it with the Jones matrix of crossed linear polarizer (see Eq. 1.47 and Eq. 1.48)

$$\mathbf{E}_{\text{in}} = E_0 e^{-i(\omega t - kz)} \mathbf{e}_x, \quad (1.47)$$

$$\mathbf{E}_{\text{out}} = -\sqrt{2} E_0 e^{-i\omega t} e^{ikLn_o} e^{i\frac{\Delta(r)}{2}} \sin \frac{\Delta(r)}{2} \sin(2\psi^{\text{swirl}}(r, \phi)) \mathbf{e}_y. \quad (1.48)$$

Figs. 1.22(b) and (c) correspond to the normalized intensity distributions of mentioned cases.

Similarly to the Fig. 1.19, the modality coefficient $|c_{0,2}|^2$, the corresponding waist radius of best LG fit w_{LG} , and efficiency coefficient η have been calculated as a function of the incident Gaussian beam reduced waist radius w_0/r_c , see three curves of Fig. 1.23. The converted beam diffraction for three typical cases of incident Gaussian beam waist radii have also been calculated, see Fig. 1.24.

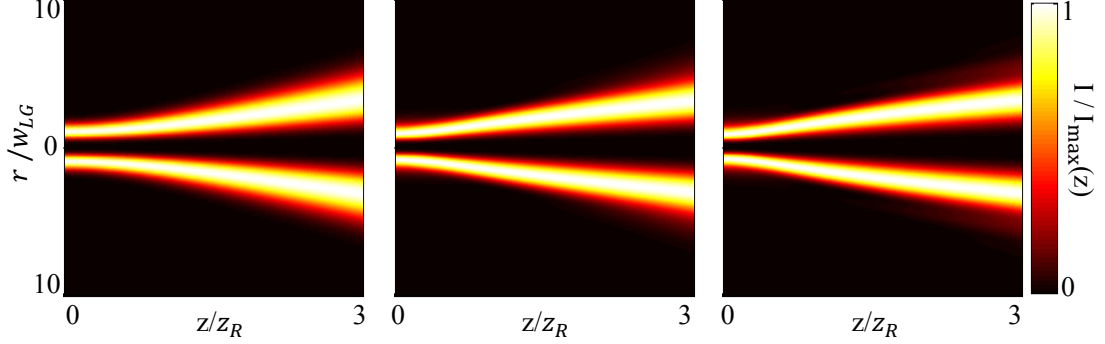


Figure 1.24: (a,b,c) The analogical diffraction plots of Figs. 1.20(a,b,c) corresponding to the new swirled umbilic.

Comparing the modality curves of Fig. 1.23(a) and Fig. 1.19(a) we conclude that a swirled umbilic can exhibit a very good modality, namely $|c_{0,2}|^2 > 0.99$ for $w_0/r_c < 5$, that is supported by the diffraction plots of Figs. 1.24(a, b).

1.3.5 Qualitative demonstration

A final step of our contribution is to carry out qualitative experimental observations of electrically induced modal umbilics in order to provide a first comparison with the theoretical results presented in previous sections. We use the nematic liquid crystal MLC-2079 with negative dielectric anisotropy, $\varepsilon_a^\Omega = \varepsilon_e^\Omega - \varepsilon_o^\Omega = -6.1$, $\varepsilon_e^\Omega = 4.1$, $\varepsilon_o^\Omega = 10.2$ at $\Omega = 1$ kHz, $K_1 = 15.9$ pN, $K_2 = 9.52$ pN, $K_3 = 18.9$ pN, and extraordinary and ordinary refractive indices are $n_e = 1.64$ and $n_o = 1.49$ at 589 nm wavelength. The 10 μm thick LC film is sandwiched between two glass substrates provided with transparent electrodes in the visible region and coated by homeotropic alignment layers to ensure the perpendicular orientations of LC molecules at boundaries (as sketched in Fig. 1.16). The Fréedericksz transition threshold value of applied voltage is $U_F = 1.83$ V_{rms}.

Two typical cases are analyzed. In the first case the, sample is under low electric field with $U_1 = 2$ V_{rms} (1kHz sinusoidal modulation), in second case it is under relatively higher electric field with $U_2 = 2.76$ V_{rms} (1kHz sinusoidal modulation). Accordingly, in the first case, $\Delta_\infty = \pi/2$ at 546 nm wavelength, while in the second case $\Delta_\infty = 2\pi$ at 633 nm wavelength.

The choice of $\Delta_\infty = \pi/2$ is done in order to use the Abrio imaging system, which can measure below π birefringent phase retardation at 546 nm operating wavelength. The idea is to find a umbilic that near to the core visually satisfies the requirement of quasi-modality, namely has a radially vanishing birefringent phase retardation with parabolic dependence on radius. Figs. 1.25(a) and (c) present the selected umbilic director azimuth and birefringent phase retardation

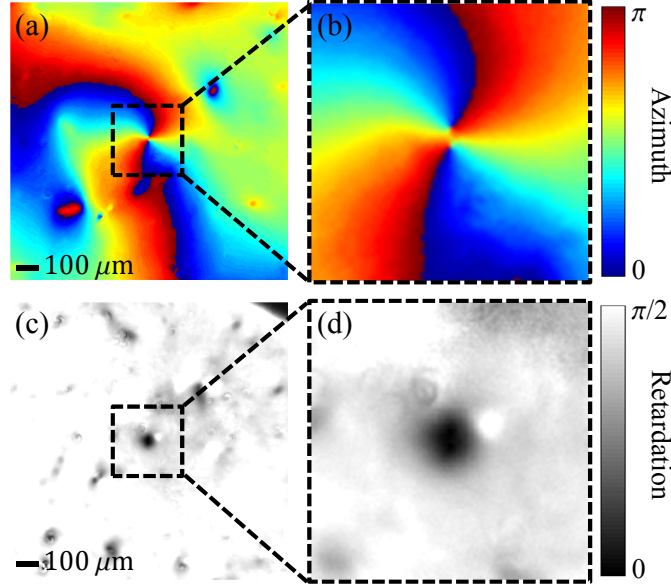


Figure 1.25: (a) The azimuth profile of umbilic induced in MLC2079 nematic homeotropic film under the voltage $U_1 = 2 \text{ V}_{\text{rms}}$. (c) Birefringent phase retardation profile of same umbilic of panel (a) at 546 nm wavelength. (b,d) enlargement of panels (a) and (c), respectively.

profiles over large area, whose local central regions enlarged in Figs. 1.25(b) and (d) exhibit qualitative similarities with Fig. 1.22(a) and Fig. 1.18(b). We stress that the umbilic compared with the fabricated quasi-modal q-plate with the same charge (see Fig. 1.10(b)) qualitatively exhibits much better retardation profile near to the core. Consequently, we expect that such umbilic will exhibit quasi-modal features if the incident Gaussian beam has relatively smaller waist radius than the core radius of umbilic (see Fig. 1.19(a)).

In second case, the choice of $\Delta_\infty = 2\pi$ at 633 nm wavelength is done in order to have the same asymptotic retardation value of theoretically predicted modal umbilic and observe the liquid crystal sample by microscope between crossed-circular and crossed-linear polarizers using incoherent white light source spectrally filtered at 633 nm wavelength. The idea is to select one that visually matches with the theoretical simulations of modal umbilic between crossed-circular and crossed-linear polarizers, see Fig. 1.22. Figs. 1.26(a,b) show the selected umbilic between crossed circular and crossed linear polarizers, respectively. Note, that following the theoretical discussion of Sec. 1.3.4, the umbilic placed between crossed-circular polarizers gives the information about its retardation profile, while the umbilic placed between crossed-linear polarizers gives information about both its retardation and azimuth profiles (see Fig. 1.48). Indeed, the first image presents an isolated vortex as in theoretical simulation of Fig. 1.22(b), which is an indication of umbilic $\Delta_\infty = 2\pi$ asymptotic retardation. However, the second image

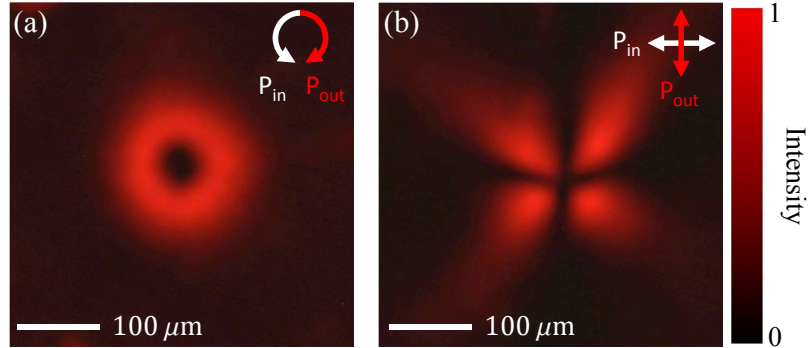


Figure 1.26: (a,b) Images of umbilical defect between crossed circular (a) and crossed linear (b) polarizers, respectively. The umbilic is induced in MLC2079 nematic homeotropic film under the voltage $U_2 = 2.76 \text{ V}_{\text{rms}}$. White and red arrows indicate the incident and output light polarization states, respectively.

clearly shows that the umbilic –being under higher voltage than that in the first case– does not possess the needed swirling properties of azimuth, that would lead to more swirled image as in Fig. 1.22(c). Nevertheless, the important conclusion of this section is that we performed the first experimental qualitative exploration and we believe that our preliminary results will soon be completed with the clean demonstration of the predicted modal umbilic. Importantly, many kinds of methods discussed in Sec. 1.3.1 give rise to very different umbilical defects, which offers a large set of options for optimization.

In addition, other self-engineered strategies that do not rely on machining techniques can also be considered. Various kinds of spontaneously formed liquid crystal defect structures with spatially varying birefringent phase retardation and azimuth profiles are enabling the generation of optical vortex beams with satisfying first-order key requirement feature of modality, namely, at the center they possess zero birefringent phase retardation. One can mention hedgehog defects [88], focal conic domains in smectics [102], localize solitonic defect structures in cholesterics [103], stress-induced birefringent defects in solid wave plates [104] and thermal-induced birefringent defects in terbium-gallium-garnet crystal [105, 106].

Reflective broadband spin-orbit beam shaping from chiral anisotropic optical media

2.1 Cholesteric liquid crystals: optical characterization

In this chapter we propose original highly reflective optical elements enabling the topological shaping of an incident light beam via geometric phase. Our idea relies on the use of cholesteric (or chiral nematic) liquid crystals (CLCs) [107]. In practice, it is well known that CLCs are prime choice materials to realize so called chiral Bragg mirrors. CLCs combine intrinsic periodic modulated orientation of molecules characterized by the local nematic extraordinary and ordinary refractive indices n_e and n_o , with chiral supramolecular ordering characterized by the pitch p over which the director, \mathbf{n} , rotates by 2π . The helicoidal director ordering of a CLC layer laying between planes $(x, y, z = 0)$ and $(x, y, z = L)$ is

$$\mathbf{n} = \left(\cos\left(\frac{2\pi\chi}{p}z + \phi_0\right), \sin\left(\frac{2\pi\chi}{p}z + \phi_0\right), 0 \right), \quad (2.1)$$

where ϕ_0 is a constant depending on boundary conditions and $\chi = \pm 1$ refers to the right/left handedness of the supramolecular chirality. Hereafter, we will call such CLCs with helix axes perpendicular to their boundaries as planar homogeneous CLCs.

The diffraction of normal incident electromagnetic field on the periodic chiral and anisotropic structure of planar homogeneous CLCs leads to circular Bragg reflection phenomenon in the range of wavelengths called photonic bandgap, $n_o p < \lambda < n_e p$ [77, 108]. Bragg reflected field can carry almost 100% of incident light power if the electric and magnetic vectors of incident circularly polarized light in free space at a particular time describe a helix along propagation direction, whose handedness is identical to the handedness of the chiral medium, see Fig. 2.1. Hence, hereafter we call such circular polarization as a co-handed circular polarization while the orthogonal one as a cross-handed cir-

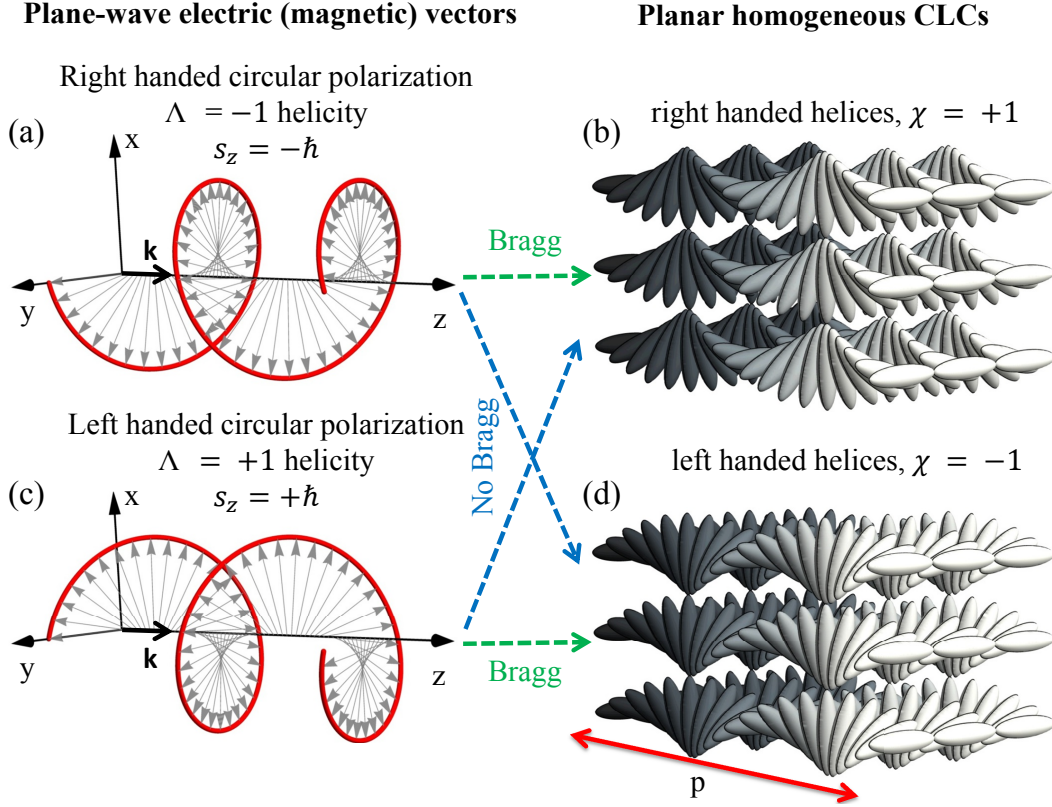


Figure 2.1: (a,c) Right and left handed circularly polarized plane waves electric (magnetic) vectors in free space at a particular time. (b,d) Planar homogeneous CLCs with right and left handed supramolecular chiralities. $\Lambda = \pm 1$ is the projection of spin angular momentum of the photon on propagation direction z in units \hbar . $\chi = \pm 1$ refers to the right/left handedness of CLCs helix.

circular polarization [109]. Let us emphasize that the electric (or magnetic) vector described by left/right handed helix, circulates at given position counterclockwise/clockwise for the observer looking toward an oncoming electromagnetic field as time increases. Therefore, electric (or magnetic) vector described by left/right handed helix equivalently corresponds to the left/right handed circular polarization (LHCP/RHCP) as it is presented in Fig. 2.1(a,b). Correspondingly, the CLC with right (or left) handedness of supramolecular chirality Bragg-reflects RHCP (LHCP) polarized state of incident light. On the other hand co-handed circularly polarized wave satisfies to the condition $\Lambda\chi = -1$, where $\Lambda = \pm 1$ is the helicity of photon.

The important feature of circular Bragg reflection illustrated in Fig. 2.2(a) is that co-handed circularly polarized light Bragg-reflecting from the CLC mirror preserves its polarization handedness and helicity. This implies that Bragg-reflected photons preserve their helicity, while their spin angular momentum projection on the axis z reverses its sign. Indeed, the reflecting photon changes

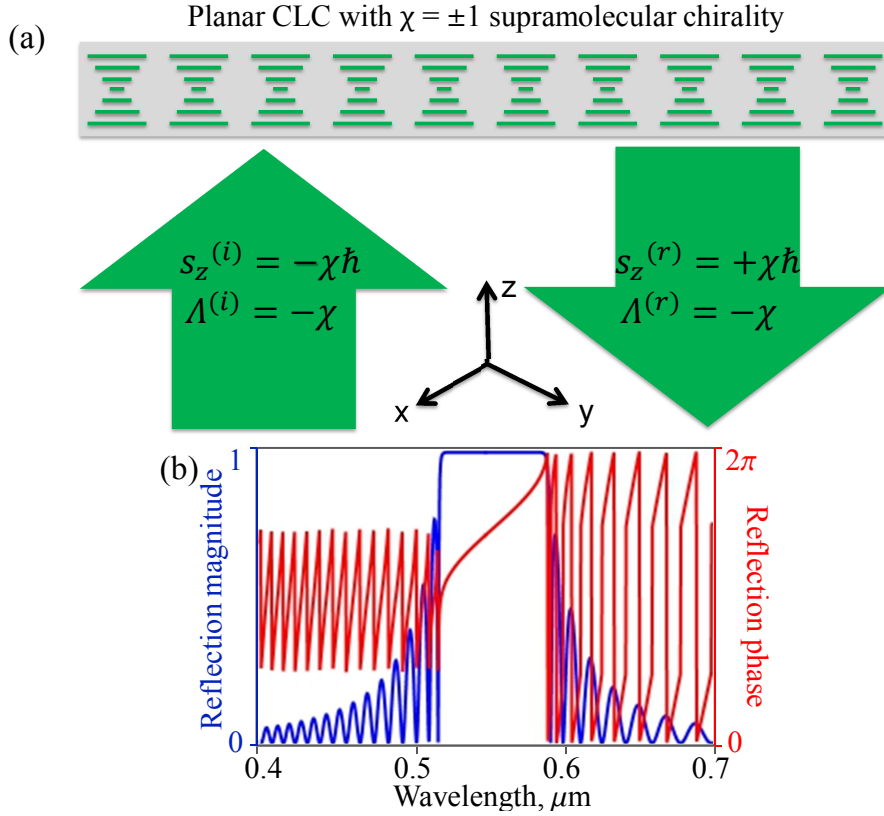


Figure 2.2: (a) Circular Bragg reflection phenomenon from supramolecular helical ordering of the planar homogeneous CLC mirror. (b) Reflection magnitude and phase spectral dependencies on incidence wavelength calculated by Berreman 4×4 matrix formalism. Medium parameters are: $\chi = +1$, $n_e = 1.7$, $n_o = 1.5$, $p = 0.347 \mu\text{m}$, $d = 20p$, $h = p/100$

its propagation from positive to negative direction of z axis.

Although the planar homogeneous CLC supramolecular ordering presented in Fig. 2.1(b,d) describes the simplest director distribution for a CLC slab (see Eq. 2.1), only normal incident plane wave finds an analytical solution of its reflection and transmission fields according to the Berreman method [108]. In order to deal with the case of oblique incidence, an approximate analytical approach called coupled-mode theory has been developed, which has the merit to have a not too heavy mathematical formulation [110, 111]. When exact solution is sought, one has to consider a numerical approach, such as the Berreman 4×4 matrix formalism [112], Ambartsumian’s layer addition modified method [113] or finite-difference time-domain method (FDTD) [114].

In our further theoretical calculations without loss of generality we will consider the Berreman 4×4 matrix formalism in the framework of the optimized approach development by I. Abdulhalim [115]. Accordingly, CLC is considered

as a multilayered system, where each layer is perpendicular to the helix axis and its local director orientation can be assumed to be constant. It is also assumed that the medium is lossless. Each elementary layer of thickness δL being constituted of an homogeneous uniaxial anisotropic dielectric medium, can be associated with an analytical propagation matrix P_i according to the Maxwell's equations, where i is the number of the layer varying from 1 to $N = L/\delta L$. By multiplying the elementary transfer matrices one finds the total transfer matrix of the multilayered CLC: $P = P_N P_{N-1} \dots P_{i+1} P_i P_{i-1} \dots P_1$. Eventually, having the propagation matrix of total CLC medium, one can easily deduce the corresponding reflection, refraction and transmission fields. For instance, the spectral dependencies on the incidence wavelength of reflection magnitude, normalized in $(0,1)$, and the reflection phase, normalized in $(0,2\pi)$, can be calculated, as illustrated in Fig. 2.2(b). The medium parameters are taken as $\chi = +1$, $n_e = 1.7$, $n_o = 1.5$, $p = 0.347 \mu\text{m}$, $d = 20p$, $\delta L = p/100$.

In this chapter we report on highly reflective spin-orbit optical elements based on helicity-preserving circular Bragg reflection phenomenon. Sec. 2.2 unveils the existence of geometric phase in reflected light field by dynamic geometric phase experiment using a flat planar homogeneous CLC. Such geometric phase allows efficient spin-orbit tailoring of light fields without need to fulfill any condition for the birefringent phase retardation, in contrast to the case of transmissive spin-orbit optical elements (see Sec. 1.1.2 for conventional q-plates). Sec. 2.3 reports on the experimental realization of flat Bragg-Berry mirrors enabling the broadband generation of optical vortices upon reflection. It demonstrates the reflective optical vortex generation from both diffractive and nondiffractive paraxial light beams using spatially inhomogeneous planar CLC films endowed with topological structure with charge 1. Sec. 2.4 reports on polychromatic dynamic geometric phase experiment using a flat chiral Bragg mirror having spatially varying pitch (so-called gradient-pitch CLCs). Ensuing experimental realization of ultra-broadband reflective optical vortex generation from gradient-pitch inhomogeneous planar CLC is presented. Sec. 2.5 reports on the experimental realization of reflective broadband Bragg-Berry q-plates based on mirror-backed charge one inhomogeneous planar CLC film. The vortex generation from left/right circularly polarized incident beams as well as the vector field generation from linearly polarized incident beam are presented. Finally, Sec. 2.6 investigates both experimentally and theoretically the spatio-temporally modulated vector fields induced from the periodical mechanical oscillation of usual back-mirror along positive and negative directions of BB mirror.

2.2 Dynamic geometric phase experiment

In this section we report on the demonstration of a dynamic geometric phase experiment proving the existence of a geometric phase for the reflected light from flat chiral Bragg mirror. The idea is to set a planar homogeneous CLC film into rotation around its normal at the angular frequency $\Omega = \Omega \mathbf{z}$ (with \mathbf{z} unit vector along the z axis) and illuminate it by a laser beam at wavelength $\lambda_0 = 532$ nm that falls into the Bragg-reflection spectral range under the condition $\Lambda\chi = -1$, see Fig. 2.3(a).

2.2.1 General consideration

In practice, the mirror is made of a right-handed ($\chi = +1$) CLC film of thickness $L = 5 \mu\text{m}$ and pitch $p = 347$ nm (MDA-02-3211 mixture from Merck: refractive indices are $n_e = 1.7013$ and $n_o = 1.5064$ at 589.3 nm wavelength and temperature 20°C). The planar and homogeneous director distribution along the cell is presented in Fig. 2.3(b). As a result of the sample rotation, the CLC helices rotate around the z axis at angular frequency Ω , as sketched in Fig. 2.3(c). Below, the experiment is described from three different points of view: (i) reflected field phase calculation by Berreman 4×4 matrix formalism for azimuthal varying CLC helices from 0 to 2π , (ii) exerted total optical torque and its consequence on the phase of reflected light (iii) the Coriolis effect on reflected light regarding to its intrinsic spin angular momentum and its interaction with rotating CLC.

(i) The rotation of planar homogenous CLC around its helix axis implies that at given time the CLC can be described in the (x,y,z) laboratory frame by Eq. 2.1, where the angle ϕ_0 periodically varies from 0 to 2π , while other parameters such as the chirality χ and the pitch p are fixed. By doing so and considering an incident plane wave at $0.532 \mu\text{m}$ wavelength on CLC with $\chi = +1$ chirality, the phase of reflected field calculated by Berreman 4×4 matrix formalism exhibits varying linear behaviour with negative gradient, see Fig. 2.4, while the magnitude of reflected field stays equal to one. Note, that the same calculation for $\chi = -1$ results to the same magnitude of reflected field, while the phase exhibits linear behaviour with positive gradient. Consequently, the rotation of planar homogenous CLC results to the periodical increase or decrease of phase (so-called geometric phase) of reflected field depending on the chirality of CLC.

(ii) When light interacts with birefringent matter, it may change its angular momentum content, hence exerting an optical radiation torque on it (for example, see [116]). In our case, light changes the sign of its spin angular momentum projection along the z axis, $s_z^{(r)} = -s_z^{(i)}$ (see Fig. 2.2). Consequently, angular momentum conservation of the light-matter system implies that an optical radiation

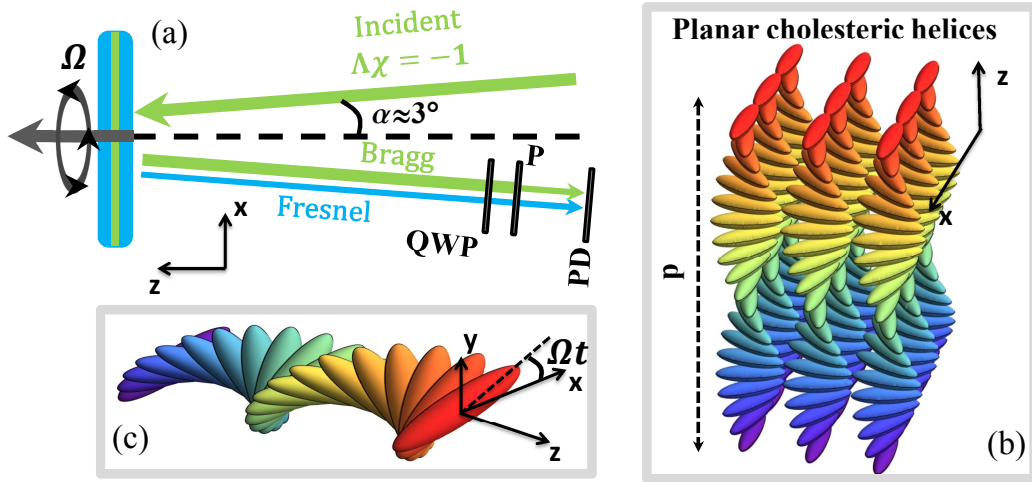


Figure 2.3: (a) Dynamic geometric phase experiment setup. QWP: quarter-wave plate, P: polarizer, PD: photodetector. Thin ‘Fresnel’ arrow refers to incident light reflected at air/glass interfaces and thick arrow labeled ‘Bragg’ refers to circular Bragg reflection. Sample is rotated at angular frequency $\Omega = 20^\circ/\text{s}$. (b) Illustration of the planar reorientation of homogeneous CLC helices. (c) Illustration of the rotation of the supramolecular helix at angular frequency Ω .

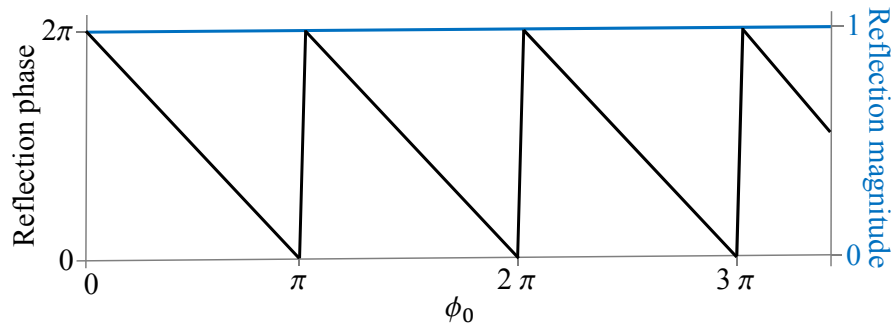


Figure 2.4: Reflection magnitude and phase dependencies on azimuthal angle of CLC helices, ϕ_0 , calculated by Berreman 4×4 matrix formalism at Bragg wavelength for the following parameters of CLC: $n_o = 1.5$, $n_e = 1.7$, $p = 347 \text{ nm}$, $L = 5 \text{ }\mu\text{m}$, $\chi = 1$.

torque is exerted by light on the CLC. Namely, the exerted torque per photon in unit time is $\Gamma_z = s_z^{(i)} - s_z^{(r)} = -2\chi\hbar$. When the CLC rotates around the axes z at frequency Ω , a work is made by light on matter, and reciprocally. Consequently, energy is either gained or dissipated, which is associated with a frequency shift $\delta\omega$. The latter shift, which is a rotational Doppler frequency shift, can be derived following energy conservation principle for the “light+matter” system considered as isolated, namely $\hbar\delta\omega - 2\chi\hbar\Omega = 0$

$$\delta\omega = 2\chi\Omega. \quad (2.2)$$

Accordingly, the following transformation takes place for time-dependent phase factor of the field: $\exp(-i\omega t) \rightarrow \exp(-i(\omega + \delta\omega)t) = \exp(-i\omega t) \exp(i\Phi)$, where $\Phi = -\delta\omega t = -2\chi\Omega t$ is the geometric phase acquired in reflection field. The Ωt production is equivalent to the $\phi_0 = \Omega t$ rotation of CLC helix (see Fig. 2.3(c)), consequently the geometric phase can be represented in the following form

$$\Phi = -2\chi\phi_0. \quad (2.3)$$

One can see that Eq. 2.3 agrees with the numerical calculations of Fig. 2.4.

(iii) Another explanation of mentioned frequency shift can be achieved within the framework of the Coriolis effect on the reflected light regarding to its interaction with the rotating CLC, following the work by K.Y. Bliokh [117]. Accordingly, in the rotating coordinate system “attached” to the director field, the reflected light undergoes frequency shift according to $\int \delta\omega dt = -\int \mathbf{s} \cdot \boldsymbol{\Omega} dt$, where \mathbf{s} is the spin angular momentum (per photon, in \hbar units) aligned along the beam propagation direction axis, and t is the time. Since the Bragg field satisfies $\mathbf{s}^{(i)} \cdot \boldsymbol{\Omega} = -\chi\Omega$ and $\mathbf{s}^{(r)} \cdot \boldsymbol{\Omega} = \chi\Omega$ the Bragg reflected wave experiences an angular frequency shift $\delta\omega = 2\chi\Omega$ and, consequently, acquires a geometric phase $\Phi = -2\chi\phi_0$.

2.2.2 Experiment

Experimentally, the above prediction of a dynamic geometric phase shift and associated frequency shift is verified by recording the net optical power of the Bragg-reflected wave combined with the unavoidable contribution of Fresnel reflection at air/glass interfaces of the cell. Indeed, the Bragg part of the reflected light is expected to acquire a frequency shift $2\chi\Omega$, while the Fresnel one is not frequency shifted since reflection off a glass surface do not flip the photon spin angular momentum, as is the case for a standard mirror. In turn, temporal intensity beatings arising from the superposition of these two contributions to the reflected light are expected.

Importantly, Bragg and Fresnel contributions have orthogonal polarization states and different powers. The glass substrates are not anti-reflection coated, hence the intensity of the Fresnel contribution is a few percent of that of the

Bragg contribution. Therefore, we use a quarter-wave plate (QWP) and a linear polarizer (P), which gives us full freedom to extract from the total field either only Bragg contribution, only Fresnel contribution or any superposition for the Bragg and Fresnel contributions. In our experiment we are interested in three basic cases:

- case 1: only the Bragg contribution is extracted from the total reflected field,
- case 2: only the Fresnel contribution is extracted from the total reflected field,
- case 3: equivalent Bragg and Fresnel contributions are extracted from the total reflected field.

The relative orientations of QWP and P corresponding to mentioned cases 1, 2 and 3 are found experimentally. Our protocol consists to install a standard mirror at the place of CLC in order to find the relative orientation of QWP and P which blocks the total reflected field, let us call a state 1 the mentioned relative orientation of QWP and P. Placing back the CLC, in state 1 the QWP and P select only the Bragg contribution from total reflected field. Indeed, blocking the Fresnel-reflected field from mirror it blocks the Fresnel-reflected field from the CLC/glass interference. Changing by the relative orientation between QWP and P from state 1 by 90 degrees we access to the state 2, which blocks the Bragg contribution while transmitting totally the Fresnel contribution. Finally, the state 3 of QWP and P, that ensures equal powers for the Bragg and Fresnel contributions is defined by the optimum contrast of the interference pattern impinging on the photodetector, see Fig. 2.3(a).

As shown by the red curve of Fig. 2.5(a), the detected signal is periodic and its power Fourier spectrum reveals a peak at frequency 2Ω , see Fig. 2.5(b). Practically, we used slightly oblique incidence ($\alpha \simeq 3^\circ$) that allows direct comparison with above general consideration of the dynamic geometric phase effect since this allows to select the total reflected field. Importantly, Bragg and Fresnel contribution – extracted separately by state 1 and state 2 relative orientations of QWP and P – give a much weaker periodic signal (see green and blue dotted curves of Fig. 2.5(a)). Corresponding Fourier spectra at 2Ω frequency are in the level of noise compared with the amplitude of main peak, see enlarged region at the foot of main peak in Fig. 2.5(b). However, residual dynamics probably appear due to the experimental imperfections of the CLC ordering, non ideal assembling of substrates and optical adjustments.

Importantly, Bragg-Berry chiral optical elements represent a novel class of spin-orbit components that do not require to fulfill the half-wave retardation

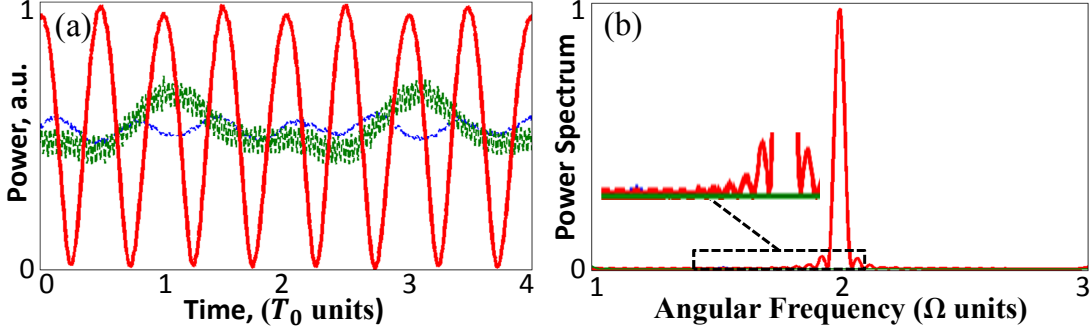


Figure 2.5: (a) Periodic signals acquired by the photodetector PD shown in Fig 2.3(a) over $\simeq 40$ periods for three configurations of the analysis of the reflected light (see state 1, state 2 and state 3 in the text), which is generated by the relative angle between QWP and P: only Bragg signal (green dotted line), only Fresnel signal (blue dotted line), equivalent Bragg-Fresnel signals for strong interference (red line) (b) Power Fourier spectrum of the three periodic signals of (a). Power Fourier spectra of Bragg and Fresnel signals are in the level of noise at the foot of main peak.

condition for optimal vortex generation, in contrast to transmissive spin-orbit couplers based on space-variant anisotropic slabs [8, 118].

2.2.3 Towards chiral Bragg metasurfaces

Although the Secs. 2.2.1 and 2.2.2 are restricted to supra-wavelength-thick chiral samples (which ensures almost 100% reflectivity), we stress that the proposed phase shaping approach is valid for smaller thickness-to-wavelength ratio too, however at the expense of reflectivity or strong material anisotropy.

To illustrate these points, let us first consider a single-pitch-thick slab ($L = p$) of the used material with $p \sim 347$ nm. The reflected phase and magnitude spectra as well as the geometric phase dependence on the azimuthal angle ϕ_0 of CLC helices are calculated by Berreman 4×4 matrix formalism and presented in Figs. 2.6(a,b). Fig. 2.6(a) shows that the single-pitch-thick slab provides higher than 10% reflectivity in a wide spectral range and can be qualified as a (non-negligibly) reflective dielectric metasurface, since $L < \lambda$. On the other hand, Fig. 2.6(b) confirms the preserved existence of geometric phase even if the CLC has a subwavelength thickness.

Importantly, we note that the reflectivity limitations can be waived with appropriate choice of material parameters recalling that the circular Bragg photonic bandgap is basically defined as $n_o p < \lambda < n_e p$. Namely, one can thus envision chiral metasurfaces fabricated from high refractive index metamaterials and small enough pitch with respect to wavelength. As a example, let us consider a chiral

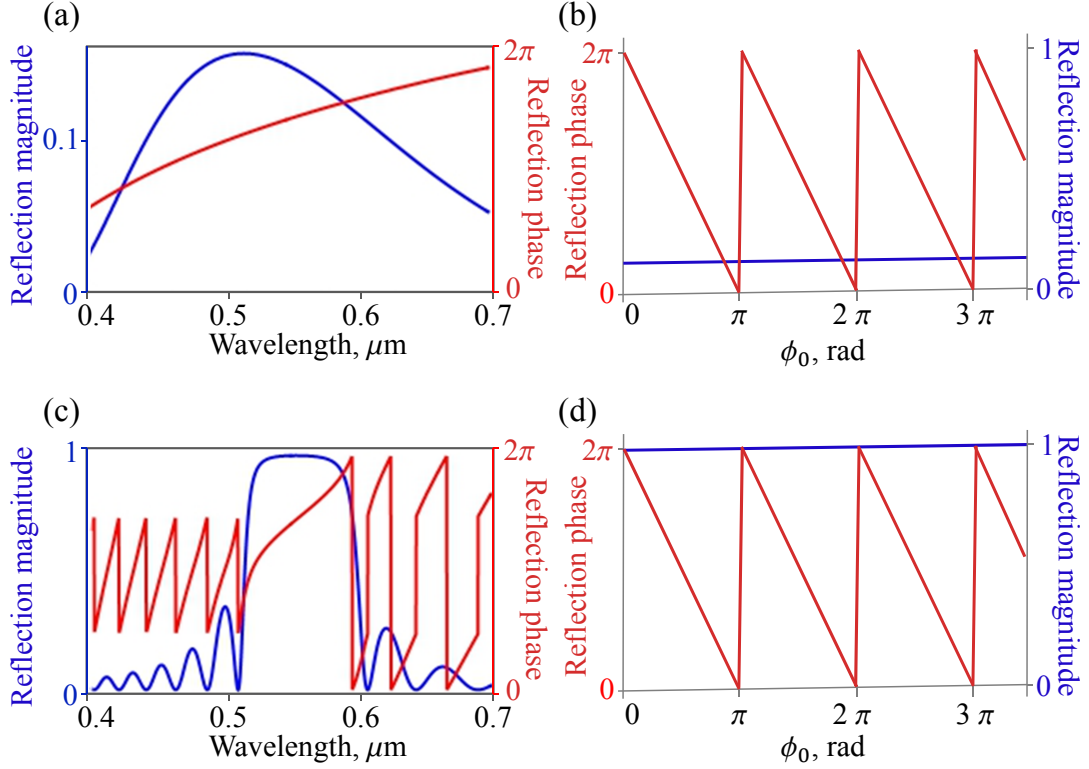


Figure 2.6: Reflection magnitude and phase dependencies on the incident wavelength and azimuthal angle of CLC helix, ϕ_0 , calculated by Berreman 4×4 matrix formalism for the following parameters: (a) and (b) $n_o = 1.5$, $n_e = 1.7$, $p = 347$ nm, $L = p = 347$ nm, $\chi = 1$. (c) and (d) $n_o = 6 \cdot 1.5$, $n_e = 6 \cdot 1.7$, $p = 347/6$ nm, $L = 8p = 463$ nm, $\chi = 1$.

metamaterial of six times larger refractive indices, $n_o = 6 \cdot 1.5$ and $n_e = 6 \cdot 1.7$, while the pitch of chiral metamaterial we choose six times smaller, $p = 347/6$ nm, in order to keep the photonic bandgap in the same spectral region. The thickness of metamaterial we take for simulation as a $L = 8p \simeq 463$ nm, which remains subwavelength for the photonic bandgap of that material. The results are shown in Figs. 2.6(c,d) that present the reflectivity and the phase similarly to the Figs. 2.6(a,b). It is found that the reflectance inside the photonic bandgap reaches almost 100%, while the geometric phase is unchanged. This illustrates that the realization of subwavelength highly reflective geometric phase device is possible. However, such chiral metamaterials bring challenging technological requirements, especially when considering operating wavelengths in the visible domain [119–121].

2.3 Bragg-Berry mirrors

2.3.1 Position of the concept

The geometric Berry phase associated with the circular Bragg reflection phenomenon in chiral anisotropic optical media brings a novel paradigm to achieve wavelength-independent pure spin-orbit topological shaping of light from “Bragg-Berry” mirrors, whose unique specificities are the ability to work (i) in the reflection mode, (ii) without need of any birefringent retardation requirement.

Here we propose, realize and experimentally demonstrate the broadband reflective optical vortex generation from flat Bragg-Berry mirrors for both diffractive and nondiffractive paraxial light beams. This is done by using either Gaussian or Bessel incident beams whose reflection off a chiral Bragg mirror endowed with suitable surface orientational boundary conditions lead to the production of Laguerre-Gauss and higher-order Bessel like beams, respectively. From the spectral point of view, we report on optical vortex generation over the full visible range, at least from 450 nm to 650 nm wavelengths. By doing so, our results set the basis for the development of a novel generation of spin-orbit optical elements whose demonstrated robustness against polychromaticity and fabrication constraints offer a valuable alternative to existing q -plates limitations, as presented in Sec. 1.1.2.

As shown in the previous section, it is the preservation of the photon helicity at circular Bragg reflection, associated with the azimuthal orientation of chiral helix, that leads to the production of a geometric Berry phase for the reflected light. More precisely, we have established that a CLC Bragg mirror characterized by director orientation angle ψ at its input facet generates a phase factor $-2\chi\psi$ for the Bragg-reflected field. Thus, we expect that a Bragg-Berry mirror having a surface director orientation of the form $\psi = q\phi$, q being a half-integer, leads to a change of the incident orbital state ℓ by an amount $\Delta\ell = -2\chi q$. Hereafter we will call such inhomogeneous planar Bragg-Berry mirror as a “charge q BB mirror”.

2.3.2 Experimental approach

Flat Bragg-Berry mirrors are prepared from a 10 μm -thick right-handed CLC film, similar to that used in Sec. 2.2. The CLC slab is sandwiched between two glass substrates coated by an azobenzene-based surface-alignment layer with submicron thickness fabricated by Beam Co., as depicted in Fig. 2.7(a). The two alignment layers are optically treated to ensure azimuthally varying orientation of the liquid crystal helices at both ends of the liquid crystal layer of the form $\psi = q\phi$ with q half-integer (homogeneous planar alignment layers used in previous section thus refer to $q = 0$). What follows, without loss of generality, we restrict

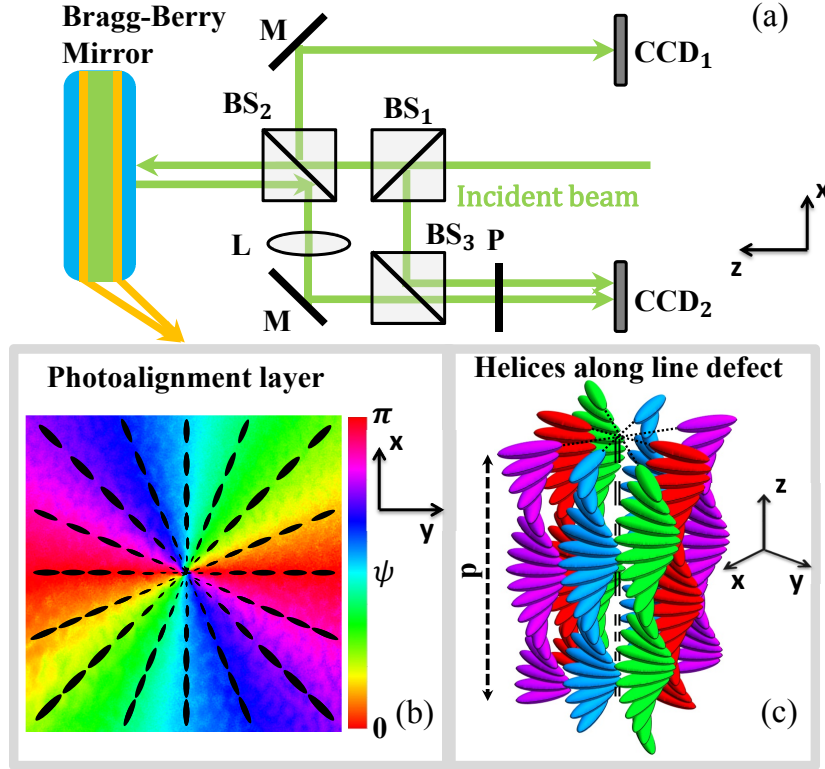


Figure 2.7: (a) Experimental setup for optical vortex generation from a normal incident beam on Bragg-Berry mirror. M , mirror; $BS_{1,2,3}$, beam splitters; L , lens; P , polarizer; $CCD_{1,2}$, imaging devices. (b) Experimental map of the space-variant orientation ψ of the photoalignment layers in the (x, y) plane. (c) Illustration of the charge one inhomogeneous planar CLC helices and their azimuthal reorientation around the hypothetical line defect (illustrations of helices are restricted to the one pitch, p).

our demonstration of principle to the case $q = 1$. This is illustrated in Fig. 2.7(b) that shows the spatial distribution of the orientational boundary conditions of a coated glass substrate alone obtained by Abrio imaging system. The residual birefringent phase retardation of the the alignment layer is measured to be of the order of 0.01π . Its contribution to the reflected field is therefore weak enough to be safely discarded. We assume that the director profile in each transverse plane of the charge one BB mirror corresponds to the profile of the charge one photoalignment layer but rotated by azimuthal angle $2\pi\chi z/p$. Consequently, the cholesteric helices of BB mirror oriented according to the photoalignment layers make an hypothetical line defect, as sketched in Fig. 2.7(c).

2.3.3 Demonstration

Experimental demonstration of optical vortex generation is done at 532 nm wavelength (that falls in photonic bandgap of our material) by using a continuous laser beam, following the setup shown in Fig. 2.7(a). At first, the charge one BB mirror is illuminated at normal incidence by a co-handed circularly polarized Gaussian beam with beam waist radius in the plane of the mirror $w \sim 0.25$ mm, see Fig. 2.8(a). The far-field reflected light is then collected by the camera CCD₂ by placing the lens L in f - f configuration with respect the charge one BB mirror and the camera, see Fig. 2.8(b). Indeed, this ensures optical Fourier transform of the field on the plane of the sample. A doughnut intensity profile, which is characteristic of the expected on-axis optical phase singularity of topological charge -2χ is observed. Theoretically, this is described by Fourier transform, which expresses in the polar coordinate (k, θ) in the reciprocal space as

$$E(k, \theta) \propto \int_0^{2\pi} \int_0^\infty \Phi(\phi) G(r) \exp[-ikr \cos(\theta - \phi)] r dr d\phi, \quad (2.4)$$

where $G(r) = \exp(-r^2/w^2)$ is the Gaussian beam incident amplitude on the mirror and $\Phi(\phi) = \exp(-2i\chi\phi)$ is the reflective phase mask of the Bragg-Berry mirror. Integration over the azimuthal coordinate gives

$$E(k, \theta) \propto \exp(-2i\chi\theta) \int_0^\infty G(r) J_{-2\chi}(kr) r dr, \quad (2.5)$$

where J_n is the n th-order Bessel function of the first kind, which unveils the optical phase singularity with topological charge 2χ . The corresponding intensity profile is axisymmetric and is given by

$$I(k) \propto [1 - \exp(-k^2 w^2/4)(1 + k^2 w^2/4)]/k^2. \quad (2.6)$$

The result of simulation is shown in Fig. 2.8(c) that displays both the intensity (luminance) and phase (colormap) profiles. The phase profile is defined for $\chi = -1$.

Further demonstration of singular beam shaping dictated by $\Delta\ell = 2\chi q$ change of the incident orbital state is made by analyzing the phase profile of the field just after its reflection from the sample. This is shown in Fig. 2.9(a) that displays the intensity pattern collected by CCD₂ camera using a lens L in $2f$ - $2f$ configuration with respect to the sample and the camera. Obviously, the observed intensity pattern corresponds to a Gaussian envelope since diffraction has not yet taken place. However, the optical phase singularity is already imprinted into the field, which is revealed by interfering the reflected field with a reference Gaussian beam. The resulting interference pattern is shown in Fig. 2.9(b) that

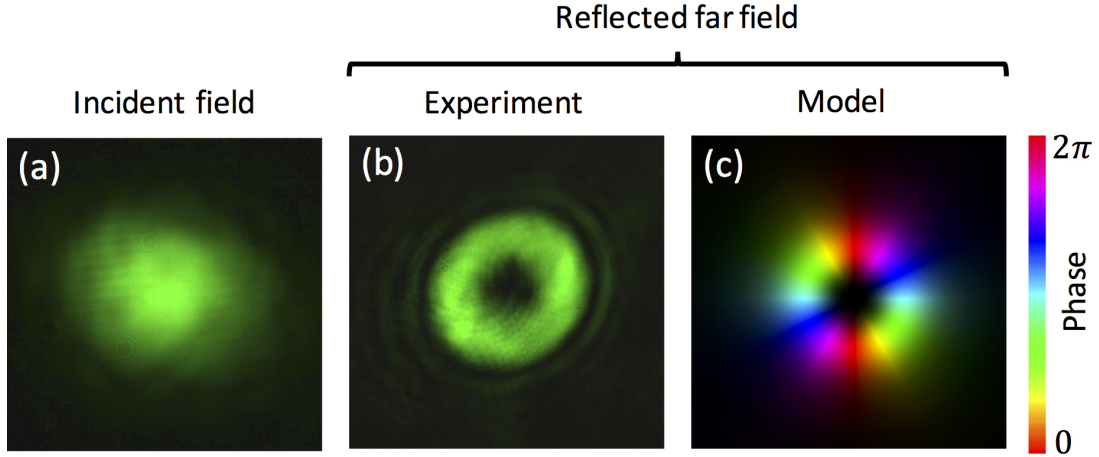


Figure 2.8: (a) Incident Gaussian intensity profile on the sample collected by camera CCD_1 (see Fig. 2.7(a)). (b) Far field intensity profile collected by camera CCD_2 owing to the lens L placed in f - f configuration. (c) Calculated intensity and phase that correspond to panel (b). The luminance refers to the intensity and the colormap refers to the phase from 0 to 2π .

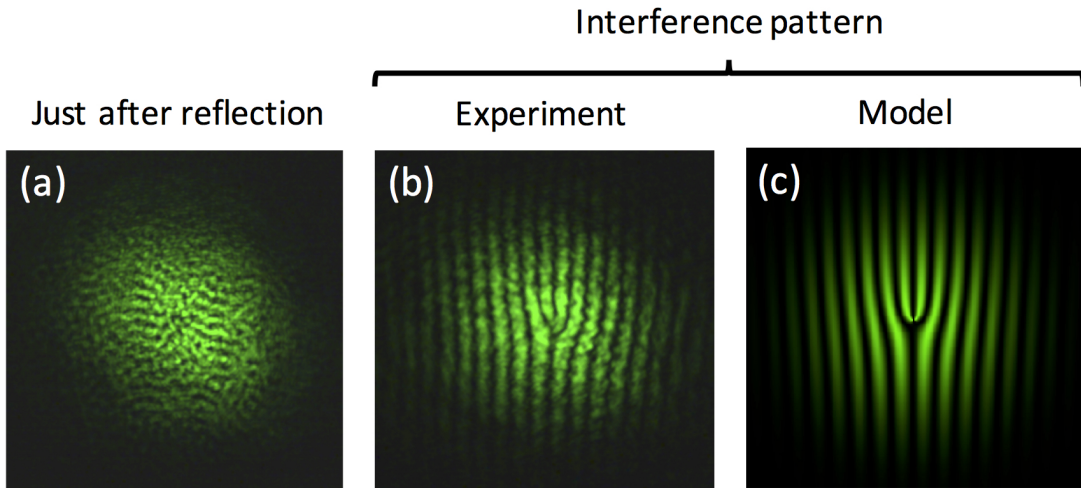


Figure 2.9: (a) Intensity profile of the field just after the reflection of a normally incident Gaussian beam off the Bragg-Berry mirror, which is collected by camera CCD_2 by placing the lens L in $2f$ - $2f$ configuration (see Fig. 2.7(a)). The speckle-like pattern is reminiscence of residual imperfections of the CLC structuring. (b) Interference pattern between the field that corresponds to panel (a) and a tilted reference Gaussian beam. A fork-like interference pattern of order two is observed. (c) Simulation of the observed singular interference pattern shown in panel (b).

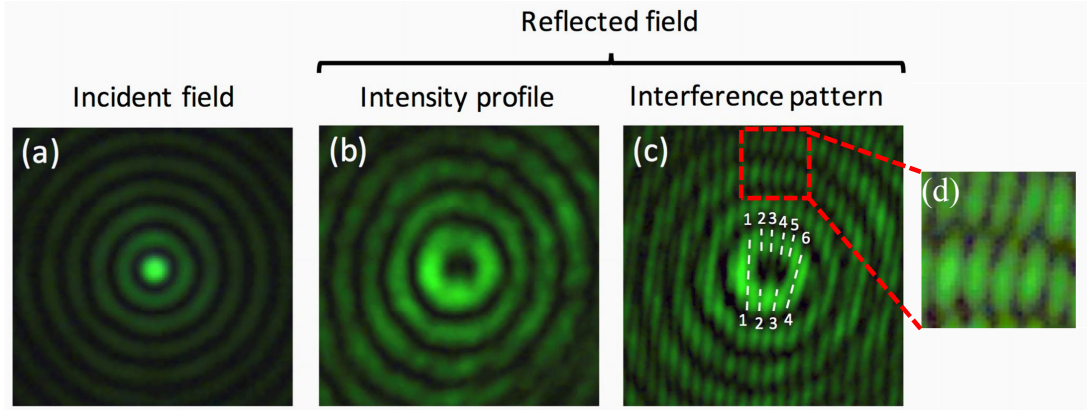


Figure 2.10: (a) Incident fundamental Bessel intensity profile on the sample collected by camera CCD_1 (see Fig. 2.7(a)). (b) Reflected field intensity profile collected by camera CCD_2 (see Fig. 2.7(a)). (c) Interference pattern between the field that corresponds to panel (b) and a reference Gaussian beam. A fork-like interference pattern of order two is observed. The Dashed segments and fringes numbering are given as a guide for the ease. (d) The enlargement of red framed region of panel (c) showing the shifted dark and light patterns of two successive rings indicates that the amplitude of Bessel field between the rings crosses the zero plan, which leads to π phase shift as the amplitude changes its sign.

exhibits a fork-like intensity pattern with two teeth, whose intensity modulation contrast is optimized by placing a polarizer before CCD_2 (see Fig. 2.7(a)). This confirms experimentally that the mirror behaves as an effective reflective singular phase mask with topological charge 2. The latter “near field” observations are confronted with simulations in Fig. 2.9(c) that displays the intensity pattern $|\Phi G + G_{\text{ref}}|^2$ where G_{ref} refers to the reference Gaussian beam whose propagation direction is slightly tilted with respect to that of the probed field.

Then, we formally extend above topological shaping of light to diffraction-free optical fields. This is done by preparing the incident field as a co-handed circularly polarized fundamental Bessel beam, by placing a glass axicon in the course of above incident Gaussian beam [122], between the beam splitters BS_1 and BS_2 (see Fig. 2.7(a)). The incident intensity pattern collected by the camera CCD_1 is shown in Fig. 2.10(a), which corresponds to an axicon with full-apex cone angle of 178° . The reflected field after a few centimeters of propagation is imaged on CCD_2 and shown in Fig. 2.10(b). The corresponding intensity pattern is representative of the expected higher-order Bessel beam as expected from the reflective phase mask $\psi(\phi)$, whose order two is unveiled by interferometry as shown in Fig. 2.10(c) where a tilted Gaussian reference arm is used. Indeed, by counting the fringes around the central part of the pattern, one can retrieve the characteristic 4π exploration of the phase along a closed path surrounding

the center of the probed beam. Interestingly, the shift between dark and light patterns of successive (see Fig. 2.10(d)) rings indicates the well known feature of Bessel beams, namely that the amplitude of Bessel field quasi-periodically crosses the zero plane (changes its sign) along the radial direction, which leads to π phase shift as the amplitude changes its sign.

2.3.4 Polychromatic features

Finally, we explore the polychromatic behavior of the Bragg-Berry mirror in the visible domain by replacing the monochromatic laser source with a supercontinuum laser source. The corresponding setup is depicted in Fig. 2.11(a), where the reflected light from BB mirror is spectrally dispersed by using a dispersion prism. The resulting spectrum is observed on a black screen placed in the imaging plane of CCD–long-range-objective system. The incident light is prepared to have co-handed circularly polarization state by tuning the relative orientation between

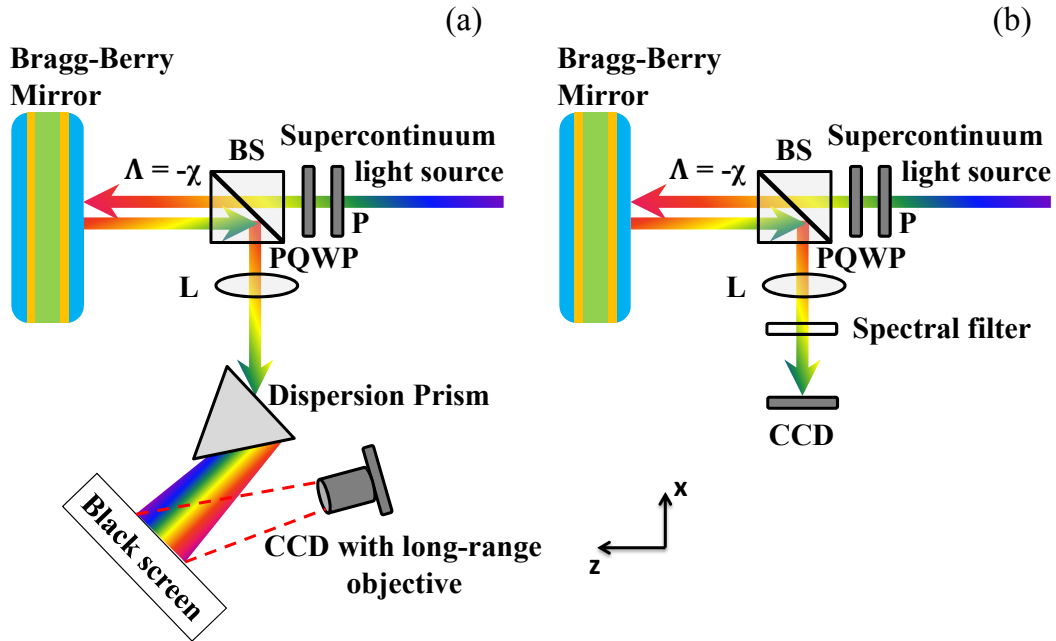


Figure 2.11: (a) Experimental setup for the extraction of reflected broadband optical vortex spectrum from an co-handed circularly polarized ($\Lambda = -\chi$) normal incident beam of supercontinuum laser source on the charge one Bragg-Berry mirror. (b) Same setup of panel (a) but instead of dispersion prism the set of spectral filters are used to extract the far-field patterns of reflected broadband optical vortex, which are detected by CCD camera. BS: beam splitter, L: lens, P: polarizer, PQWP: polychromatic quarter wave plate.

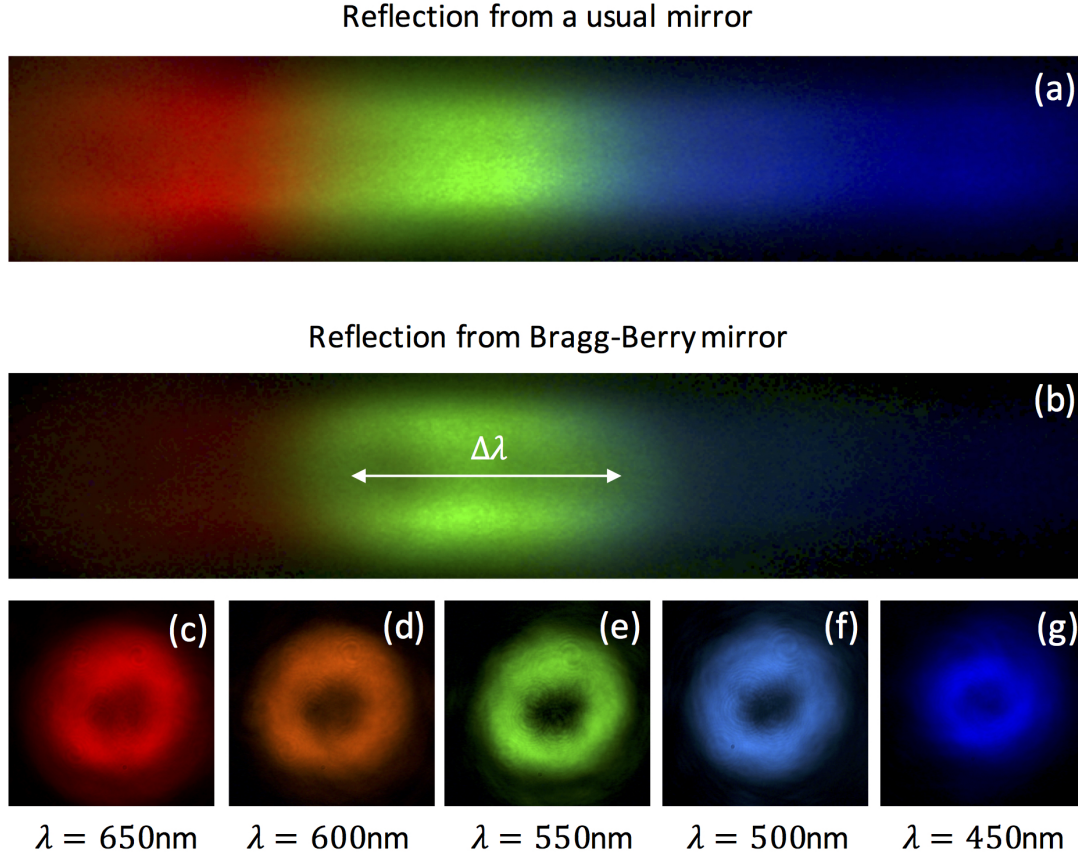


Figure 2.12: (a) Supercontinuum laser source spectrum corresponding to the Fig. 2.11(a) setup having a standard mirror installed instead of BB mirror. (b) The reflected broadband vortex spectrum from charge one Bragg-Berry mirror corresponding to the setup of Fig. 2.11(a). (c–g) Selection of far field vortex beam intensity profiles for a set of spectral filters (see the corresponding setup in Fig. 2.11(b)).

the linear polarizer (P) and the polychromatic quarter wave plate (PQWP) until the incident beam is totally reflected. The spectrum of incident supercontinuum Gaussian beam is extracted by replacing the BB mirror with a standard mirror Fig. 2.12(a). The Bragg reflection spectrum corresponding to BB mirror exhibits its characteristic high reflectance photonic bandgap $\Delta\lambda$ Fig. 2.12(b). However, we observe that the singular nature of Bragg-reflected field goes beyond the spectral region of photonic bandgap. This is illustrated in the bottom part of Fig. 2.12 that shows the far-field intensity patterns of the Bragg-reflected polychromatic vortex beams with topological charge 2 for a set of spectral filters chosen to filter the reflected wavelength from 450 to 650 nm by step of 50 nm (see Fig. 2.11(b)). Nevertheless, from Fig. 2.12(c) to Fig. 2.12(g), the quality of the generated optical vortex beam is decreased outside the photonic bandgap,

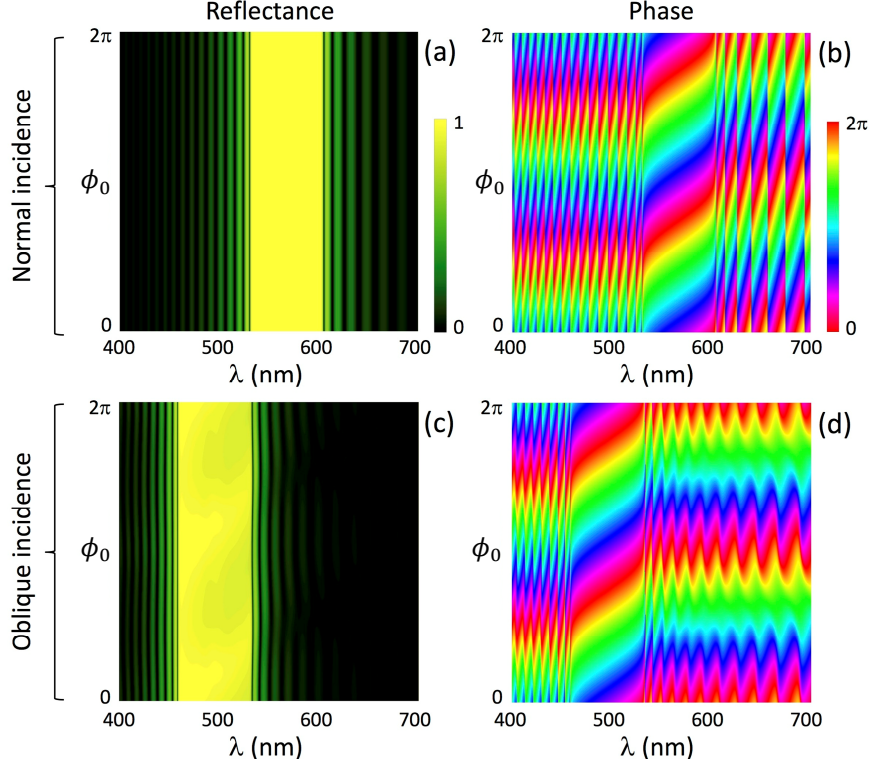


Figure 2.13: (a,b) Reflectance and phase spectra of the helicity-preserved light field component of the reflected field for Bragg-polarized incident field at normal incidence as a function of ϕ_0 . (c,d) Same as in (a) and (b) for 30° incident angle in the glass substrate. Calculations are made using the refractive indices parallel and perpendicular to the director of our liquid crystal mixture, namely $n_e = 1.7013$ and $n_o = 1.5064$, and glass substrate refractive index $n_{\text{glass}} = 1.52$.

where the reflected signal is low. To our understanding, this is due to the larger acquisition time used for CCD camera, hence lower signal-to-noise ratio, as one can see in Figs. 2.12(c, g). Several factors can alter topological shaping purity as well, such as the imperfect refractive index matching conditions between glass substrate and the average refractive index of the anisotropic medium [77] and the presence of photoalignment layers. In practice, this can be easily achieved by using either external fields (thermal, electrical, magnetic) effects or oblique incidence that are well-known to drastically shift the bandgap [107]. However, both methods shift the photonic bandgap keeping its width relatively unchanged, while in the next section we will demonstrate another solution towards the ultra-broadening the photonic bandgap of BB mirror.

We stress that although the reflected intensity is obviously wavelength dependent outside the circular photonic bandgap, the purity of the generated vortex is wavelength independent. This is illustrated in Figs. 2.13(a,b) where the re-

flectance and phase spectra of the helicity-preserved reflected field for incident Bragg-polarized light is calculated by Berreman 4×4 matrix formalism as a function of the helices orientation ϕ_0 of the CLC, see Figs. 2.7(b,c). Therefore, our approach does not require the use of post polarization filtering as is the case of usual transmissive q -plate. Moreover, the robustness of the pure broadband optical vortex generation versus the angle of incidence is illustrated in Fig. 2.13(c) and Fig. 2.13(d) for 30° external incidence angle in glass substrate. Note that the two main effects of oblique incidence are (i) to shift photonic bandgap to the blue spectral region and (ii) to break axisymmetry, both effects being more pronounced as the incidence angle increases, as one can see from the modulated reflectance versus ϕ_0 in Fig. 2.13(c). This emphasizes the large acceptance angle of Bragg-Berry mirrors.

Summarizing, we have demonstrated that flat spin-orbit reflective optical elements enable complex phase engineering of light fields, whatever their diffractive or non-diffractive nature. In general, the use of anisotropic chiral metamaterials may offer exotic photonic bandgaps that are valid for both incident circular polarizations and extended till ultrashort or extremely high wavelength regions [123]. Moreover, the sensitivity of liquid crystals to external fields should bring tunable or self-induced operating conditions. On the other hand, state-of-the-art point-by-point photoalignment techniques allow considering arbitrary singular or non-singular patterns [124, 125], that could immediately be exploited for the development of BB optical elements. Finally, recalling that Bragg-Berry mirrors have no restrictions in terms of cell thickness (see Sec. 2.2.3) and that their curvature may lead to additional topological shaping features [126, 127], this work should foster the development of spin-orbit photonic technologies.

2.4 Ultra-broadband Bragg-Berry mirrors

2.4.1 Position of the problem

In general, CLC with uniform pitch has only first-order photonic bandgap, which is defined in $n_o p < \lambda < n_e p$ spectral region, which is very often less than 100 nm. However, it is known that the chiral materials possessing non-uniform chirality can provide with higher-order photonic bandgaps [128] or can broaden their photonic bandgap proportional to the pitch gradient of chirality (see [129, 130]). Gradient-pitch CLCs have been created mainly by the following ways: diffusion of two CLC films with long and short pitches that are in tight contact, UV-illumination gradient in polymeric materials, temperature gradient or electric/magnetic fields applied to the CLCs of uniform pitches [131]. Accordingly, we propose to combine the topological beam shaping capabilities of Bragg-Berry mirrors with the ultra-broadband capabilities of CLCs. Experimental demonstration of ultra-broadband vortex generation endowed with extreme robustness

against large oblique incidences will be carried out by using gradient-pitch Bragg-Berry mirrors.

2.4.2 Sample preparation

In this section we report on the preparation of ultra-broadband Bragg-Berry mirror using thermal diffusion of two CLC films with long and short pitches [132] in order to induce a pitch gradient in Bragg-Berry mirrors with the aim of widening their photonic bandgap. At first, a planar homogeneous gradient-pitch CLC is prepared in order to observe the ultra-broadband light reflection and realize the dynamic geometric phase experiment over a wide spectral range. Once this has been validated, we moved to the preparation of ultra-broadband BB mirrors, at second stage. Both, planar homogeneous and planar inhomogeneous samples (differing only by their photoalignment layers of glass substrates) are prepared by using the same materials and protocol within the framework of a collaboration with G. Agez from Toulouse University (France).

The used materials are CLC oligomers from Wacker Chemie GmbH with $n_e = 1.72$ and $n_o = 1.42$ effective extraordinary and ordinary refractive indices. The molecular structure of the material consists of a siloxane cyclic chain to which is attached, via aliphatic spacers, two types of side chains: an achiral mesogen and a chiral cholesterol-bearing mesogen. The pitch of the helical structure and therefore the reflection wavelength depends on the molar percentage of the chiral mesogene in the molecule. This percentage is 31% in the case of *Silicon Red* (SR), 40% for *Silicon Green* (SG) and 50% for *Silicon Blue* (SB). The cholesteric phase appears between 180–210°C (clearing temperature range) and 40–50°C (glass-transition temperature range). By freezing the film in a glassy solid state the cholesteric structure and its optical properties are kept at room temperature.

A tri-layer sample was elaborated by stacking three different 10µm thick CLC oligomers layers: SR–SG–SB. The SR and SB film were confined between a

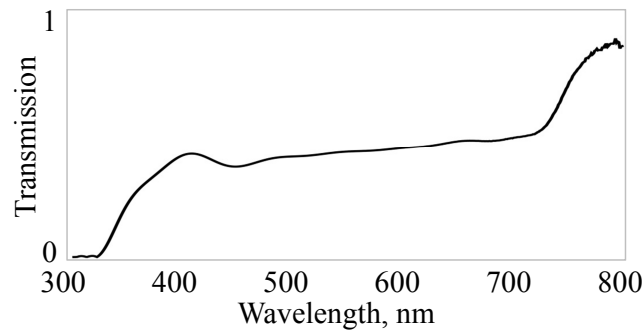


Figure 2.14: Typical transmission spectrum of homogeneous gradient-pitch CLC sample.

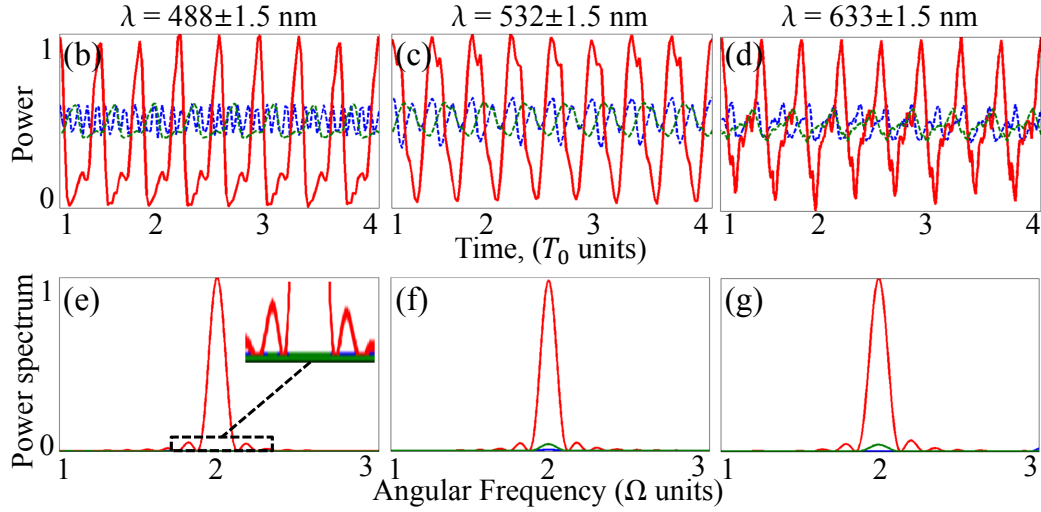


Figure 2.15: (a, b, c) Periodic signals acquired by the photodetector PD shown in Fig 2.3(a) for Bragg (green line), Fresnel (blue line) and equivalent Bragg-Fresnel (red line) reflected signals analyzed by $\lambda = (488 \text{ nm}, 532 \text{ nm}, 633 \text{ nm})$ filters of $\pm 1.5 \text{ nm}$ spectral width, respectively. (d, e, f) Power Fourier spectrum of the three cases of (a, b, c). Power Fourier spectra of Bragg and Fresnel signals are in the level of noise at the foot of the main peak.

specific radial anchoring glass and a lamella. The SG layer were confined between two lamellae. The samples were kept at 80°C (cholesteric phase) for 10 minutes to form a texture provided by photoalignment layer. Then we put the samples in the freezer for 15 minutes at low temperature (-18°C) to obtain glassy solid layers. At this temperature the lamellae can be easily taken off. The free-standing SG layer was sandwiched between the SR and SB semi-free films. Finally the RBG tri-layer sample several times was annealed at 80°C during 5 minutes to initiate an inter-diffusion of the 3 species and obtain a continuous pitch gradient structure with a ultra-broadband reflection. Fig. 2.14 corresponds to the typical transmission spectrum of homogeneous gradient-pitch CLC sample prepared by above mentioned procedure. It shows that the photonic bandgap of sample covers almost all the visible region of light. The next step is therefore to explore to which extent the geometric phase shaping also applies for such sample, as it has been shown for uniform pitch CLCs in the Sec. 2.2.

2.4.3 Spectral exploration of dynamic geometric phase

The dynamic geometric phase experiment for the homogeneous gradient-pitch CLC is performed by using a similar setup to that reported in Fig. 2.3(a) and a supercontinuum source instead of the monochromatic one. Following the protocol described in Sec. 2.2, Figs. 2.15(b,c,d) show the Bragg, Fresnel and Bragg-

Fresnel-reflected lights power dependencies on time using interference filters for three typical wavelengths, $\lambda = (488 \pm 1.5 \text{ nm}, 532 \pm 1.5 \text{ nm}, 633 \pm 1.5 \text{ nm})$. Similarly to the case of uniform CLCs (see Fig. 2.5), here the Bragg-Fresnel reflected light also undergoes much stronger oscillations at 2Ω frequency than Bragg or Fresnel contributions taken individually (see Figs. 2.15(e,f,g)), where Ω is the frequency of sample mechanical rotation. We note that the oscillations are noticeably distorted compared to our previous experiment, which caused wider peaks in power Fourier spectrum at 2Ω frequency. Several reasons, such as not perfectly planar alignments of CLC helices, some inhomogeneity between them, possible small differences between their pitch gradients or, in general, not perfect alignment of experimental setup can cause observed distortions. However, observed imperfections can not question the existence of geometric phase for reflected light from gradient-pitch cholesteric liquid crystals.

2.4.4 Gradient-pitch Bragg-Berry mirror demonstration

Once it has been clarified that gradient-pitch properties does not alter the geometric phase existence, the remaining demonstration consists to implement optical vortex generation using a gradient-pitch inhomogeneous CLC sandwiched between two charge one photoalignment layers. The corresponding experiment is performed using the setup shown in Fig 2.16(a), which corresponds to a Michelson interferometer scheme. Note that we used a polarizing beam splitter (PBS) instead of a non-polarizing beam splitter, otherwise the Fresnel contribution of the reflected beam and the reference beam reflected from the mirror would have the same polarizations, which would prevent post-selection via polarization optics. PBS initially splits the circularly polarized incidence in two orthogonal linear polarization (LP) states and collects them when they are reflected from CLC and from mirror in the same polarization states. Here the point is to benefit from the natural imperfection of the PBS. Indeed, ideally, the reflected light from the mirror having similar LP state than that of the incident beam would return back to the laser source. However, in practice, the PBS redirects a small fraction of that field, which thus interferes with the reflected light from the CLC sample. The incident Gaussian field of supercontinuum laser source (see Fig 2.16(b)) reflects from charge one ($q = 1$) gradient-pitch BB mirror and captured by CCD camera in the focal plane of L2 lens, see Fig 2.16(c) where the reference beam coming from mirror is blocked. We used a second polarizer, P2, in orthogonal orientation to the incidence polarization, in order to get rid of the Fresnel contribution from the reflected beam, since this sample is similar to the previously studied one regarding the absence of an antireflection coating on its glass substrates. Fig 2.16(d) corresponds to the interference pattern between reflected vortex and reference beams and discloses the charge 2 phase singularity of the

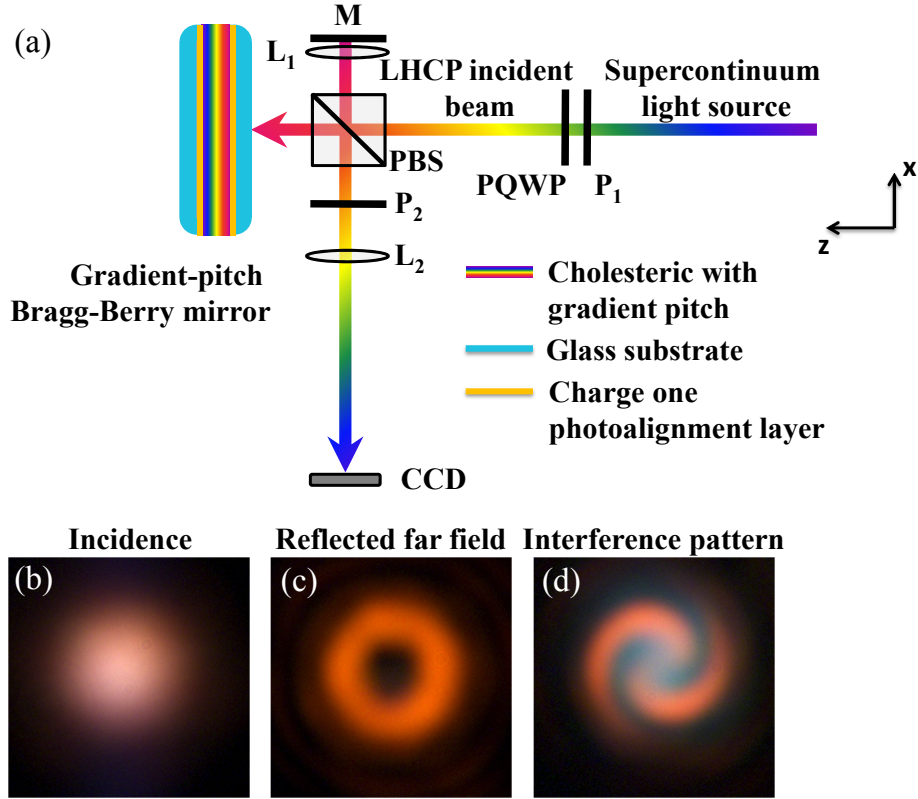


Figure 2.16: (a) *Experimental setup based on a Michelson interferometer in order to observe the reflected charge two vortex generated by a charge one gradient-pitch Bragg-Berry mirror and disclose its charge two singularity by interfering with reference Gaussian beam. M: mirror, $L_{1,2}$: lenses with $f = 500\text{mm}$ and $f = 300\text{mm}$ focal lengths, respectively, PBS: polarizing beam splitter, $P_{1,2}$: linear polarizers, PQWP: polychromatic quarter-wave plate, CCD: imaging camera (b) The intensity profile of incident supercontinuum Gaussian field. (c) The intensity profile of reflected far field vortex detected by CCD camera. (d) The interference pattern between the field corresponding panel (c) and a coaxial reference Gaussian beam.*

reflected vortex beam. In order to get a interference patterns like Fig 2.16(d) one has to change the curvatures between reflected vortex and reference beams, which is done by placing the lens L1 just before the mirror.

Then we used seven interference filters covering all the visible domain, that are placed before CCD camera, in order to disclose the spectral content of polychromatic vortex field shown in Fig 2.16(c), see Figs 2.17(a–g). Afterwards, a reflective diffractive grating (blazed wavelength reflective diffraction grating provided from Thorlabs with model number GR13-0605) is used in the place of CCD camera to disperse the reflected vortex (see Fig 2.17(a)) as in the Sec. 2.3 when the dispersion prism was used. One can see that the dispersed spectrum of vortex

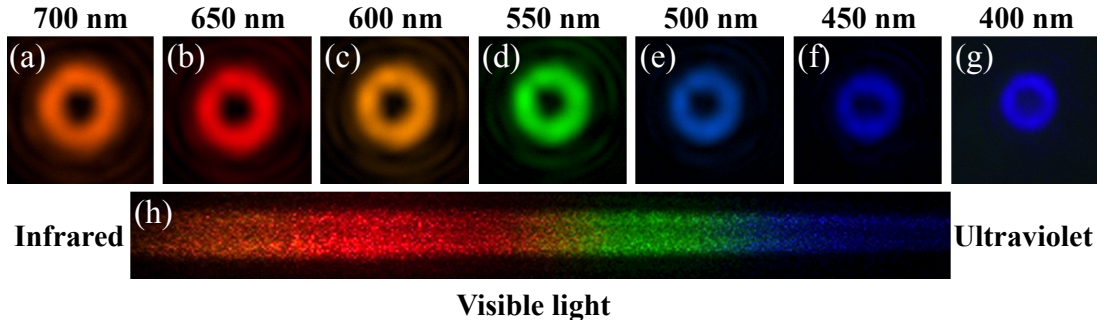


Figure 2.17: (a–g) The spectral components of Fig 2.16(c) vortex intensity distribution analyzed by set of interference filters from 400 nm to 700 nm. (h) The corresponding spectrum of vortex beam using reflective diffraction grating.

fills all the region of visible light. The noticeable decrease of reflected vortices waist radiuses towards blue wavelength region is observed in the case of uniform BB mirrors too (see Figs. 2.12(c–g)) and is associated with the properties of supercontinuum laser source (shorter wavelengths originally have smaller waist radiuses).

As shown in the previous section, the topological shaping properties of Bragg-Berry mirrors are expected to be robust to the angle of incidence, however, at the expense of a blue-shift. Such a property is tested for the gradient-pitch BB mirror using a linearly polarized supercontinuum Gaussian beam impinging on the sample at various external incident angles α_{ext} , namely $\alpha_{\text{ext}} = (2^\circ, 10^\circ, 20^\circ, 30^\circ, 40^\circ, 50^\circ, 60^\circ, 70^\circ)$. The reflected vortex beam is then analyzed by using the crossed-linear polarizer in order to clean the Fresnel contribution of the reflected field arising from air/substrate interface. Finally, a CCD camera with lens in $f - f$ configuration and a reflective diffraction grating are used in order to detect reflected far field vortices (see Figs. 2.18(i–p)) and their spectral contents (see Figs. 2.18(a–h)). The quality of reflected vortices are very robust and almost does not change for all the incidence angles. However, in some extent they lose the long-wavelength region of their spectra. In general it is expected that whole spectrum entirely move to the short-wavelength region, as observed in Fig. 2.13(c). However, we can't detect such effect because of the spectral limitations of our CCD camera (from 400 nm to 900 nm). Nevertheless, it remains unclear that the latter spectral blue-shift straightforwardly apply to the case of an inhomogeneous sample. First, the shorter wavelengths are very near to the absorption boundary of used material. Then, if the incident wavelength is smaller than the pitch value of chiral material, besides Bragg reflection, higher orders of reflections should also be accounted. However, we want to emphasize that according to the Berreman method the photonic bandgap should be shifted much more towards short-wavelength region than in this experiment we have ob-

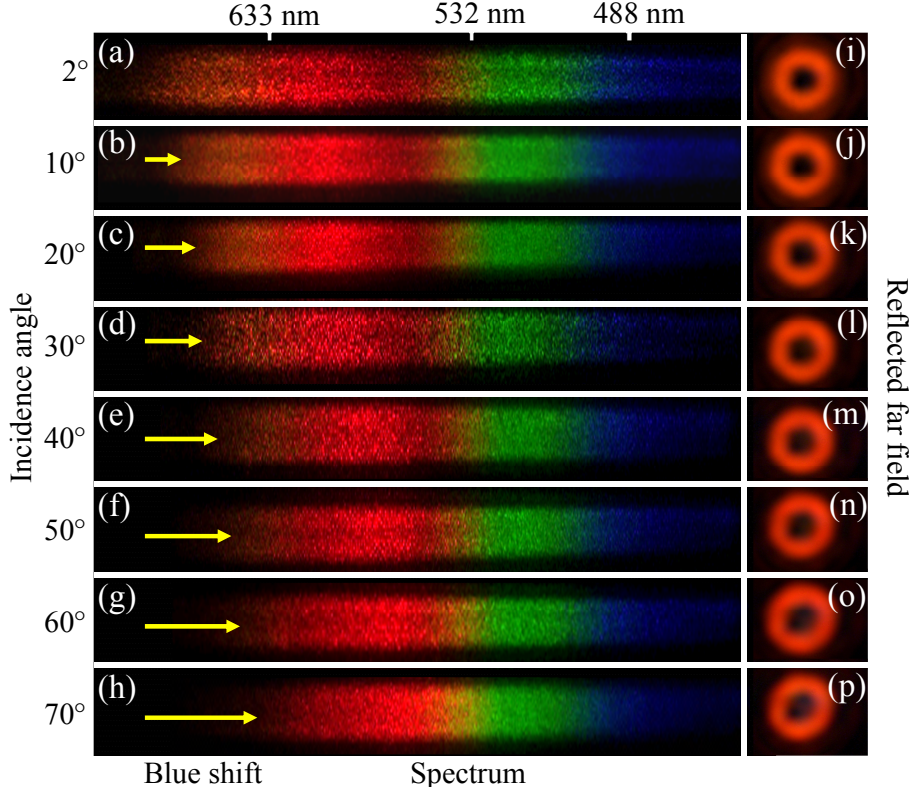


Figure 2.18: (a–h) The spectra of reflected far field vortices corresponding to the oblique incidences of supercontinuum Gaussian beam at $\alpha_{\text{ext}} = 2^\circ, 10^\circ, 20^\circ, 30^\circ, 40^\circ, 50^\circ, 60^\circ, 70^\circ$ angles on charge one gradient-pitch Bragg-Berry mirror. (i–p) The corresponding intensity profiles of reflected vortices.

served. The approximate estimation of blue-shifted spectral region depending on the incident angle can be done by the following formula $\lambda = \lambda_0 \cos(\alpha_{\text{int}})$, where λ is the center of blue-shifted photonic bandgap, λ_0 is the center of photonic bandgap at normal incidence and α_{int} is the internal incidence angle that can be calculated by applying the Snell's law. Namely, $\alpha_{\text{int}} = \sin^{-1}(\sin(\alpha_{\text{ext}})/n_{\text{av}})$, where $n_{\text{av}} = ((n_e^2 + 2n_o^2)/3)^{1/2} \approx 1.53$ is the average refractive index of used CLC. Accordingly, assuming $\lambda_0 = 550$ nm (see Fig. 2.17(h)), the blue-shifted photonic bandgap corresponding to the $\alpha_{\text{ext}} = 70^\circ$ is centered at $\lambda \approx 430$ nm, while experimentally we have detected relatively weaker blue shift. However, the provided estimation is working well in the case of small incidence angle of beam on the homogeneous CLC with uniform pitch, while in the case of large incidence angle of beam on the inhomogeneous CLC with gradient-pitch neither the mentioned analytical method nor the Berreman numerical method are not tested to our knowledge [133]. Experimentally, we conclude that the observed robust behaviour indicates that Bragg reflection, especially for oblique incident light, is

different for Bragg-Berry mirrors and it is subject of our further investigation.

2.5 Bragg-Berry q-plates

2.5.1 Position of the problem

In previous sections we have introduced that BB mirrors can shape the phase of incident co-handed circularly polarized beam in reflection. Particularly, we have demonstrated the reflective broadband vortex generation from charge one BB mirror. However, this approach of vortex generation (beam shaping in general) has a limitation that prevent from full spin-orbit functionality, i.e. spin-controlled topological shaping. Indeed, BB mirror relies on the use of co-handed circularly polarized incident beam and consequently the generated vortex (beam shaping) in reflection has the circular polarization of incident beam, see 2.2(a). Here we address the following question: could a BB mirror become a BB q-plate? Or, in other words, could we benefit from the broadband topological shaping of BB mirrors and spin controlled topological shaping of q-plates at the same time?

In this section, we extend the use of BB mirrors in beam shaping towards arbitrary polarization state for the incident beam. In general, there are two basic methods to achieve polarization independence from circular Bragg reflection. One is based on the stacking of CLC layers of $\chi = \pm 1$ chiralities [134] and the other is based on the use of standard mirror placed behind a CLC layer, that can have either positive or negative chirality [135]. Here, we use the latter method that has the merit of simplicity, hence is better towards practical applications. In particular, we show that an incident circularly polarized beams with $\Lambda = \pm\chi$ give almost total reflections of circularly polarized vortex beams from mirror-backed BB mirror. Then, we demonstrate the reflective vector vortex beam generation from incident linearly polarized beam on the same system. Consequently, above mentioned demonstrations will allow us to consider the mirror-backed BB mirror as a q-plate, hence a Bragg-Berry q-plate or a BB q-plate.

2.5.2 Mirror-backed uniform Bragg mirror

The case of circularly polarized incident light of $\Lambda = \pm\chi$ helicities on the mirror-backed homogeneous CLC layer is depicted in Fig. 2.19, where the case of a conventional CLC is also provided for the sake of comparison. In the latter case, an incident circularly polarized light with $\Lambda = -\chi$ state is almost totally reflected while with a helicity $\Lambda = +\chi$ state is almost totally transmitted. Note that in both cases the helicities are preserved upon reflection or transmission. On the other hand, as reported in [135], a mirror-backed planar homogeneous CLC exhibits a Bragg reflection for $\Lambda = \pm\chi$ helicities of the incident circularly polarized field. According to that article the following “ray-optics” explanation is provided: the

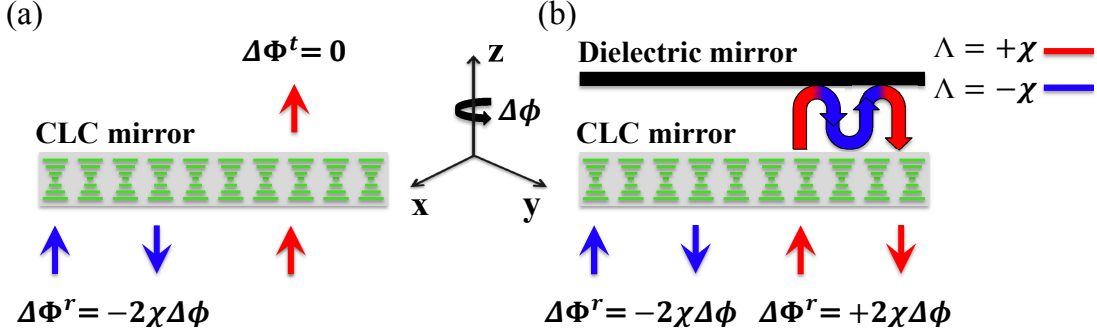


Figure 2.19: (a) Sketch of the incident light reflection or transmission depending on its polarization state on planar homogeneous CLC mirror of $\chi = 1$ chirality. The geometric phases $\Delta\Phi^r$ and $\Delta\Phi^t$ of reflected and transmitted lights are acquired from the angular offset, $\Delta\phi$, of cholesteric mirror in (x, y) transverse plane (see Sec. 2.3.2). (b) “ray-optics” description of light propagation impinging on mirror-backed planar homogeneous CLC mirror. The geometric phases $\Delta\Phi^r$ and $\Delta\Phi^t$ of reflected and transmitted fields are acquired from the $\Delta\phi$ angular offset of cholesteric mirror in (x, y) transverse plane. Blue and red arrows correspond to the RHCP and LHCP states of lights respectively.

incident circularly polarized light with $\Lambda = +\chi$ helicity is almost totally transmitted from CLC by keeping its helicity, then it is reflected from mirror, which is associated with the helicity-flipping. Afterwards, it is Bragg-reflected from the opposite side of the CLC without helicity change. Then, helicity-flipping reflection again occurs on the mirror, and finally transmission through the CLC without helicity change takes place. This is illustrated in Fig. 2.19(b), where arrows with red and blue colors refer to $\Lambda = +\chi$ and $\Lambda = -\chi$, respectively.

That being said, let us consider that the CLC layer as presented in Fig. 2.19(b) is rotated in the (x, y) plane by an angle $\Delta\phi$ (similar to the dynamic geometric phase experiment of Sec. 2.2). According to the dynamic geometric phase experiment of Sec. 2.2, the incident light with $\Lambda = -\chi$ reflects from mirror-backed CLC with $\Delta\Phi^r = -2\chi\Delta\phi$ geometric phase, while the incident light with $\Lambda = +\chi$, according to the mentioned “ray-optics” interpretation, reflects from mirror-backed CLC with $\Delta\Phi^r = 2\chi\Delta\phi$ geometric phase, since it is Bragg-reflected from the opposite side of the CLC layer. Generalizing, the geometric phase acquired at reflection for $\chi = \pm 1$ chirality and $\Lambda = \pm 1$ incident helicity is

$$\Delta\Phi^r = 2\Lambda\chi\Delta\phi. \quad (2.7)$$

We stress that a similar phenomenon occurs in reflection in the case of conventional q-plate, as discussed in the Sec. 1.1.2. Indeed, in that case an incident light with helicity $\Lambda = \pm 1$ leads to a transmitted phase factor $\exp(i2\Lambda q\phi)$ (see 1.6). This encourages us to use the charge one BB mirror of Sec. 2.3 placed in front

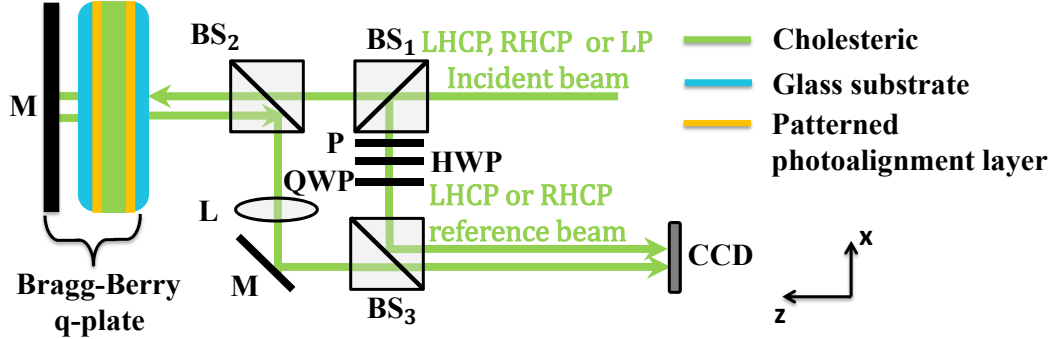


Figure 2.20: Experimental setup for optical vortex generation from normal incident beam of LHCP, RHCP or LP states on the BB q-plate of $q = 1$ charge. Reference beam of LHCP or RHCP states is used to interfere with the reflected vortex in order to disclose its optical singularity. *M*: mirror, $BS_{1,2,3}$: beam splitters, *L*: lens, *P*: polarizer, *HWP*: half-wave plate, *QWP*: quarter-wave plate, *CCD*: imaging device.

of a standard mirror towards the realization of a BB q-plate.

2.5.3 Mirror-backed Bragg-Berry mirror

From the “ray-optics” description depicted in Fig. 2.19(b) and the ensuing determination of Eq. 2.7, we expect that the circularly polarized reflected vortex from an incident light beam with $\Lambda = \pm 1$ changes its orbital state by

$$\Delta\ell = 2\Lambda\chi q. \quad (2.8)$$

We stress that in compression with conventional q-plate, the Bragg-Berry q-plates give another degree of freedom towards beam orbital angular shaping. That is the chirality, χ , of the CLC.

The experimental demonstration is made by using the setup depicted in Fig. 2.20. In contrast to the setup of the previous section, see Fig. 2.7(a), this setup allows incident and reference beams to have LHCP, RHCP or LP states. The CCD camera, in conjunction with lens, *L*, placed in $f - f$ configuration, is used to detect the far fields of reflected incident Gaussian beams of LHCP, RHCP and LP states. In order to disclose the phase singularities of reflected beams, RHCP and LHCP reference beams are also prepared. In practice, the distance between the standard and Bragg-Berry mirrors is set to be much shorter than the Rayleigh distance of the incident Gaussian beam. Otherwise, two independently processed LHCP and RHCP reflected beams propagated different distances would have different $w(z)$ radiuses in the same transverse plane (see Eq. 1 and following text about $w(z)$ dependence on z).

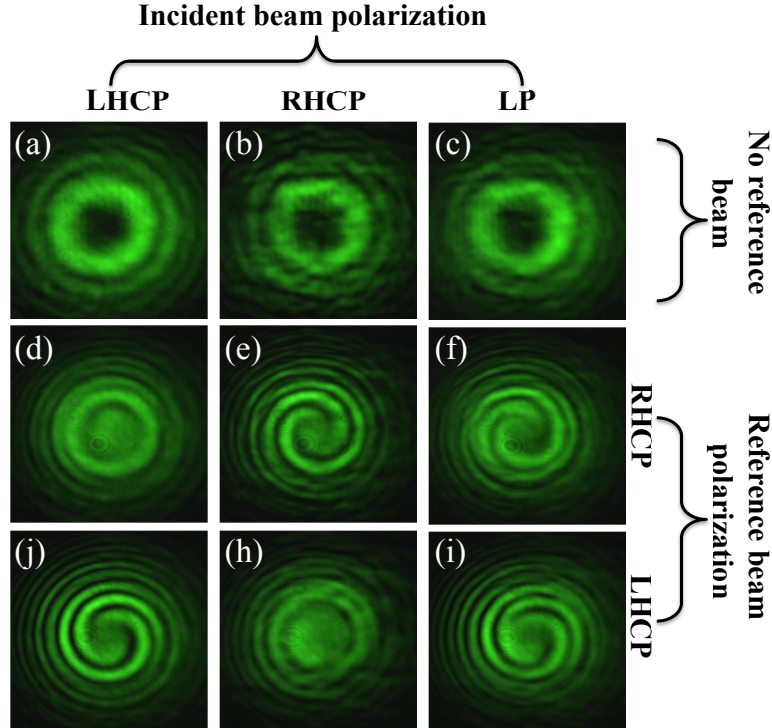


Figure 2.21: The first row shows the reflected far field intensity profiles of incident LHCP, RHCP and LP Gaussian beams, respectively. The second and third rows show their interference patterns with RHCP or LHCP reference Gaussian beams, respectively.

The captured intensity profiles of reflected doughnuts of incident LHCP, RHCP or LP Gaussian beams as well as their interference patterns with LHCP and RHCP reference beams are presented in Fig. 2.21. Several conclusions can be made from these experimental results:

- The charge one BB q-plate equally reflects the incident beam of any polarization into a vortex beam. This can be qualitatively assessed by visual inspection of equivalent luminosities of Figs. 2.21(a,b,c) that are all recorded with same incident beam power and camera acquisition time.
- The helicity of the reflected vortex field is that of the incident field, as expected from the “ray-optics” description of Fig. 2.19. Indeed, their interferences with orthogonal polarization states of Figs. 2.21(d,h) does not show an existence of singularity. The observed low-contrast interference rings in the LHCP/RHCP (Figs. 2.21(d)) and RHCP/LHCP (Figs. 2.21(h)) situations are most probably the indication of low-weight Fresnel contribution in the reflected field from CLC/glass interface. Indeed, since it has an orthogonal polarization with respect to the Bragg reflected vortex, it can interfere with the reference beam.

- Right and left circularly polarized incident beams result phase singularities with opposite topological charge $\ell = \pm 2$ in reflection, see Figs. 2.21(e,j).
- Linearly polarized incident beam generates a vector vortex beam of charge two in reflection, see Figs. 2.21(e,f,i).

All above mentioned statements allow us to conclude that the mirror-backed BB mirror of order q can be considered as a reflective q-plate, which thus deserve to be called Bragg-Berry q-plate.

Since the case of incident linearly polarized beam offers a platform for the spatio-temporal control of vector beam, we dedicate the next section to that particular situation.

2.6 Spatio-temporally modulated vector beams from Bragg-Berry q-plates

The standard mirror behind CLC layer of Bragg-Berry q-plate is responsible for the Bragg reflection of incident beam having circular polarization with handedness opposite to the sign of medium chirality (cross-handed circular polarization), see Fig. 2.19(b). From the “ray-optics” representation it follows that the co- and cross-handed circularly polarized beams experience different optical paths before to be reflected. On the other hand, in Sec. 2.5, we did not mention a requirement of a special distance, d , between the standard and the Bragg-Berry mirrors (except that $d \ll z_R$). Therefore, a reasonable question arises: what is the consequence on the reflected field when d varies by Δz ? Without loss of generality, hereafter we assume that the Bragg-Berry mirror is fixed, whereas the rear standard mirror is displaced along the z axis. Before to move the case of Bragg-Berry q-plate, which requires a charge q inhomogeneous CLC in front of standard mirror, let us first analyze the case of mirror-backed homogeneous CLC.

2.6.1 Tunable feature of mirror-backed CLCs

Let us discuss the consequence on the reflected field when the standard mirror is displaced by Δz along the z axis in the case of an homogeneous planar CLC. Obviously, the incident beam of co-handed circular polarization state ($\Lambda = -\chi$) is not affected, while the incident beam of cross-handed circular polarization state ($\Lambda = \chi$) will change its phase by $\Delta\Phi = 8\pi\Delta z/\lambda$, namely, four times the phase delay $2\pi\Delta z/\lambda$ due to the double reflection of ($\Lambda = \chi$) beam between the homogeneous CLC and the standard mirror. Next, we describe the reflection of a linearly polarized incident plane wave (say along the z axis) by representing its polarization state on the circular polarization basis, namely $\mathbf{e}_x = (\mathbf{e}_{+\Lambda} + \mathbf{e}_{-\Lambda})/\sqrt{2}$,

where $\mathbf{e}_\Lambda = (\mathbf{x} + i\Lambda\mathbf{y})/\sqrt{2}$

$$\mathbf{E}_{\text{in}} = \frac{E_0}{\sqrt{2}} e^{-i(\omega t - kz)} (\mathbf{e}_{+\Lambda} + \mathbf{e}_{-\Lambda}), \quad (2.9)$$

$$\mathbf{E}_{\text{out}} = \frac{E_0}{\sqrt{2}} e^{-i(\omega t + kz)} (\mathbf{e}_{+\chi} + e^{i\Delta\Phi} \mathbf{e}_{-\chi}). \quad (2.10)$$

Accordingly the following transformations are taken account: $\mathbf{e}_{+\chi} \rightarrow \exp(i\Delta\Phi)\mathbf{e}_{-\chi}$, because the light with $\Lambda = \chi$ helicity transmits from CLC and reflects back from standard mirror by acquiring the phase $\Delta\Phi$ and by flipping the vector $\mathbf{e}_{+\chi} \rightarrow \mathbf{e}_{-\chi}$, while the light with $\Lambda = -\chi$ is Bragg reflected from CLC by only flipping the vector $\mathbf{e}_{-\chi} \rightarrow \mathbf{e}_{+\chi}$. Simplifying Eq. 2.10 one gets

$$\mathbf{E}_{\text{out}} = E_0 e^{-i(\omega t + kz)} e^{i\Delta\Phi/2} (\cos(\Delta\Phi/2)\mathbf{x} + \chi \sin(\Delta\Phi/2)\mathbf{y}). \quad (2.11)$$

Above expression allows to reveal that a LP incident beam is reflected in a LP state but the polarization plane is rotated in (x, y) transverse plane by the angle $\gamma = \Delta\Phi/2$, namely

$$\gamma = \frac{4\pi\Delta z}{\lambda}. \quad (2.12)$$

When the homogeneous CLC is replaced by inhomogeneous CLC with charge q , an incident plane wave with helicity Λ is reflected with a phase factor $\exp(i\ell\phi)$ with $\ell = 2\Lambda\chi q$ (see Eq. 2.8). Therefore a similar analyses for an incident LP plane wave along the z axis gives

$$\mathbf{E}_{\text{out}} = \frac{E_0}{\sqrt{2}} e^{-i(\omega t + kz)} (e^{-i2q\phi} \mathbf{e}_{+\chi} + e^{i\Delta\Phi} e^{i2q\phi} \mathbf{e}_{-\chi}). \quad (2.13)$$

Which can be rewritten as

$$\mathbf{E}_{\text{out}} = E_0 e^{-i(\omega t + kz)} e^{i\Delta\Phi/2} (\cos(\Delta\Phi/2 + 2q\phi)\mathbf{x} + \chi \sin(\Delta\Phi/2 + 2q\phi)\mathbf{y}). \quad (2.14)$$

The electric field given by Eq. 2.14 describes a charge $\ell = 2q\chi$ vector field, where each vector is additionally rotated in transverse plane by angle $\gamma = \Delta\Phi/2$. Let us note that in the particular case when $q = 0$ Eq. 2.14 turns to the Eq. 2.11.

In general, the rotation of composite vectors of vector field (except charge one ($\ell = 1$) vector field) by the same angle corresponds to the entire rotation of vector field by that angle. This is illustrated in Fig. 2.22 where $\ell = (0, 1, 2, 3)$ vector fields are simulated for $\gamma = (0, \pi/4, \pi/2, 3\pi/4, \pi)$ angles. In the case of $\ell = 1$, depending on the angle γ , the charge one vector field rotates from radial to azimuthal vector fields. Namely, in the case of radial vector beam, each point of beam has a linear polarization pointed towards the center of beam, in the case of azimuthal vector beam, each point of beam has a linear polarization tangential to the circle constructed by that point and the center of the beam.

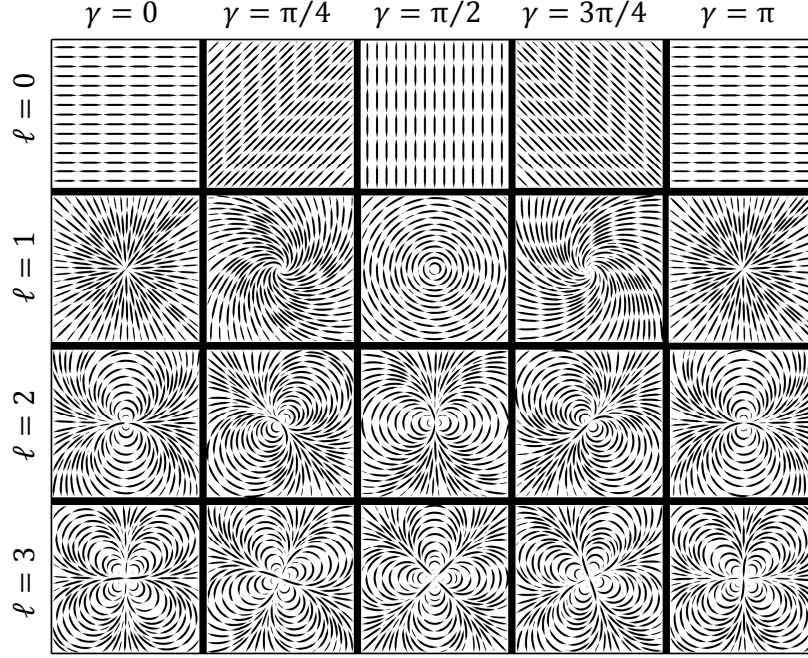


Figure 2.22: Vector fields of $\ell = (0, 1, 2, 3)$ charges for $\gamma = (0, \pi/4, \pi/2, 3\pi/4, \pi)$ angles, which refer to the in-plane rotations of each individual vector.

One can see from Eq. 2.11 and Eq. 2.14 that the total reflected field of both cases change with the periods of $\Delta z_0 = \lambda/2$. Importantly, the linear polarization state azimuth of their each point changes with the periods of $\Delta z_0 = \lambda/4$, since $\gamma \rightarrow \gamma + \pi$ corresponds to the same linear polarization state. More precisely, in the case of LP incident beam on the homogeneous CLC, the reflected field changes its linear polarization direction in the transverse plane by the periods of $\Delta z_0 = \lambda/4$. Similarly, in the case of LP incident beam on inhomogeneous CLC, the reflected vector field changes its composite linear polarization directions in the transverse plane with the periods of $\Delta z_0 = \lambda/4$ causing its entire rotation in the transverse plane (except the case of $\ell = 1$) with the same periods of Δz_0 .

Importantly, in both cases of homogeneous and inhomogeneous CLCs, after the projection of reflected field by linear polarizer, one detects the same $\Delta z_0 = \lambda/4$ periods of oscillating intensity patterns. Without loss of generality, the following example will demonstrate that. Let us take the orientation of linear polarizer along the x axis. In both cases, the intensities of projected output fields can be calculated by $I = |\mathbf{E}_{\text{out}} \cdot \mathbf{x}|^2$ using the Eqs. 2.11, 2.14 and 2.12. Namely, for the case of homogeneous CLC one gets $I_{\text{hom}} \propto \cos(4\pi\Delta z/\lambda)^2$, and for the case of inhomogeneous CLC one gets $I_{\text{inhom}} \propto \cos(4\pi\Delta z/\lambda + 2q\phi)^2$. Consequently, in both cases the detected intensity profiles exhibit oscillations with $\Delta z_0 = \lambda/4$ periods.

Since the subwavelength displacement of the standard mirror can change

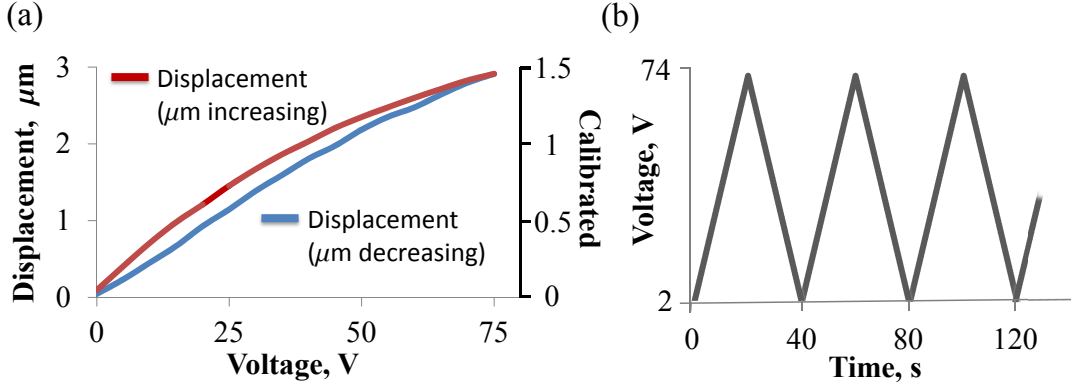


Figure 2.23: (a) Load-free piezo stage displacement under applied positive electric voltage provided by Thorlabs. The right axis corresponds to the mirror-loaded piezo stage displacement calibrated by setup of Fig. 2.24(a). (b) The periodically varying voltage applied on the piezo stage.

the vectorial characteristics of the reflected field significantly, an experimental demonstration implies fine motion control of standard mirror. We thus choose a piezoelectric translation stage. The voltage-controlled amplitude of the displacement depends on the applied load, therefore we cannot rely on load-free and lot-dependent calibration specifications provided by supplier and a special calibration corresponding to our experiment is required.

2.6.2 Calibration of the piezoelectric translation stage

We used the piezoelectric translation stage (or in short piezo stage) TA0505D024 from Thorlabs, which provides a continuous displacement up to $\Delta z_{\max} = 2.8 \mu\text{m}$ when a positive electric voltage is applied, see the typical load-free calibration data in Fig. 2.23(a) provided by Thorlabs. Red and blue curves are showing the piezo stage displacement when the voltage is increased from $V_{\min} = 0 \text{ V}$ to $V_{\max} = 75 \text{ V}$ and decreased from V_{\max} to V_{\min} , respectively.

In our case, we use a 1 inch dimensional, 5 mm thick standard mirror. To perform a calibration of mirror-loaded piezo displacement, an interference setup is assembled, see Fig 2.24(a). Basically, our protocol consists to measure the interference between Fresnel-reflected beams from two microslides (thin transparent layers of glasses), one being fixed while the other being attached to the piezo stage. In addition, the mirror that will be used in the next experiments is fixed on the piezo stage in order to have the piezo stage loaded as close as possible to the planned measurements. In practice a diffusing paper is placed between the mirror and microslide in order to diffuse the unwanted transmitted light from the microslide and not reflect it back from the mirror, see the sketch shown in Fig 2.24(a). Note that the weights of the diffusing paper and the microslide can

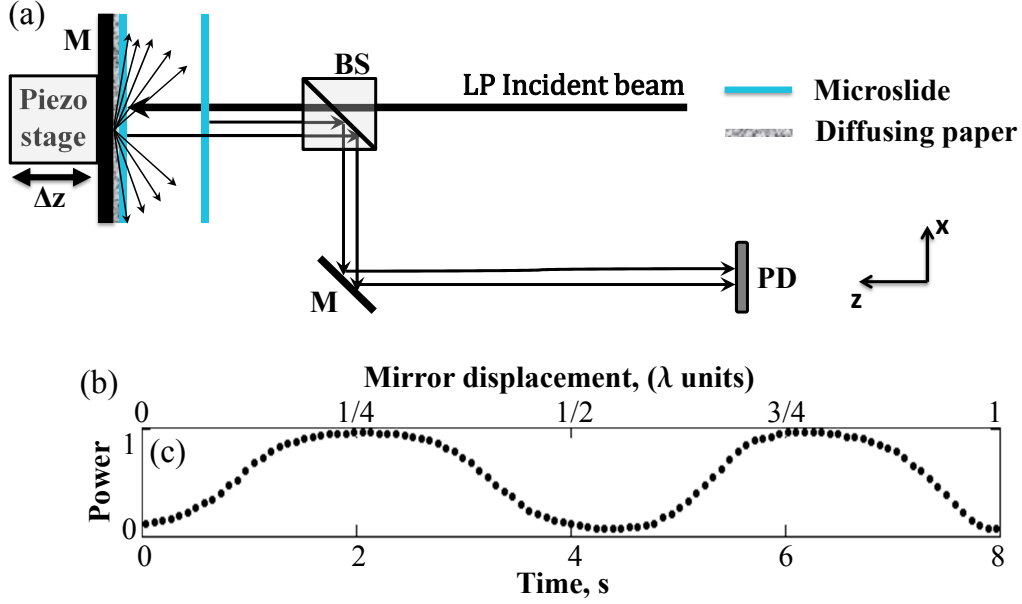


Figure 2.24: (a) Piezo stage calibration by experimental setup based on the interference between LP incident beam reflections from fixed and moving microslides. The transmitted part of beam from moving microslide undergoes diffusing reflection from the paper placed behind it. The mirror is mounted on piezo stage deliberately in order to have the same amount of load applied to the piezo stage as in the farther experiments (the weights of diffusing paper and microslide can be neglected compared with the mirror). (b) Detected power oscillations of reflected lights in the setup of panel (a) under applied voltage of Fig. 2.23 (b) and in the periods of 8 seconds corresponds to the λ displacement of piezo stage.

be neglected compared to that of the standard mirror.

The incident linearly polarized beam first Fresnel-reflects from the fixed microslide and then Fresnel-reflects from the second microslide attached to the continuously moving piezo stage and the total reflected field is detected by photodetector. The continuous displacement of the piezo stage should thus bring an intensity oscillation due to the interference with a period of displacement $\Delta z_0 = \lambda/2$. In order to get a continuous displacement of piezo stage, we applied a periodic voltage on it, which is periodically changing from $V_1 = 2$ V up to $V_2 = 74$ V by $T = 40$ s period, as depicted in Fig. 2.23(b). We chose the applied voltages $V_1 > V_{\min}$ and $V_2 < V_{\max}$ in order to work safely regarding the limits of piezo stage. Obtained time-dependent intensity signal is shown in Fig. 2.24(b), which gives a time period of $\Delta t = 4$ s. This is associated with the voltage change $\Delta V = (V_2 - V_1)\Delta t/(T/2) = 14.4$ V, which corresponds to a displacement $\Delta z^{\text{spec}} = \Delta z_{\max} \cdot \Delta V/V_{\max} = 0.53 \mu\text{m}$. The estimated value from the generic specifications is thus larger than the expected one $\Delta z_0 = \lambda/2 = 0.266 \mu\text{m}$ by almost two

times. Assuming that the red and blue displacement curves of Fig. 2.23(a) have almost linear dependencies on voltage, we can calibrate them by the coefficient $\Delta z_0^{\text{exp}}/\Delta z_0^{\text{spec}} \approx 0.5$. The right side axis of Fig. 2.23(a) refers to the calibrated axis. The displacement dependence on applied voltage of mirror-loaded piezo stage being determined, we can move to the main experiments.

2.6.3 Tunable mirror-backed homogeneous CLC: experiment

In sec. 2.6.1 we have showed theoretically that LP incident beam on the mirror-backed homogeneous CLC changes its LP state azimuth in transverse plane by angle $\gamma = 4\pi\Delta z/\lambda$ when mirror moves along CLC by Δz . Here we demonstrate that experimentally. We use the piezo stage calibrated in Sec. 2.6.2.

The experimental setup is depicted in Fig 2.25(a). Accordingly, the incident LP beam first reflects from the homogenous CLC then from the moving mirror-loaded piezo stage and eventually passes through a linear polarizer before to be collected by a CCD camera. Fig 2.25(b) shows the time dependent integrated signal detected by the CCD camera. Obtained signal varies approximately twice faster than in the calibration case (the small deviation most probably comes due to the non perfect parallel alignment of the mirror and the CLC sample). This experimentally proves that the continuous displacement of mirror by $\Delta z = \lambda$ results to 2 full rotation of the plane of the reflected field (see Sec. 2.6.1). At the same time, this supports the “ray-optics” concept of double reflection between cholesteric and mirror illustrated in Fig. 2.19. Let us note that the power oscillations of both experiments are originally recorded for much longer period and their behaviour is same as presented in Fig. 2.24(b) and Fig. 2.25(b). Still there is an open question that we did not explain so far, namely the robust asymmetric power oscillation in the case of the mirror-backed CLC, see Fig. 2.25(b). The volumetric representation of recorder signal by CCD camera is presented in Fig. 2.25(c), which emphasizes the spatio-temporal features of the obtained modulation [116]. Three kinds of characteristics of the modulated signal are emphasized in Fig. 2.25(c): (i) The length of mirror displacement, Δz , which led to the rotation of reflected light LP state in transverse plane with period of $\lambda/4$; (ii) the time period of mirror displacement, which is also the length of recorded video; (iii) the length of the spatio-temporally modulated signal in space, which is equal to $c\Delta t$.

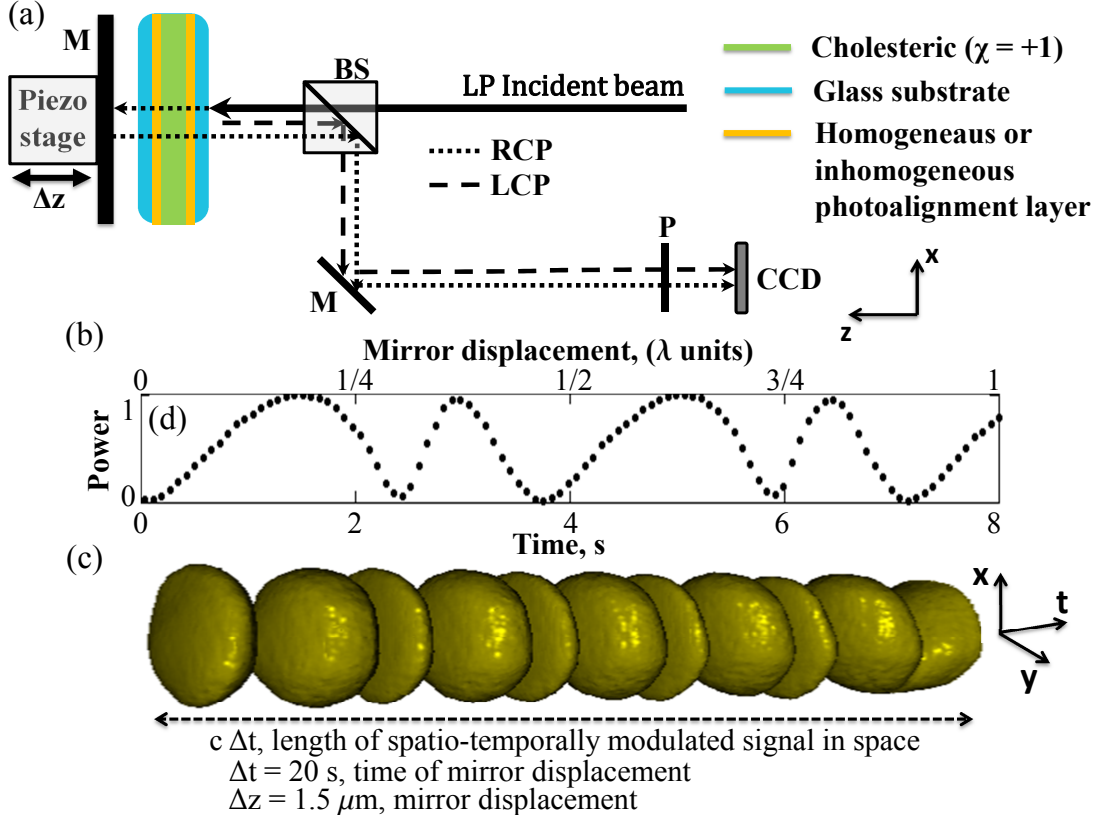


Figure 2.25: (a) Experimental setup for the detection of polarization plane rotation of the reflected beam from a planar homogeneous CLC with moving back-mirror. Piezo stage oscillates along the z axis with an amplitude Δz . (b) Integrated signal detected by the CCD camera that collects the total reflected light analyzed by linear polarizer for λ displacement of piezo stage over a time duration of 8 s. (c) Volumetric spatio-temporal presentation of the signal collected by the CCD camera. It corresponds to the $\Delta z = 1.5 \mu\text{m}$ displacement of piezo stage under applied voltage of Fig. 2.23 (b) over a time duration of $\Delta t = 20$ s. The spatio-temporally modulated signal has a $c\Delta t$ length in the space.

2.6.4 Tunable mirror backed inhomogeneous CLC: experiment

Eventually, we address the case of the planar inhomogeneous cholesteric sample. We use the same setup of Fig. 2.25(a), but with the charge one inhomogeneous CLC instead of the homogeneous one. Volumetric spatio-temporal presentation of projected vector field is shown in Fig. 2.26(a). It corresponds to the displacement of back-mirror by $\Delta z = 1.5 \mu\text{m}$ over the time duration of $\Delta t = 20$ s. Figs. 2.26(b–f) correspond to one full period rotation of projected vector field intensity pattern for $\Delta z = \lambda/4$ displacement of piezo stage over a time duration

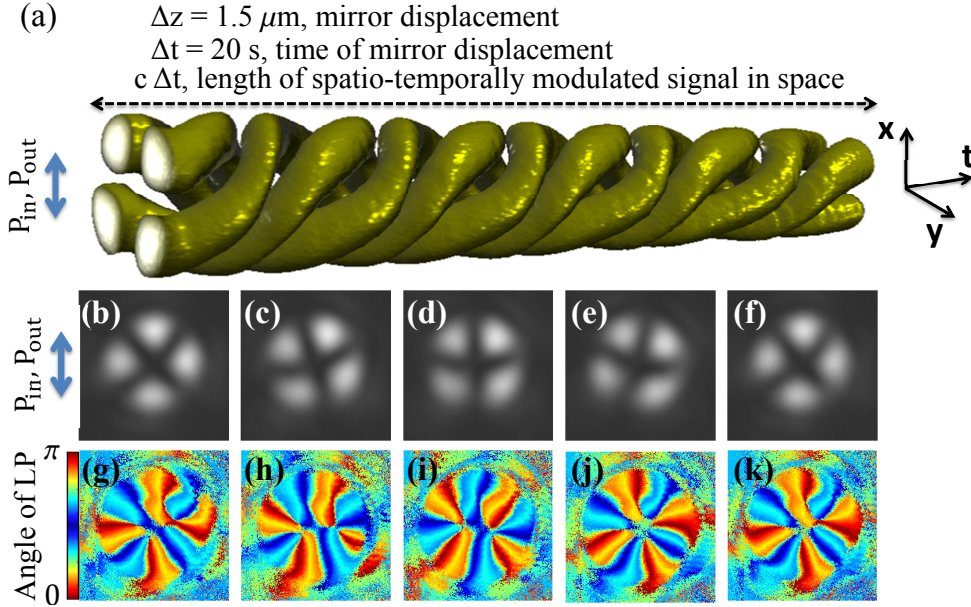


Figure 2.26: (a) Volumetric presentation of spatio-temporally modulated vector field analyzed by linear polarizer and detected in the same setup of Fig. 2.25(a), but instead of planar homogeneous CLC, charge one planar inhomogeneous CLC is used. It corresponds to the $\Delta z = 1.5 \mu\text{m}$ displacement of piezo stage under applied voltage of Fig. 2.23 (b) over a time duration of $\Delta t = 20 \text{ s}$. The spatio-temporally modulated signal has a $c\Delta t$ length in the space. (b–f) One full period rotation of transverse-plane intensity pattern of panel (a) modulated signal corresponding to $\Delta z = \lambda/4$ displacement of piezo stage over a time duration of 2 s. (g–k) The azimuthal maps of polarizations of same fields of (l–p) obtained by Salsa camera, which is placed instead of linear polarizer and CCD camera. The orientations of incident and analyzing polarizations are the same and presented by two blue arrows (P_{in} and P_{out}).

of 2 s. The dark crosses mean that over that region field is polarized orthogonal to the linear polarizer placed before CCD camera. As it was expected from Sec. 2.6.1, the period of rotating intensity pattern is $\Delta z = \lambda/4$.

In order to directly detect the polarization state of the reflected vector field without projecting it, we remove the linear polarizer and install the SALS camera instead of CCD camera. SALS is a full Stokes polarization camera, which performs live measurement of fields Stokes parameters as well as many other polarization-related parameters such as the “degree of polarization” (linear or circular), the “angle of polarization”, the “ellipticity angle” etc. In our case, we measure the angular map of linear polarization of reflected vector field, see Figs. 2.26(g–k). The experimental results of vector beam projections (Figs. 2.26(b–f)) as well as their linear polarization angular maps (Figs. 2.26(g–k))

give a good agreement with our theoretical predictions depicted in Fig. 2.22.

Spatio-temporal signals modulated in time and in space can enhance substantially the capacity of optical communication [136–140]. On the other hand, spatially modulated signals by phase and intensity are very actual in optomechanical manipulations [141–143]. Consequently, we think that the presented new method of spatio-temporal modulated beam generation can be useful towards investigations of high speed optical communication or in complex optomechanical manipulations.

One of the key element in our experimental setup, which induces the spatio-temporal modulation of vector beam, is the piezoelectric crystal. Recent studies show that vibration frequency of piezoelectric crystals can go beyond 100 MHz [144, 145], consequently such piezoelectric stages in our setup allow to induce very high frequency spatio-temporally modulated vector beams without use of expensive spatial light modulators or other complex interference technologies [146–149]. On the other hand, alternative method to that, can be electrooptical phase modulators relying on Pockel effect of nonlinear crystals placed between dielectric and Bragg-Berry mirrors, which can change the optical path of cross-circular polarized part of incident beam in GHz frequencies [150–152].

Conclusion and perspectives

In this work we have addressed two main issues of topological beam shaping: the modality and the polychromaticity. The first one enhances the degree of freedom of converted information adding a radial degree of freedom to the spin-orbit information of converted modal beam. The second one provides broadband spin-orbit beam shaping.

In chapter 1 we have theoretically proposed single anisotropic inhomogeneous dielectric flat medium, that we have called a modal q-plate, since it can convert the incident Gaussian beam into the pure Laguerre Gaussian beam of arbitrary radial and azimuthal indices depending on its optical properties. The idea of modal beam shaping is generic and relies on the simultaneous contributions of dynamic and geometric phases in the beam shaping. For that reason, the required optical characteristics of modal HG-plates, that convert the incident Gaussian beam into the pure Hermite Gaussian beams of arbitrary modes, are also introduced. The technological realization of such flat modal shapers maiden by anisotropic inhomogeneous dielectric medium is challenging to date. However, two different approaches, namely glassy quasi-modal q-plates and liquid crystal quasi-modal defects, are discussed experimentally and theoretically, that ease the technological difficulties by sacrificing the modality of beam shaping, to some extent. Fortunately, both methods principally can offer increase of modality vs decrees of conversion efficiency. Sec. 1.1 and Sec. 1.2 have led to the publication and submission of articles [153] and [154], respectively.

In chapter 2 we proposed a novel individual method of beam shaping based on the revealed Pancharatnam-Berry geometric phase in Bragg reflection from chiral optical media based on inhomogeneous azimuthal orientation of its chiral helices. We called a Bragg-Berry mirror such inhomogeneous flat chiral material. The experimental demonstration of novel kind of beam shaping is carried out by showing the broadband optical vortex reflection from charge one Bragg-Berry mirror using thin cholesteric liquid crystal (CLC) layer sandwiched by glass substrates coated by charge one planar photoalignment layer. Afterwards, ultra-broadband Bragg-Berry mirrors are realized based on the charge one inhomogeneous CLC sample having nonuniform chirality (pitch gradient) along the cell induced by thermal diffusion of three cholesteric liquid crystal layers with three different chiralities. We have showed that the optical vortex reflected from that sample exhibits ultra-broadband characteristics covering almost all the visible light region. Then, we upgrade the Bragg-Berry mirror achieving polarization

independent spin-orbital beam shaping, by using a standard mirror behind that and calling such configuration a Bragg-Berry q-plate. The demonstration of charge ± 2 optical vortex generations from incident right/left circularly polarized Gaussian beams on the charge one ($q = 1$) Bragg-Berry q-plate is carried out. We have showed, that the incident linearly polarized Gaussian beam generates a vector vortex beam in reflection. Finally, in the last section, we provoke the possibility of highly spatio-temporal modulation of vector fields from the periodical modulation of optical path between the standard and the Bragg-Berry mirrors. The experimental demonstration is carried out by placing the back-mirror on a piezoelectric translation stage and displacing it in a periodic manner. Sec. 2.2 and Sec. 2.3 have led to the publication of two articles, namely [126] and [155].

The results presented in this thesis bring a novel concept of modal beam shaping and provide a novel broadband reflective spin-orbit element, which in turn may open path for number of new research perspectives towards advanced novel spin-orbit elements. For example a new modal q-plate that overcomes previous limitations regarding the robustness of modality against the handedness of the incident circular polarization state or regarding the fully efficient modal conversion. Another novel spin-orbit element can be a “modal Bragg-Berry q-plate” that combining the concept of modality with the polychromaticity of Bragg-Berry mirror can generate polychromatic Laguerre-Gaussian beams or a “reconfigurable Bragg-Berry mirror” that benefiting from the tunability of cholesteric liquid crystals by electric field can shape the geometric phase of reflected polychromatic light in controlled manner. Finally, one can consider a “broadband complex beam shaper” that stacking Bragg-Berry mirrors with opposite chiralities and different topological charges can generate vector vortex beams with inhomogeneous polarization states on higher-order or hybrid-order Poincaré spheres [156, 157].

Bibliography

- [1] J. VAUGHAN AND D. WILLETTS, “Interference properties of a light beam having a helical wave surface”, *Optics Communications* **30**, 263 (1979).
- [2] S. KHONINA, V. KOTLYAR, M. SHINKARYEV, V. SOIFER, AND G. USPLENIEV, “The phase rotor filter”, *Journal of modern optics* **39**, 1147 (1992).
- [3] M. BEIJERSBERGEN, R. COERWINKEL, M. KRISTENSEN, AND J. WORDERDMAN, “Helical-wavefront laser beams produced with a spiral phase-plate”, *Optics Communications* **112**, 321 (1994).
- [4] G. RUFFATO, M. MASSARI, AND F. ROMANATO, “Generation of high-order Laguerre–Gaussian modes by means of spiral phase plates”, *Optics letters* **39**, 5094 (2014).
- [5] N. HECKENBERG, R. MCDUFF, C. SMITH, AND A. WHITE, “Generation of optical phase singularities by computer-generated holograms”, *Optics letters* **17**, 221 (1992).
- [6] J. ARLT, K. DHOLAKIA, L. ALLEN, AND M. PADGETT, “The production of multiringed Laguerre–Gaussian modes by computer-generated holograms”, *Journal of modern optics* **45**, 1231 (1998).
- [7] V. Y. BAZHENOV, M. VASNETSOV, AND M. SOSKIN, “Laser beams with screw dislocations in their wavefronts”, *Jetp Lett* **52**, 429 (1990).
- [8] G. BIENER, A. NIV, V. KLEINER, AND E. HASMAN, “Formation of helical beams by use of Pancharatnam–Berry phase optical elements”, *Optics letters* **27**, 1875 (2002).
- [9] P. CHEN, B.-Y. WEI, W. JI, S.-J. GE, W. HU, F. XU, V. CHIGRINOV, AND Y.-Q. LU, “Arbitrary and reconfigurable optical vortex generation: a high-efficiency technique using director-varying liquid crystal fork gratings”, *Photonics Research* **3**, 133 (2015).
- [10] S.-J. GE, W. JI, G.-X. CUI, B.-Y. WEI, W. HU, AND Y.-Q. LU, “Fast switchable optical vortex generator based on blue phase liquid crystal fork grating”, *Optical Materials Express* **4**, 2535 (2014).

-
- [11] Y. LIU, X. SUN, Q. WANG, AND D. LUO, “Electrically switchable optical vortex generated by a computer-generated hologram recorded in polymer-dispersed liquid crystals”, *Optics express* **15**, 16645 (2007).
- [12] E. BRASSELET, “Tunable optical vortex arrays from a single nematic topological defect”, *Physical Review Letters* **108**, 087801 (2012).
- [13] C. LOUSSERT, U. DELABRE, AND E. BRASSELET, “Manipulating the orbital angular momentum of light at the micron scale with nematic disclinations in a liquid crystal film”, *Physical Review Letters* **111**, 037802 (2013).
- [14] Y. OHTAKE, T. ANDO, N. FUKUCHI, N. MATSUMOTO, H. ITO, AND T. HARA, “Universal generation of higher-order multiringed Laguerre-Gaussian beams by using a spatial light modulator”, *Optics letters* **32**, 1411 (2007).
- [15] N. MATSUMOTO, T. ANDO, T. INOUE, Y. OHTAKE, N. FUKUCHI, AND T. HARA, “Generation of high-quality higher-order Laguerre-Gaussian beams using liquid-crystal-on-silicon spatial light modulators”, *J. Opt. Soc. Am. A* **25**, 1642 (2008).
- [16] L. ALLEN, M. W. BEIJERSBERGEN, R. SPREEUW, AND J. WOERDMAN, “Orbital angular momentum of light and the transformation of Laguerre-Gaussian laser modes”, *Physical Review A* **45**, 8185 (1992).
- [17] S. VAN ENK AND G. NIENHUIS, “Spin and orbital angular momentum of photons”, *EPL (Europhysics Letters)* **25**, 497 (1994).
- [18] K. Y. BLOKH, F. J. RODRÍGUEZ-FORTUÑO, F. NORI, AND A. V. ZAYATS, “Spin-orbit interactions of light”, *Nature Photonics* **9**, 796 (2015).
- [19] VINITSKIĬ, “Topological phases in quantum mechanics and polarization optics”, .
- [20] R. BHANDARI, “Polarization of light and topological phases”, *Physics Reports* **281**, 1 (1997).
- [21] E. HASMAN, G. BIENER, A. NIV, AND V. KLEINER, “Space-variant polarization manipulation”, *Progress in Optics* **47**, 215 (2005).
- [22] L. MARRUCCI, E. KARIMI, S. SLUSSARENKO, B. PICCIRILLO, E. SANTAMATO, E. NAGALI, AND F. SCIARRINO, “Spin-to-orbital conversion of the angular momentum of light and its classical and quantum applications”, *J. Opt.* **13**, 064001 (2011).

- [23] N. YU AND F. CAPASSO, “Flat optics with designer metasurfaces”, *Nature materials* **13**, 139 (2014).
- [24] E. RAHIMI AND K. ŞENDUR, “Femtosecond pulse shaping by ultrathin plasmonic metasurfaces”, *J. Opt. Soc. Am. B* **33**, A1 (2016).
- [25] J. BUTET AND O. J. MARTIN, “Evaluation of the nonlinear response of plasmonic metasurfaces: Miller’s rule, nonlinear effective susceptibility method, and full-wave computation”, *J. Opt. Soc. Am. B* **33**, A8 (2016).
- [26] V. ASADCHY, M. ALBOOYEH, AND S. TRETAKOV, “Optical metamirror: all-dielectric frequency-selective mirror with fully controllable reflection phase”, *J. Opt. Soc. Am. B* **33**, A16 (2016).
- [27] N. M. ESTAKHRI AND A. ALÙ, “Recent progress in gradient metasurfaces”, *J. Opt. Soc. Am. B* **33**, A21 (2016).
- [28] A. EPSTEIN AND G. V. ELEFTHERIADES, “Huygens’ metasurfaces via the equivalence principle: design and applications”, *J. Opt. Soc. Am. B* **33**, A31 (2016).
- [29] N. CHIOTELLIS AND A. GRBIC, “Analytical modeling of tensor metasurfaces”, *J. Opt. Soc. Am. B* **33**, A51 (2016).
- [30] A. KALVACH AND Z. SZABÓ, “Aberration-free flat lens design for a wide range of incident angles”, *J. Opt. Soc. Am. B* **33**, A66 (2016).
- [31] Y. LI, I. NIGO LIBERAL, AND N. ENGHETA, “Metatronic analogues of the Wheatstone bridge”, *J. Opt. Soc. Am. B* **33**, A72 (2016).
- [32] J. M. JAUCH AND F. ROHRlich, *The Theory of Photons and Electrons: The relativistic quantum field theory of charged particles with spin one-half* (Springer Science & Business Media, 2012).
- [33] X. MAITRE, E. HAGLEY, G. NOGUES, C. WUNDERLICH, P. GOY, M. BRUNE, J. RAIMOND, AND S. HAROCHE, “Quantum memory with a single photon in a cavity”, *Physical Review Letters* **79**, 769 (1997).
- [34] G. NOGUES, A. RAUSCHENBEUTEL, S. OSNAGHI, M. BRUNE, J. RAIMOND, AND S. HAROCHE, “Seeing a single photon without destroying it”, *Nature* **400**, 239 (1999).
- [35] A. MAIR, A. VAZIRI, G. WEIHS, AND A. ZEILINGER, “Entanglement of the orbital angular momentum states of photons”, *Nature* **412**, 313 (2001).

-
- [36] J. LEACH, M. J. PADGETT, S. M. BARNETT, S. FRANKE-ARNOLD, AND J. COURTIAL, “Measuring the orbital angular momentum of a single photon”, *Physical Review Letters* **88**, 257901 (2002).
- [37] J. LEACH, J. COURTIAL, K. SKELDON, S. M. BARNETT, S. FRANKE-ARNOLD, AND M. J. PADGETT, “Interferometric methods to measure orbital and spin, or the total angular momentum of a single photon”, *Physical Review Letters* **92**, 013601 (2004).
- [38] E. NAGALI, F. SCIARRINO, F. DE MARTINI, L. MARRUCCI, B. PICCIRILLO, E. KARIMI, AND E. SANTAMATO, “Quantum information transfer from spin to orbital angular momentum of photons”, *Physical Review Letters* **103**, 013601 (2009).
- [39] R. H. HADFIELD, “Single-photon detectors for optical quantum information applications”, *Nature photonics* **3**, 696 (2009).
- [40] B. NDAGANO, I. NAPE, B. PEREZ-GARCIA, S. SCHOLES, R. HERNANDEZ-ARANDA, F. ROUX, T. KONRAD, AND A. FORBES, “Quantum-key distribution with vector modes”, *Proc. of SPIE Vol 10120*, 101200X (2017).
- [41] A. E. SIEGMAN, *Lasers* (University Science Books, 1986).
- [42] M. HARRIS, C. HILL, AND J. VAUGHAN, “Optical helices and spiral interference fringes”, *Optics communications* **106**, 161 (1994).
- [43] M. CLIFFORD, J. ARLT, J. COURTIAL, AND K. DHOLAKIA, “High-order Laguerre–Gaussian laser modes for studies of cold atoms”, *Optics Communications* **156**, 300 (1998).
- [44] S.-C. CHU, Y.-T. CHEN, K.-F. TSAI, AND K. OTSUKA, “Generation of high-order Hermite–Gaussian modes in end-pumped solid-state lasers for square vortex array laser beam generation”, *Optics express* **20**, 7128 (2012).
- [45] H. LAABS AND B. OZYGUS, “Excitation of Hermite Gaussian modes in end-pumped solid-state lasers via off-axis pumping”, *Optics & Laser Technology* **28**, 213 (1996).
- [46] S. A. KENNEDY, M. J. SZABO, H. TESLOW, J. Z. PORTERFIELD, AND E. ABRAHAM, “Creation of Laguerre–Gaussian laser modes using diffractive optics”, *Physical Review A* **66**, 043801 (2002).
- [47] S.-C. CHU AND K. OTSUKA, “Doughnut-like beam generation of Laguerre–Gaussian mode with extremely high mode purity”, *Optics Communications* **281**, 1647 (2008).

- [48] M. S. SEGhilani, M. MYARA, M. SellaHi, L. LEGRATIET, I. SAGNES, G. BEAUDOIN, P. LALANNE, AND A. GARNACHE, “Vortex Laser based on III-V semiconductor metasurface: direct generation of coherent Laguerre-Gauss modes carrying controlled orbital angular momentum”, *Scientific Reports* **6**, 38156 (2016).
- [49] B. E. SALEH, M. C. TEICH, AND B. E. SALEH, *Fundamentals of photonics* (Wiley New York, 1991), Vol. 22.
- [50] Y.-X. REN, Z.-X. FANG, L. GONG, K. HUANG, Y. CHEN, AND R.-D. LU, “Digital generation and control of Hermite-Gaussian modes with an amplitude digital micromirror device”, *Journal of Optics* **17**, 125604 (2015).
- [51] S. KHONINA, V. KOTLYAR, R. SKIDANOV, V. SOIFER, P. LAAKKONEN, AND J. TURUNEN, “Gauss-Laguerre modes with different indices in prescribed diffraction orders of a diffractive phase element”, *Optics communications* **175**, 301 (2000).
- [52] P. CHEN, B.-Y. WEI, W. JI, S.-J. GE, W. HU, F. XU, V. CHIGRINOV, AND Y.-Q. LU, “Arbitrary and reconfigurable optical vortex generation: a high-efficiency technique using director-varying liquid crystal fork gratings”, *Photonics Research* **3**, 133 (2015).
- [53] V. LERNER, D. SHWA, Y. DRORI, AND N. KATZ, “Shaping Laguerre-Gaussian laser modes with binary gratings using a digital micromirror device”, *Optics letters* **37**, 4826 (2012).
- [54] Y.-X. REN, M. LI, K. HUANG, J.-G. WU, H.-F. GAO, Z.-Q. WANG, AND Y.-M. LI, “Experimental generation of Laguerre-Gaussian beam using digital micromirror device”, *Applied optics* **49**, 1838 (2010).
- [55] V. ARRIZÓN, U. RUIZ, R. CARRADA, AND L. A. GONZÁLEZ, “Pixelated phase computer holograms for the accurate encoding of scalar complex fields”, *J. Opt. Soc. Am. A* **24**, 3500 (2007).
- [56] T. ANDO, Y. OHTAKE, N. MATSUMOTO, T. INOUE, AND N. FUKUCHI, “Mode purities of Laguerre-Gaussian beams generated via complex-amplitude modulation using phase-only spatial light modulators”, *Optics letters* **34**, 34 (2009).
- [57] E. KARIMI AND E. SANTAMATO, “Radial coherent and intelligent states of paraxial wave equation”, *Optics letters* **37**, 2484 (2012).
- [58] B. SEPHTON, A. DUDLEY, AND A. FORBES, “Revealing the radial modes in vortex beams”, *Applied optics* **55**, 7830 (2016).

-
- [59] G. VALLONE, A. SPONSELLI, V. DAMBROSIO, L. MARRUCCI, F. SCIARRINO, AND P. VILLORESI, “Birth and evolution of an optical vortex”, *Optics Express* **24**, 16390 (2016).
- [60] Y. LI, J. KIM, AND M. J. ESCUTI, “Broadband orbital angular momentum manipulation using liquid crystal thin films”, *Proc. of SPIE OPTO* 827415 (2012).
- [61] F. BOUCHARD, H. MAND, M. MIRHOSSEINI, E. KARIMI, AND R. W. BOYD, “Achromatic orbital angular momentum generator”, *New Journal of Physics* **16**, 123006 (2014).
- [62] N. RADWELL, R. HAWLEY, J. GÖTTE, AND S. FRANKE-ARNOLD, “Achromatic vector vortex beams from a glass cone”, *Nature communications* **7**, (2016).
- [63] E. BRASSELET, Y. IZDEBSKAYA, V. SHVEDOV, A. S. DESYATNIKOV, W. KROLIKOWSKI, AND Y. S. KIVSHAR, “Dynamics of optical spin-orbit coupling in uniaxial crystals”, *Optics letters* **34**, 1021 (2009).
- [64] J. LEACH AND M. PADGETT, “Observation of chromatic effects near a white-light vortex”, *New Journal of Physics* **5**, 154 (2003).
- [65] D.-M. SPANGENBERG, A. DUDLEY, P. H. NEETHLING, E. G. ROHWER, AND A. FORBES, “White light wavefront control with a spatial light modulator”, *Optics express* **22**, 13870 (2014).
- [66] A. NIV, G. BIENER, V. KLEINER, AND E. HASMAN, “Polychromatic vectorial vortex formed by geometric phase elements”, *Optics letters* **32**, 847 (2007).
- [67] Y. TOKIZANE, K. OKA, AND R. MORITA, “Supercontinuum optical vortex pulse generation without spatial or topological-charge dispersion”, *Optics express* **17**, 14517 (2009).
- [68] L. HUANG *et al.*, “Dispersionless phase discontinuities for controlling light propagation”, *Nano letters* **12**, 5750 (2012).
- [69] R. R. ALFANO, “The supercontinuum laser source”, (1989).
- [70] W. J. WADSWORTH, A. ORTIGOSA-BLANCH, J. C. KNIGHT, T. A. BIRKS, T.-P. M. MAN, AND P. S. J. RUSSELL, “Supercontinuum generation in photonic crystal fibers and optical fiber tapers: a novel light source”, *J. Opt. Soc. Am. B* **19**, 2148 (2002).

- [71] K.-Y. KIM, A. TAYLOR, J. GLOWNIA, AND G. RODRIGUEZ, “Coherent control of terahertz supercontinuum generation in ultrafast laser–gas interactions”, *Nature photonics* **2**, 605 (2008).
- [72] P. HARIHARAN, “Broad-band superachromatic retarders”, *Measurement Science and Technology* **9**, 1678 (1998).
- [73] R. K. KOMANDURI, K. F. LAWLER, AND M. J. ESCUTI, “Multi-twist retarders: broadband retardation control using self-aligning reactive liquid crystal layers”, *Optics express* **21**, 404 (2013).
- [74] C. OH AND M. J. ESCUTI, “Achromatic diffraction from polarization gratings with high efficiency”, *Optics letters* **33**, 2287 (2008).
- [75] J. M. HERRERA-FERNANDEZ, J. L. VILAS, L. M. SANCHEZ-BREA, AND E. BERNABEU, “Design of superachromatic quarter-wave retarders in a broad spectral range”, *Applied optics* **54**, 9758 (2015).
- [76] N. V. TABIRYAN, S. V. SERAK, S. R. NERSISYAN, D. E. ROBERTS, B. Y. ZELDOVICH, D. M. STEEVES, AND B. R. KIMBALL, “Broadband waveplate lenses”, *Optics express* **24**, 7091 (2016).
- [77] M. FARYAD AND A. LAKHTAKIA, “The circular Bragg phenomenon”, *Advances in Optics and Photonics* **6**, 225 (2014).
- [78] R. BARBOZA, U. BORTOLOZZO, M. G. CLERC, AND S. RESIDORI, “Berry Phase of Light under Bragg Reflection by Chiral Liquid-Crystal Media”, *Physical Review Letters* **117**, 053903 (2016).
- [79] C. BAYON, G. AGEZ, AND M. MITOV, “Wavelength-tunable light shaping with cholesteric liquid crystal microlenses”, *Lab on a Chip* **14**, 2063 (2014).
- [80] J. KOBASHI, H. YOSHIDA, AND M. OZAKI, “Polychromatic optical vortex generation from patterned cholesteric liquid crystals”, *Physical Review Letters* **116**, 253903 (2016).
- [81] J. KOBASHI, H. YOSHIDA, AND M. OZAKI, “Planar optics with patterned chiral liquid crystals”, *Nature Photonics* (2016), doi: 10.1038/NPHOTON.2016.66.
- [82] E. HECHT, *Optics* (Addison Weley, 2002).
- [83] Y. SHIMOTSUMA, P. G. KAZANSKY, J. QIU, AND K. HIRAO, “Self-organized nanogratings in glass irradiated by ultrashort light pulses”, *Physical Review Letters* **91**, 247405 (2003).

-
- [84] M. SOSKIN AND M. VASNETSOV, “Singular optics”, *Progress in optics* **42**, 219 (2001).
- [85] M. R. DENNIS, K. O’HOLLERAN, AND M. J. PADGETT, “Singular optics: optical vortices and polarization singularities”, *Progress in Optics* **53**, 293 (2009).
- [86] O. D. LAVRENTOVICH, dans *Handbook of Liquid Crystals* (Wiley-VCH Verlag GmbH & Co. KGaA, 2014).
- [87] D. VOLOSCHENKO AND O. LAVRENTOVICH, “Optical vortices generated by dislocations in a cholesteric liquid crystal”, *Optics letters* **25**, 317 (2000).
- [88] E. BRASSELET, N. MURAZAWA, H. MISAWA, AND S. JUODKAZIS, “Optical vortices from liquid crystal droplets”, *Physical Review Letters* **103**, 103903 (2009).
- [89] E. BRASSELET AND C. LOUSSERT, “Electrically controlled topological defects in liquid crystals as tunable spin-orbit encoders for photons”, *Optics letters* **36**, 719 (2011).
- [90] R. BARBOZA, U. BORTOLOZZO, G. ASSANTO, E. VIDAL-HENRIQUEZ, M. CLERC, AND S. RESIDORI, “Vortex induction via anisotropy stabilized light-matter interaction”, *Physical Review Letters* **109**, 143901 (2012).
- [91] P. AUBOURG, J.-P. HUIGNARD, M. HARENG, AND R. MULLEN, “Liquid crystal light valve using bulk monocrystalline Bi 12 SiO 20 as the photoconductive material”, *Applied Optics* **21**, 3706 (1982).
- [92] E. BRASSELET, A. E. MIROSHNICHENKO, D. F. CHEN, W. KROLIKOWSKI, AND Y. S. KIVSHAR, “Polarizational nonlinear optical response of photonic structures with a liquid crystal defect”, *Optics letters* **34**, 488 (2009).
- [93] E. BRASSELET, “Singular optical manipulation of birefringent elastic media using nonsingular beams”, *Optics letters* **34**, 3229 (2009).
- [94] M. EL KETARA AND E. BRASSELET, “Self-induced nonlinear spin-orbit interaction of light in liquid crystals”, *Optics letters* **37**, 602 (2012).
- [95] P. PIERANSKI, B. YANG, L.-J. BURTZ, A. CAMU, AND F. SIMONETTI, “Generation of umbilics by magnets and flows”, *Liquid Crystals* **40**, 1593 (2013).

- [96] I. BUDAGOVSKY, A. ZOLOT'KO, D. KORSHUNOV, M. SMAYEV, S. SHVETSOV, AND M. BARNIK, "Generation of spiral dislocation of wave front in absorbing nematic liquid crystal", *Optics and Spectroscopy* **119**, 280 (2015).
- [97] A. RAPINI, "Umbilics: static properties and shear-induced displacements", *Journal de Physique* **34**, 629 (1973).
- [98] R. B. MEYER, "Point Disclinations at a Nematic-Isotropic Liquid Interface", *Molecular Crystals and Liquid Crystals* **16**, 355 (1972).
- [99] A. SAUPE, "Disclinations and properties of the directorfield in nematic and cholesteric liquid crystals", *Molecular Crystals and Liquid Crystals* **21**, 211 (1973).
- [100] M. SAKAMOTO, T. SASAKI, T. M. TIEN, K. NODA, N. KAWATSUKI, AND H. ONO, "Flexible and achromatic generation of optical vortices by use of vector beam recorded functionalized liquid crystals", *Applied Optics* **55**, 10427 (2016).
- [101] A. RAPINI, L. LÉGER, AND A. MARTINET, "Umbilics: Static and dynamic properties", *Le Journal de Physique Colloques* **36**, C1 (1975).
- [102] B. SON *et al.*, "Optical vortex arrays from smectic liquid crystals", *Optics express* **22**, 4699 (2014).
- [103] B. YANG AND E. BRASSELET, "Arbitrary vortex arrays realized from optical winding of frustrated chiral liquid crystals", *Journal of Optics* **15**, 044021 (2013).
- [104] A. K. SPILMAN AND T. G. BROWN, "Stress birefringent, space-variant wave plates for vortex illumination", *Applied optics* **46**, 61 (2007).
- [105] S. MOSCA *et al.*, "Photon self-induced spin-to-orbital conversion in a terbium-gallium-garnet crystal at high laser power", *Physical Review A* **82**, 043806 (2010).
- [106] E. A. KHAZANOV, O. V. KULAGIN, S. YOSHIDA, D. B. TANNER, AND D. H. REITZE, "Investigation of self-induced depolarization of laser radiation in terbium gallium garnet", *IEEE Journal of Quantum Electronics* **35**, 1116 (1999).
- [107] P. OSWALD AND P. PIERANSKY, *Nematic and Cholesteric Liquid Crystals: Concepts and Physical Properties Illustrated by Experiments* (Taylor & Francis, CRC, Boca Raton, FL, 2005).

-
- [108] D. W. BERREMAN AND T. L. SCHEFFER, “Bragg reflection of light from single-domain cholesteric liquid crystal films”, *Physical Review Letters* **25**, 577 (1970).
- [109] V. A. BELYAKOV, *Diffraction optics of complex-structured periodic media* (Springer, 1992).
- [110] P. YEH AND C. GU, *Optics of liquid crystal displays* (John Wiley & Sons, 2010), Vol. 67, Chap. 7, pp. 461–484.
- [111] T. SCHARF, *Polarized light in liquid crystals and polymers* (John Wiley & Sons, 2007), Chap. 11, pp. 349–391.
- [112] D. W. BERREMAN, “Optics in stratified and anisotropic media: 4×4 -matrix formulation”, *J. Opt. Soc. Am.* **62**, 502 (1972).
- [113] A. GEVORGYAN AND M. HARUTYUNYAN, “Chiral photonic crystals with an anisotropic defect layer”, *Physical Review E* **76**, 031701 (2007).
- [114] D. M. SULLIVAN, *Electromagnetic simulation using the FDTD method* (John Wiley & Sons, 2013).
- [115] I. ABDULHALIM, “Analytic propagation matrix method for linear optics of arbitrary biaxial layered media”, *Journal of Optics A: Pure and Applied Optics* **1**, 646 (1999).
- [116] D. HAKOBYAN AND E. BRASSELET, “Optical torque reversal and spin-orbit rotational Doppler shift experiments”, *Optics express* **23**, 31230 (2015).
- [117] K. Y. BLIOKH, Y. GORODETSKI, V. KLEINER, AND E. HASMAN, “Coriolis effect in optics: unified geometric phase and spin-Hall effect”, *Physical Review Letters* **101**, 030404 (2008).
- [118] L. MARRUCCI, C. MANZO, AND D. PAPARO, “Optical spin-to-orbital angular momentum conversion in inhomogeneous anisotropic media”, *Physical Review Letters* **96**, 163905 (2006).
- [119] X. WEI, H. SHI, X. DONG, Y. LU, AND C. DU, “A high refractive index metamaterial at visible frequencies formed by stacked cut-wire plasmonic structures”, *Applied Physics Letters* **97**, 011904 (2010).
- [120] J.-T. SHEN, P. B. CATRYSSSE, AND S. FAN, “Mechanism for designing metallic metamaterials with a high index of refraction”, *Physical Review Letters* **94**, 197401 (2005).

- [121] M. CHOI *et al.*, “A terahertz metamaterial with unnaturally high refractive index”, *Nature* **470**, 369 (2011).
- [122] D. MCGLOIN AND K. DHOLAKIA, “Bessel beams: diffraction in a new light”, *Contemporary Physics* **46**, 15 (2005).
- [123] A. GEVORGYAN AND M. RAFAYELYAN, “Optics of anisotropic metamaterial based structurally chiral photonic crystals”, *Journal of Optics* **15**, 125103 (2013).
- [124] J. KIM, Y. LI, M. N. MISKIEWICZ, C. OH, M. W. KUDENOV, AND M. J. ESCUTI, “Fabrication of ideal geometric-phase holograms with arbitrary wavefronts”, *Optica* **2**, 958 (2015).
- [125] W. JI *et al.*, “Meta-q-plate for complex beam shaping”, *Scientific reports* **6**, (2016).
- [126] M. RAFAYELYAN, G. TKACHENKO, AND E. BRASSELET, “Reflective spin-orbit geometric phase from chiral anisotropic optical media”, *Physical Review Letters* **116**, 253902 (2016).
- [127] G. TKACHENKO, M. RAFAYELYAN, AND E. BRASSELET, “Spin-orbit optomechanics of optically levitated chiral Bragg microspheres”, *Physical Review A* **95**, 053839 (2017).
- [128] D. J. BROER, G. N. MOL, J. A. VAN HAAREN, AND J. LUB, “Photo-Induced Diffusion in Polymerizing Chiral-Nematic Media”, *Advanced Materials* **11**, 573 (1999).
- [129] J.-Y. CHEN AND L.-W. CHEN, “Photonic defect modes of cholesteric liquid crystal with spatially varying pitch”, *Physica B: Condensed Matter* **357**, 282 (2005).
- [130] D. SEDRAKIAN, A. GEVORGYAN, A. Z. KHACHATRIAN, AND V. BADALIAN, “Photonic band gap in 1D Photonic crystals with gradient profile of pitch and amplitude of modulation”, *Optics communications* **271**, 451 (2007).
- [131] R. BALAMURUGAN AND J.-H. LIU, “A review of the fabrication of photonic band gap materials based on cholesteric liquid crystals”, *Reactive and Functional Polymers* **105**, 9 (2016).
- [132] M. MITOV, A. BOUDET, AND P. SOPÉNA, “From selective to wide-band light reflection: a simple thermal diffusion in a glassy cholesteric liquid crystal”, *The European Physical Journal B-Condensed Matter and Complex Systems* **8**, 327 (1999).

-
- [133] Q. HONG, T. X. WU, AND S.-T. WU, “Optical wave propagation in a cholesteric liquid crystal using the finite element method”, *Liquid crystals* **30**, 367 (2003).
- [134] A. GEVORGYAN, K. PAPOYAN, AND O. PIKICHYAN, “Reflection and transmission of light by cholesteric liquid crystal-glass-cholesteric liquid crystal and cholesteric liquid crystal (1)-cholesteric crystal (2) systems”, *Optics and Spectroscopy* **88**, 586 (2000).
- [135] S. ERTEN, S. E. SWIONTEK, C. M. GRAHAM, AND A. LAKHTAKIA, “Experimental investigation of circular Bragg phenomenon exhibited by a mirror-backed chiral sculptured thin film”, *Journal of Nanophotonics* **9**, 090599 (2015).
- [136] T. BRIXNER AND G. GERBER, “Femtosecond polarization pulse shaping”, *Optics letters* **26**, 557 (2001).
- [137] A. M. WEINER, “Femtosecond pulse shaping using spatial light modulators”, *Review of scientific instruments* **71**, 1929 (2000).
- [138] L. YAN, A. E. WILLNER, X. WU, A. YI, A. BOGONI, Z.-Y. CHEN, AND H.-Y. JIANG, “All-optical signal processing for ultrahigh speed optical systems and networks”, *Journal of Lightwave Technology* **30**, 3760 (2012).
- [139] K. IGARASHI AND K. KIKUCHI, “Optical signal processing by phase modulation and subsequent spectral filtering aiming at applications to ultrafast optical communication systems”, *IEEE journal of selected topics in quantum electronics* **14**, 551 (2008).
- [140] M. M. WEFERS AND K. A. NELSON, “Generation of high-fidelity programmable ultrafast optical waveforms”, *Optics letters* **20**, 1047 (1995).
- [141] K. DHOLAKIA AND T. ČIŽMÁR, “Shaping the future of manipulation”, *Nature Photonics* **5**, 335 (2011).
- [142] G. TKACHENKO AND E. BRASSELET, “Helicity-dependent three-dimensional optical trapping of chiral microparticles”, *Nature communications* **5**, (2014).
- [143] D. HAKOBYAN AND E. BRASSELET, “Left-handed optical radiation torque”, *Nature Photonics* **8**, 610 (2014).
- [144] J. M. CANNATA, T. A. RITTER, W.-H. CHEN, R. H. SILVERMAN, AND K. K. SHUNG, “Design of efficient, broadband single-element (20-80 MHz) ultrasonic transducers for medical imaging applications”, *IEEE transactions on ultrasonics, ferroelectrics, and frequency control* **50**, 1548 (2003).

- [145] K. K. SHUNG, J. CANNATA, AND Q. ZHOU, “Piezoelectric materials for high frequency medical imaging applications: A review”, *Journal of Electroceramics* **19**, 141 (2007).
- [146] K. J. MITCHELL, S. TURTAEV, M. J. PADGETT, T. ČIŽMÁR, AND D. B. PHILLIPS, “High-speed spatial control of the intensity, phase and polarisation of vector beams using a digital micro-mirror device”, *Optics Express* **24**, 29269 (2016).
- [147] S. A. GOORDEN, J. BERTOLOTTI, AND A. P. MOSK, “Superpixel-based spatial amplitude and phase modulation using a digital micromirror device”, *Optics express* **22**, 17999 (2014).
- [148] M. MIRHOSSEINI, O. S. MAGANA-LOAIZA, C. CHEN, B. RODENBURG, M. MALIK, AND R. W. BOYD, “Rapid generation of light beams carrying orbital angular momentum”, *Optics express* **21**, 30196 (2013).
- [149] C. MAURER, A. JESACHER, S. FÜRHAPTER, S. BERNET, AND M. RITSCH-MARTE, “Tailoring of arbitrary optical vector beams”, *New Journal of Physics* **9**, 78 (2007).
- [150] I. KAMINOW AND E. TURNER, “Electrooptic light modulators”, *Applied optics* **5**, 1612 (1966).
- [151] E. L. WOOTEN *et al.*, “A review of lithium niobate modulators for fiber-optic communications systems”, *IEEE Journal of selected topics in Quantum Electronics* **6**, 69 (2000).
- [152] C. HAFFNER *et al.*, “All-plasmonic Mach–Zehnder modulator enabling optical high-speed communication at the microscale”, *Nature Photonics* **9**, 525 (2015).
- [153] M. RAFAYELYAN AND E. BRASSELET, “Laguerre–Gaussian modal q-plates”, *Optics Letters* **42**, 1966 (2017).
- [154] M. RAFAYELYAN, T. GERTUS, AND E. BRASSELET, “Laguerre-Gaussian quasi-modal q-plates from nanostructured glasses”, *Applied physics letters* submitted (2017).
- [155] M. RAFAYELYAN AND E. BRASSELET, “Bragg-Berry mirrors: reflective broadband q-plates”, *Optics Letters* **41**, 3972 (2016).
- [156] G. MILIONE, H. SZTUL, D. NOLAN, AND R. ALFANO, “Higher-order Poincaré sphere, Stokes parameters, and the angular momentum of light”, *Physical Review Letters* **107**, 053601 (2011).

- [157] X. YI, Y. LIU, X. LING, X. ZHOU, Y. KE, H. LUO, S. WEN, AND D. FAN, “Hybrid-order Poincaré sphere”, *Physical Review A* **91**, 023801 (2015).